Hochschule für Angewandte Wissenschaften Hamburg
Hamburg University of Applied Sciences

Masterthesis

Filip Kovacevic

Machine Learning with Vibrational Measurement Data of Wind Turbine Environments

Fakultät Technik und Informatik
Department Maschinenbau und Produktion

Faculty of Engineering and Computer Science
Department of Mechanical Engineering and Production Management

Filip Kovacevic

Machine Learning with Vibrational Measurement Data of Wind Turbine Environments

Masterarbeit eingereicht im Rahmen der Masterprüfung

im Studiengang Nachhaltige Energiesysteme im Maschinenbau
am Department Maschinenbau und Produktion
der Fakultät Technik und Informatik
der Hochschule für Angewandte Wissenschaften Hamburg

in Zusammenarbeit mit:
Fraunhofer IWES, Large Bearing Lab
Am Schleusengraben 22
21029 Hamburg

Erstprüfer:	Prof. Peter Dalhoff
Zweitprüfer/ Betreuer:	Dr. Ing. Matthias Stammler

Zusammenfassung

Name des Studierenden

Filip Kovacevic

Thema der Masterthesis

Maschinelles Lernen auf Basis von Vibrationsdaten im Umfeld einer Wind Turbine

Stichworte

Maschinelles Lernen, Windkraftanlagen, Schwingungsmessungen, IEPE-Sensor, svd-Algorithmus

Kurzzusammenfassung

Windenergieanlagen unterliegen verschiedenen Vibrationseinflüssen, die durch schwach gedämpfte Strukturen übertragen werden. Das Ziel ist es, die Vibrationscharakteristik eines Blattlagerschadens in einer Umgebung, ähnlich einer Windenergieanlage, zu isolieren. Hierfür wird ein Prüfstand mit Sensoren bestückt, um anhand eines generierten Testprofiles ein realitätsnahes Testumfeld zu erzeugen. Die generierten Vibrationsdaten werden schließlich von klassischen Ansätzen der Wälzlagerschadensanalyse und eines Separationsalgorithmus beurteilt.

Name of Student

Filip Kovacevic

Title of the paper

Machine Learning with Vibrational Measurement Data of Wind Turbine Environments

Keywords

machine learning, wind turbines, vibrational measurements, IEPE sensor, svd algorithm

Abstract

Wind turbines are subject to various vibrations transmitted through weakly damped structures. The aim is to isolate the vibration characteristics of a blade bearing damage in an environment similar to a wind turbine. For this purpose, a test rig is equipped with sensors to generate a realistic test environment based on a generated test profile. The generated vibration data are finally evaluated by classical approaches of rolling bearing damage analysis and a separation algorithm.

Abstract

Wind turbines are the largest rotating aerodynamic machines humankind has ever built. Due to the need of cost reduction, these machines grow in the matter of performance and thereby in size, which leads to large rotor diameters of currently up to 230 meters and a strong increase in structural load. The lightweight structures of a wind turbine have naturally low damping properties and are subject to external aerodynamic turbulences, as well as a high quantity of internal vibrational sources such as gearboxes and electrical generators. Vibrational measurements are state of the art in failure detection of rotating bearings. They are commonly used in drive trains of wind turbines. As the gearbox has several stages with defined ratios the over rolling frequencies of the bearings are well known, and the signal output of vibration sensors is usually checked for energy levels at these frequencies. Detecting wear marks in an oscillating pitch bearing does highly differ from these traditional approaches. At first, there is a need to get as close as possible to the damaged contact surface, due to the assumed low energy content of the low over rolling impulses on blade bearing failure marks. But even closely placed sensors will always record a mix of vibrational signals, emitted, and transmitted by various sources inside and outside of the turbine such as gearbox noise or aerodynamical whirls along the blade surface. The main objective of this thesis is the examination of the possibility to split these mixed vibrational signals, by distinguishing noise and damage-related contact vibrations via a machine learning processing algorithm and validate the results through findings of a traditional bearing envelope analysis (BEA). The cocktail party effect offers an approach on base of a single value decomposition algorithm (SVD). Therefore, a suitable test environment is built up which modifies the existing test rig environment on the large bearing lab's bearing endurance and acceptance test rig (BEAT0.1). The capability to produce wear marks through a predeveloped test program is given and used to develop test programs and proof the functional abilities of the approach in relation to real turbine behavior. By over rolling of these wear marks vibrational profiles via high and low-frequency accelerometers are recorded and interpreted. The final subsections of this thesis will discuss the results of split noise signals off the SVD algorithm and improved ways of CM based damage procedure for large pitch bearing test rigs and wind turbines as well as a recommendation of a inherit test program.

Acknowledgement

I would like to take this opportunity to thank my colleagues at Fraunhofer IWES for their shared knowledge and support on various projects at the large-scale storage laboratory in Hamburg. In particular, I would like to thank my supervisor, Dr. Matthias Stammler, who gave me the opportunity to work for almost five years on one of the most exciting topics of our time for a sustainable future, wind energy. He is an outstanding researcher and has supported me developing my conceptual thinking. I would also like to thank Professor Peter Dalhoff, who always served my interest in wind turbines with his great expertise. During this socially and familial turbulent and challenging times along with my masters studies, I was also able to enjoy the full support of my partner Helena, for which I am very grateful.

Table of Contents

I. Symbols and Formula

Nm	Newton meter
$MxyB$	Combined Blade Root Momentum
$x/2b$	Contact Ellipse and Overrolling Ratio
GPa	Gigapascal
w	Deformation of Material
B	Bulk Modulus
ρ	Density
v	Contraction
c_l	Longitudinal Wave Speed
c_s	Shear Wave Speed
E	Young’s Modulus
G	Shear Modulus
Hz	Frequency in Hertz
$h(t)$	Unit Pulse Function
f_t	Carrier Frequency
f_M	Modulation Frequency
$\propto_c$	Bearing Contact Angle
D_{Outer}	Bearing Outer Diameter
D_{Inner}	Bearing Inner Diameter
D_{Pitch}	Bearing Contact Diameter
V_i	Inner Ring Contact Speed
V_{rb}	Rolling Body Circumference Speed
D	Rolling Body Diameter
$\dot{\rho}$	Rotational Speed
f_I	Ball Pass Frequency of Inner Ring Defect
f_O	Ball Pass Frequency of Outer Ring Defect
f_R	Ball Pass Frequency of Roller Defect
f_D	Low Speed Drive Shaft Frequency
R_{xy}	Cross Correlation Process
J	Number of Sound Sources
I	Number of Sensors
$S_{(\omega,t)}$	Short Time Fourier Transformation

II. Abbreviations

CMS:	Condition Monitoring System
BEA:	Bearing Envelope Analysis
LBL:	Large Bearing Lab
OEM:	Original Equipment Manufacturer
HAWT:	Horizontal Axis Wind Turbine
SCADA:	Supervisory Control and Data Acquisition
CPC:	Collective Pitch Control
IPC:	Individual Pitch Control
LIDAR:	Light Detecting and Ranging
RCF:	Rolling Contact Fatigue
WT:	Wind Turbine
FD:	Frequency Domain
TD:	Time Domain
HS:	High Speed
LS:	Low Speed
OPEX:	Operational Expenses
LCC:	Levelized Cyclic Costs
BEAT:	Bearing Acceptance and Endurance Test Rig
LAS:	Load Application System
DUT:	Device Under Test
FTE:	Force Transmitting Element
HPU:	Hydraulic Pressure Unit
AI:	Artificial Intelligence
BSS:	Blind Source Separation
SVD:	Singular Value Decomposition
FFT:	Fast Fourier Transformation
STFT:	Short Time Fourier Transformation
IEPE:	Integrated Electronics Piezo Electric
SHM:	Structural Health Monitoring
CSV:	Comma Separated Value
BPFI:	Ball Pass Frequency of Inner Ring
BPFO:	Ball Pass Frequency of Outer Ring

III. Table of Figures

IV. List of Tables

1 Introduction

Over the last year, 93 Gigawatts of wind power capacity were installed globally, thereby following the groundbreaking growth of 2020 with an increase of 14.2% in 2021 [1]. These years mark the highest rate of annual installed capacity ever since and consequently follow a trend that led to a total installed capacity of 837 GW, avoiding 1.2 billion tons of CO_2 [1]. Recent natural catastrophic events such as severe draughts e.g., in Madagascar, central Africa and simultaneous floodings in West Germany, nowadays occur 400% more often than in 1970, show the upmost importance of Co_2 reduction to limit the global warming to a maximum of 1,5 °C [2] . Meeting this temperature limitation requires the wind energy capacity to quadruple [1]. Growing on capacity demands suitable high wind areas, leading to a further distribution of wind energy into remote areas such as far away forests in e.g., Scandinavia and offshore locations [1]. Turbine design reaches enormous rotor dimensions while turbine producers aim to reduce material input for structural components, followed by the effect of highly loaded, lightweight structures with naturally low damping properties [3]. Meanwhile pricing pressure plays a significant role for turbine manufacturers, such as the maintenance sector. Reducing offshore turbine downtime, like critical component failure such as main bearing or gearbox failure, is one of the main objectives of traditional predictive maintenance and owed to high efforts and costs in offshore related component exchange. Focusing on real time condition monitoring (CM) enables a trend based, quick response and long term ahead planning of maintenance activity, which becomes crucial due to high prices for offshore installation equipment and downtime compensation payments [4]. Currently, condition monitoring solutions are widely used for drivetrain and structural components of wind turbines (WT). These systems consist of vibrational sensors and strain gauges, which store low-frequency load data in on-site data loggers. Data trending is then frequently performed to estimate the damage process in bearings or define the fatigue-related structural integrity of tower structures. As this procedure is derived from standards for industrial production such as ISO 7919-3 AMD 1, the focus is on frequency analysis and energy level quantification to match the measurement results to the real state of component damage. Detecting wear marks on oscillating pitch bearings does highly differ from these traditional approaches. Due to the assumed low energy content of the low over rolling impulses on blade bearing failure marks, the sensor should be placed as close as possible to the source of damage related (contact) vibrations and meet the highest sensitivity needs. But even closely placed sensors always record a mix of vibrational signals, emitted, and transmitted by various parts and structures inside and outside of the turbine such as gearbox noise or aerodynamical whirls along the blade surface. Difficulties are expected while defining a sensor type that provides a promising frequency range with high sensitivity whilst not being over excited or saturated by noise of peripheric components. To advance the development of damage analysis of pitch bearings, incorporating state-of-the-art data clustering and AI algorithms while considering traditional CM approaches is essential. In Chapter 2, state-of-the-art measurement methods of gearboxes, such as classical condition monitoring systems (CMS) and bearing envelope analysis (BEA) for low energy density impulses, as well as basic physical knowledge of physical processes, such as sound propagation in solid bodies related to these methods, will be compiled [5] [6]. Since pitch bearings face individual pitch control demands while increasing in load due to larger blades and increased rotor torque requirements, Chapter 2 also covers a general explanation of pitch patterns under high contact loads, resulting in false brinelling wear marks. These marks, when subsequently over-rolled, create solid-born sound and are assumed to lead to further bearing damage modes [5]. Chapter 3 focuses on reproducing these wear patterns in a defined structural environment by comparing test rig options and capabilities at Fraunhofer IWES's large bearing lab (LBL), while Chapter 6 6 details the creation of a reproducible test process. To study the vibrational signals, Chapter 5 requires a high-sensitivity sensor setup, which calls for extensive investigation in terms of sensor availability, application possibilities, sensitivity, and data storage. After solving these first issues a machine learning data analysis is selected for a suitable separation algorithm to clarify the measured vibration from surrounding noise sources in Chapter 4, followed by the last Chapter 8 and 9 with a critical discussion of the results and an outlook for a recommendation of a appropriated process for large test rigs and wind turbines.

2 State of the Art

2.1 Wind Turbine History

It has been more than 3700 years since humankind started to use the movement of light air molecules as a technical advantage by blocking up their flow direction to create a torque moment by simple reed mats. Whole empires relied on this cheap and unlimited energy for millennia to grind their agricultural products or drive the Archimedean screw to pump water into their viaduct systems or out of swamps. These rather simple machines used the phenomenon of the displacement principle, which results in a very low coefficient of power. Since horizontal windmills established and finally improved in the means of a lift driven rotor in the early 20th century, while power consumption of wester society rose astronomically, the electrical power production through wind energy came close to an industrially functional application. As many times in human history, war, and the affinity to burn fossil ancient creatures and their byproducts, dominated common sense and led to a strong development reduction of industrial scale wind energy machinery. Finally, the first politically motivated shortage of middle east oil supplies kick started the motivation to harness free kinematic energy of the wind molecules in the 1970's. As history of human irrationality repeats constantly, nuclear power has cut numerous wind energy approaches in central Europe and the United States as an expected "clean" energy alternative. In 1986 a horrible combination of malfunctioning man and machinery, which hardly need a further naming, led to vast contaminations and the cruel death of up to 4000 humans, by following radiation related disease [7]. In the early nineties of the 20th century, a slow improvement of the lift based horizontal axis wind turbine continued and made the development of Multi Megawatt turbines possible, which will be scoped by this thesis. Since then, political regulations first pushed the wind industry sector by subsidies, making innovative development and a lively but inefficient market possible. Then pushing down the payout to drive competition up, which led to a sorted-out wind industry with only few, big original equipment manufacturers (OEM) in recent years. Meeting the trend of offshore development measures makes turbines grow in power output, and due to Froude-Ranking, proportional to its rotor surface [3]. The Square Cube Law still heats up WT designer's minds in technical discussions about the possible limits in material optimization for blade length and tower height but leaves no doubt about the continuing OEM battle in higher electrical output values of ever new appearing turbine models with an increase of dynamic loads due to their dimensions [8]. The following subsections 2.1.1 & 2.2 will intersect the most relevant turbine design principles for this thesis and their specific properties and difficulties, related to these.

2.1.1 Design Principles

Figure 1 shows a three bladed up-wind turbine. WT are yet the largest rotating machines humankind has ever built. Within a 20-year design lifetime, some of these turbines expect more than a billion load cycles [9]. By mid-2022 the largest fully commissioned prototype reaches out with 220 meters of rotor diameter and can boost its power production up to 13 Megawatts. This is enough to supply 16,000 households at rated wind speed [10]. As mentioned earlier, the horizontal axis wind turbine (HAWT) as shown in Figure 1 has taken the sacrosanct lead in installed capacity in a global scale. To name one advantage, the possibility to align the horizontal axis of the rotor with the wind fields flow direction via azimuth drive should be mentioned. In contrary to down wind turbine models of the early 1990's, this up wind design reduces aerodynamic tower induced turbulences, with thereout periodic load control that enables light weight structures as shown in Figure 1.

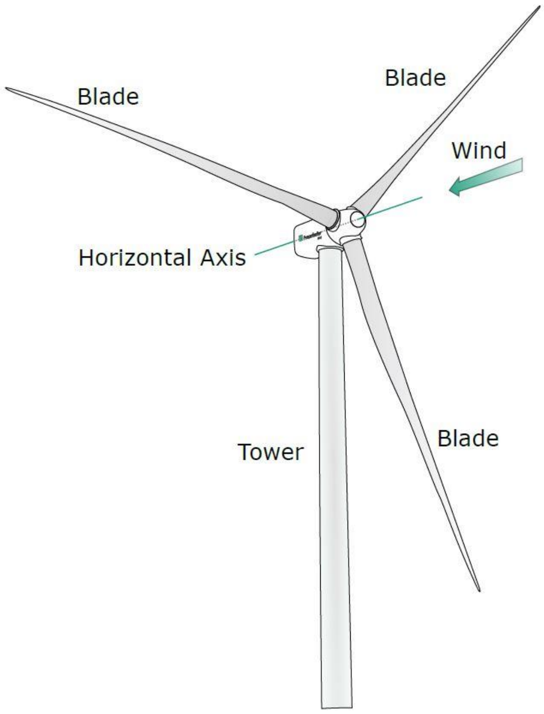

Figure 1: Schematic structure of *Fraunhofer's Adwen AD8* turbine [11]

2.2 Components and Sources of Vibrations

As before mentioned, horizontal axis wind turbine designs are state of the art, as aerodynamic load distributions of vertical axis turbines are barely predictable and subject to highly fluctuating and turbulence demanded loading, which in the past, led to severe component damage and falling blades in 2020 [12]. But aerodynamic turbulences are also a considerable difficulty on horizontal axis turbines, challenging the blade and blade joint component with high frequency stochastic vibrations. Considering the wind turbine as a multi component system with stiff couplings (bolted flange connections) between the main components, this property validates the assumption of a vibration transducing system. To keep things simpler, the turbine is divided into two main assemblies, or main systems. For this thesis only vibration emitting or transmitting components are focused and named in the following. These main systems consist of the machine housing, which inhabits amongst others, the drivetrain (gearbox, main bearing, and generator) as well as the yaw drives. Second, the rotor with a hub, a pitch system (pitch bearings and drives) and rotor blades [13].

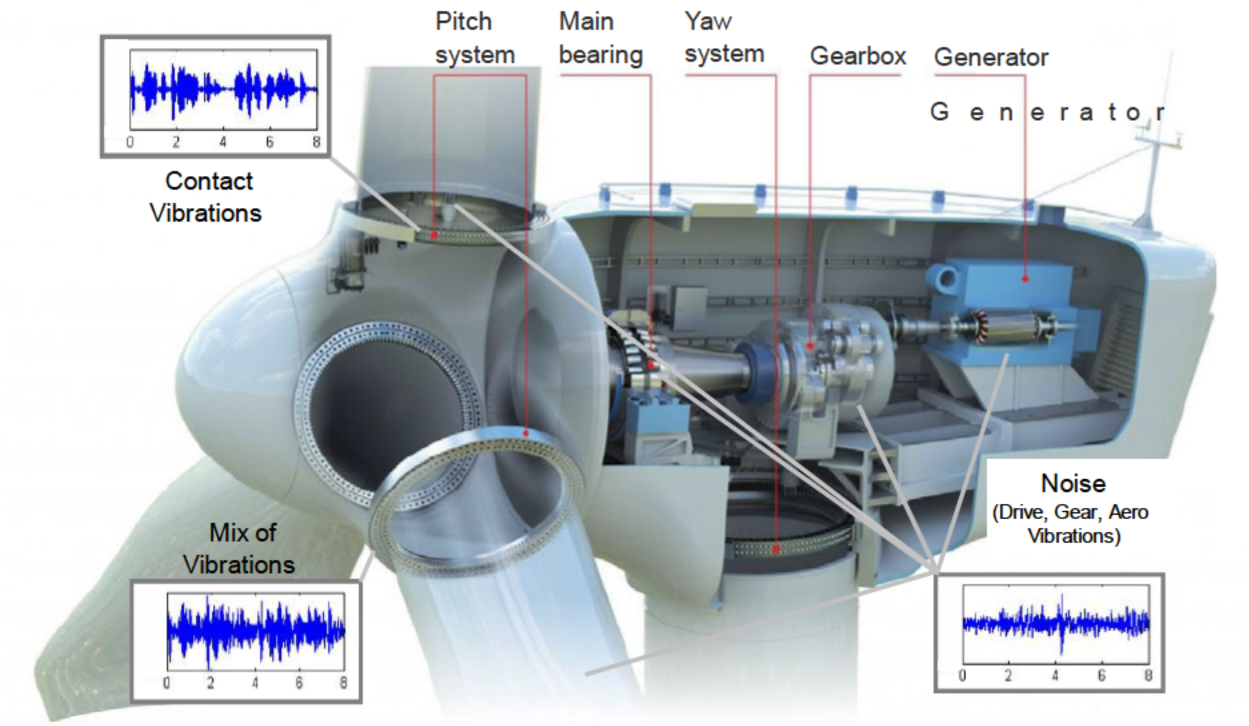

Figure 2: Wind turbine gear type with pitch control [14]

Figure 2 shows a turbine system of a non- direct drive turbine which has a gearbox reduction. This turbine type is the example turbine type for this thesis. The shown vibration signal plots show the schematic problem of this thesis, which is the differentiation of noise signals from a mix of surrounding machine environment and pitch bearing related damage induced vibrations (contact vibrations).

2.2.1 Pitch Control

Considering the enormous growth in blade length over the past decades and the thereby related squared increase of the power output, the need for a suitable power limiter and braking system gets crucial [15]. Early Danish models of the 1980's use the aerodynamic phenomenon of stall and huge dynamically controlled disc brakes to limit their power output. These turbines have fixed blades that start to stall as soon the wind speed exceeds the nominal designed operational wind speed. The rotor blades are bolted directly to the hub, while exceedingly inducing vibrations into the turbine. These vibrations led to high fatigue loads and demanded a proportionally big amount of material to support the entire structure. Modern light weight wind turbines use a so called "pitch" to regulate the flow into the blade and thereby related torque of the rotor- and generator shaft. When turning the blade to the production pitch position ($\alpha = 0°$ in Figure 3 & Figure 4), the turbine gains tip speed, proportional to the flow direction along the Vw direction in Figure 3.

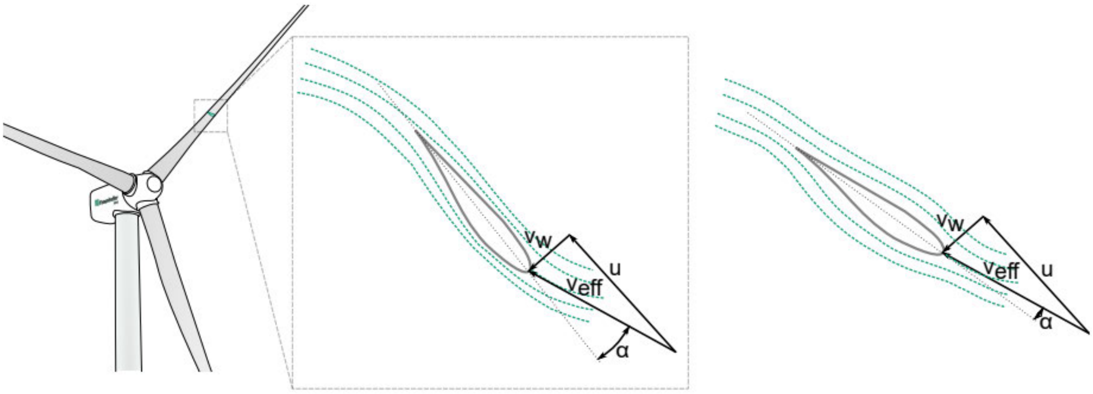

Figure 3: Foil profile adjustment by pitch angle, modified from [11]

When nominal wind speed is reached, a signal is sent to the supervisory control and data acquisition system (SCADA) to start the depowering of the turbine. This happens by turning the rotor blade along the Z- axis of Figure 4, as the rotor induction is increased, and rotational frequency is lowered. If the windspeed at hub height exceeds the design cut- out wind speed limit of turbine, the SCADA system shifts the pitch angle to 90 ° (see Figure 4), which is the position of the aerodynamically defined brake position. These events cause vibrations.

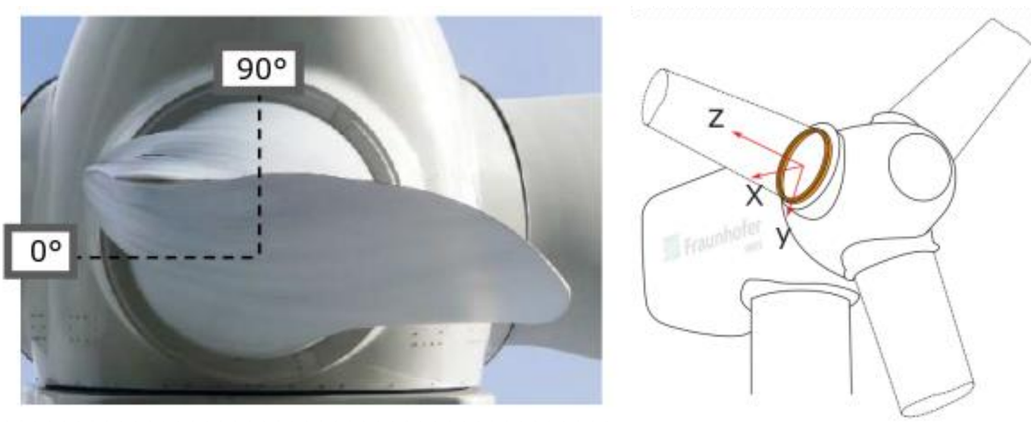

Figure 4: Rotor blade and pitch coordinate system, modified from [11]

Regulating the rotor torque and retarding the turbine in case of emergency is not the only purpose pitch drives are used for. Specially since turbine diameters grew while turbine components got slender, the design of turbine support structures change from differing steel and concrete structures to steel tube and hybrid towers [3]. These towers are benefitting from lower weight and hence are preferred for the growth of turbine height as well but provide a soft base along with the Campbell diagram [3]. The soft design has short comings in terms of lower Eigenfrequencies, which can be imposed by pitch-controlled ride through windspeeds at turbine start up procedure and in nominal production wind range. Last mentioned makes a smart control strategy of the turbine a core capability to prevent high quantities of vibrations and possible component fatigue. To achieve these yet mentioned, more basic tasks, the basic model of a collective pitch control (CPC) system has been developed in the 1980's. In this terminology, collective means turning all blades along their Z- axis (see Figure 4) at the same speed. So, all pitch angles were set the same way. In nominal turbine production ranges, which makes up the major life span of the production time on high wind offshore sites, control strategies come crucial as load management is needed to reduce loads at this operation state with maximum thrust force [3]. But this additional control strategy differs from the beforementioned since wind is not expected as laminar and consistency over the rotor diameters. This is derived from Figure 4, showing a stochastic wind speed distribution up wind to the rotor surface. In a vertical direction wind shear has a dominant influence, which has the effect of lower wind speeds at the lower tip position due to ground related turbulences, with a opposite influence on the same tips upper position.

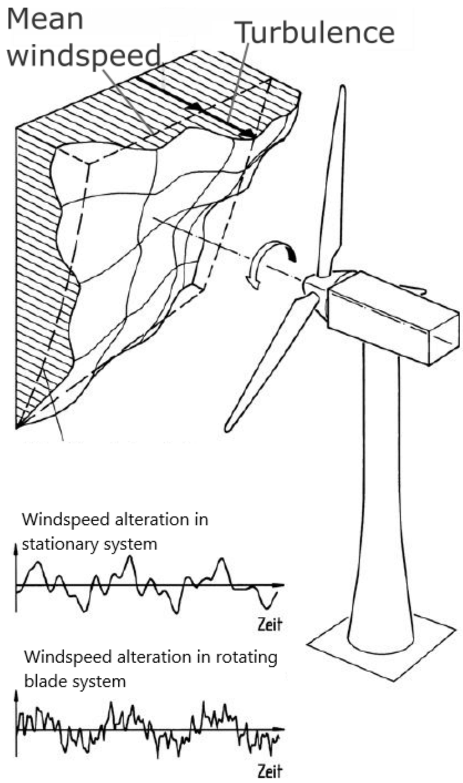

Figure 5: Stochastic wind field distribution, modified from [13]

Due to the large rotor diameter of up to 220 m, this difference is a drastic increase of wind speed and consequently induces higher periodic loads at the blade root and a related nodding momentum (stationary hub moment My). A Geer momentum is also to be considered, as a horizontal distribution in Figure 5 shows a in homogeneous wind field over the horizontal axis. These stochastic influences can be measured by a light detecting and ranging (LIDAR) device measuring the wind field in front of the turbine to predict the upcoming thrust values per rotor blade and following pitch control to increase induction on a particular blade, while reducing the load. Also, the information of wind speeds in advance to the rotor plane can help predict local loads on certain blades and thereby on its blade root momentum (My). A possible purpose for this load state information could be delineated for later thesis related test profile ideas. To be fair, this wind field related pitch control approach is still at a test state by leading OEM's and has yet not fully passed the industrial application threshold [16], [17] .But individual pitch control (IPC) is state of the art since the early years of the second millennia. The IPC is developed for a typical problems of a horizontal wind turbines, so called tower shadow or dam and wind shear over height. This dam effect of a slower air stream in front of the tower reduces a significant and periodical amount of thrust of the rotor blade passing through the downwards pointing blade, aligning with the tower axis while wind shear induces a high bending moment on the upward pointing blade. This leads to severe harmonical excitation of the entire turbine structure, followed by a fatigue load preventing increase of structural component reinforcement, weight and consequently costs. Using IPC, to turn the blade by around 1 - 4° along the Z- axis (value fits below nominal turbine wind speed) of Figure 4 before entering the tower shadow and then oscillating back to 0° after leaving the tower zone, reduces the dynamic load significantly and cuts down the turbine mass and costs. [11]. Combined phenomena's as beforementioned aerodynamic controlled, output power regulation, braking and IPC for load reduction, qualifies the pitch systems to one of the most complex, high loaded and most safety relevant components [3].

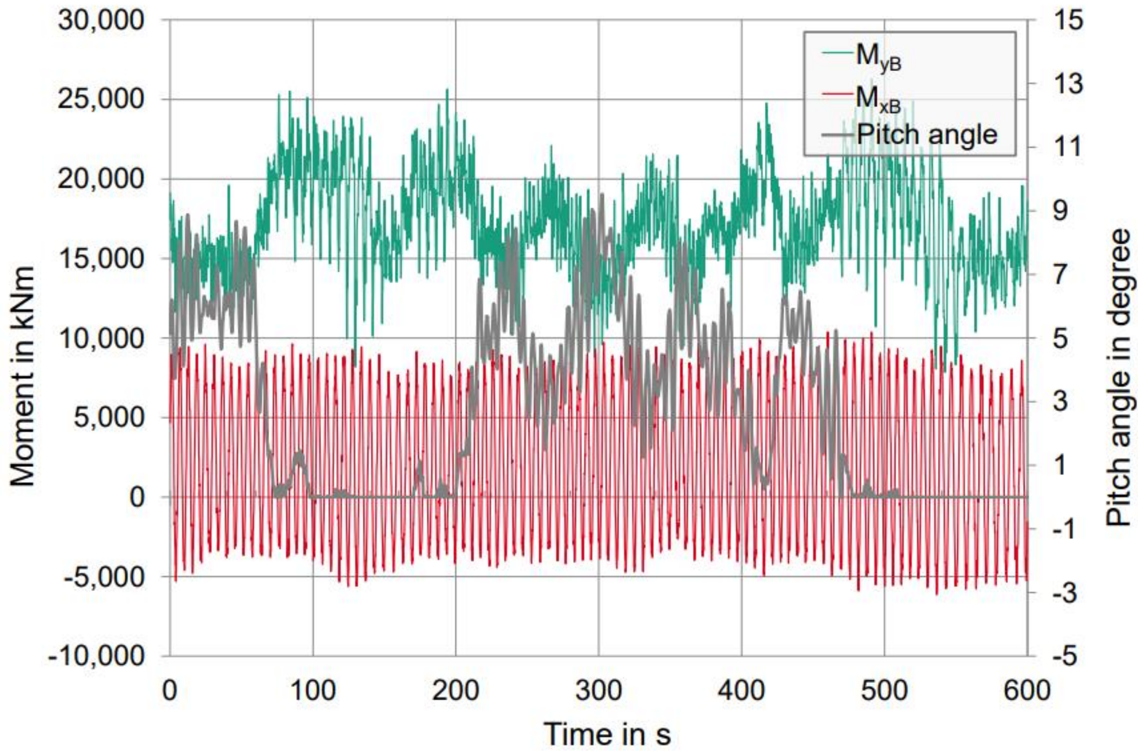

Figure 6: Pitch movement and reaction moment profile [11]

Fluctuating winds, as seen in the lower left corner of Figure 5, lead to constant pitch angle adjustment superimposed by IPC movements, related to load reduction strategies. Figure 6 shows the interaction of an uneven windspeed distribution and periodic tower dam load in the oscillation of the green line. The flap wise bending moment of the blade root M_{YB}. M_{XB} shows the influence of gravity and tumbles around the zero crossing of its own weight related bending moment. These moments build a combined moment due to simple vector addition. The pitch angle, shown as a grey line in Figure 6 and verifies the idea of highest thrust forces, hence highest M_{YB} with a 0° pitch angle below rated wind speed [3]

2.3 Design Principles of Wind Turbine Bearings

As mentioned in the preceding section 2.2, wind turbine components do resist high loads, while light weight designs make of- the-shelf solutions rather impossible to use. Besides the more standardized, continuously rotating bearing systems which are located in the WT gears, drives and main bearing, a second and rather rare category of bearings dominates WT applications. These so-called slewing bearings are used to perform oscillating movements of the yaw- wind direction adjustment, as well as the beforementioned pitch system. Last mentioned bearings are used to resist exceedingly small oscillations, compared to the stochastic movements of the yaw bearing and mainly lacking on sufficient lubrication supply within the rolling bodies contact zone [14]. The following subsections 2.3.1 to 2.3.2 will give a brief overview of the most relevant bearing designs along with their specific capabilities and most relevant operational threads.

2.3.1 Continuously Rotating Bearings in Wind Turbines

When observing a wind turbine, one can determine its continuous rotation in power production mode and even below cut in wind speed while idling with low rotation rates. Having a closer look from cut- in wind speeds to moderate windspeeds of nominal production, it might be possible to define a relation between an increase of rotor frequency with the windspeed. This control strategy is related to gain an optimum of the tip speed ratio. As soon nominal windspeed is reached, the before mentioned pitch system starts to hold the rotor frequency at a constant level. One of the main reasons for a constant rotational frequency of the drive train is, besides the already mentioned load limiting property, an ideal input frequency for the wind turbines generator [3] [13].

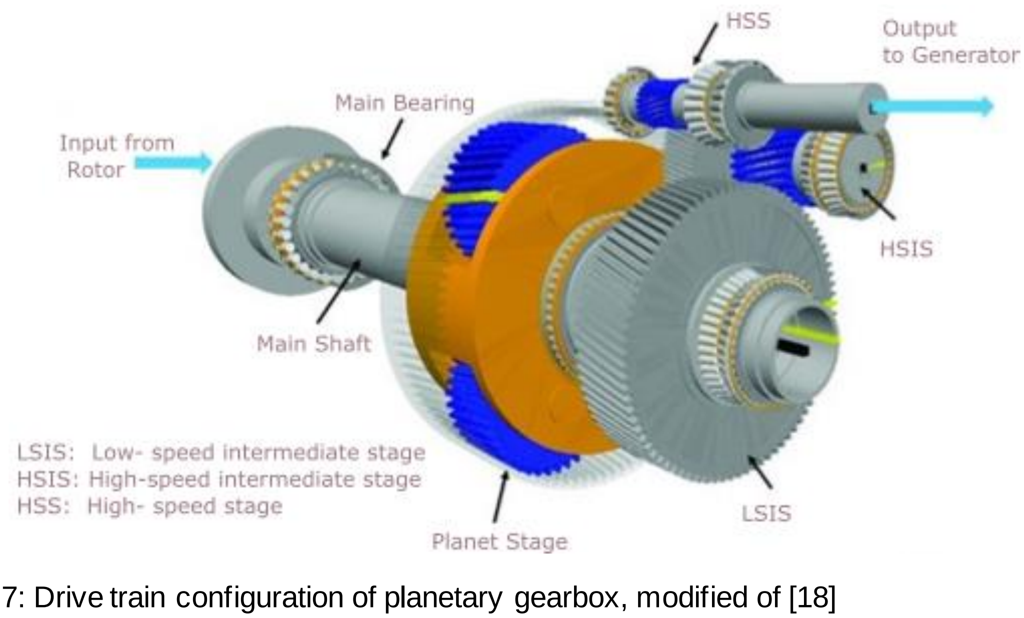

Figure 7: Drive train configuration of planetary gearbox, modified of [18]

To achieve the transmission of rotational energy between the low rotor frequency of around 0.2 Hz and the considerably high output frequency of 50 Hz in most cases a multistage planetary gearbox, as shown in Figure 7, is used. Also, planetary gears are used to transmit the motor torque of a pitch or yaw drive system. Bearings of these components are mostly specified for wind turbine application and sometime be black oxide coated to survive long rolling body slip in the event of turbine or grid fault [18]. Of course, there is a variety of different generator types, and most offshore turbines use permanent magnet synchronous generators without gearing, but still utilizing pitch and yaw drives with planetary stages. Summing up the aforesaid findings from idling to cut out, a wind turbine drive train and pitch-/ yaw drives see a variety of directional and rotational frequencies. As every reduction stage has a specific meshing frequency as well as every bearing type and component specifies a certain over rolling frequency, the bandwidth of possible vibration source is widespread over the later discussed frequency bandwidth. But as long the dimension of each component is known, a designation of each components vibrations is rather possible [5].

2.3.2 Pitch Bearing Designs

, these bearings enable the blades to adjust the loads and the derived power output. They do resist extraordinarily high loading. To give a short impression of the loading by single blade of the most powerful offshore turbines a comparison with the help of a Volkswagen Golf series 6 and its mass of 1297 kg will be performed. At the event of a 50- year wind gust the combined bending moment $M_{xy}B$ of these turbines, as seen as a green line in Figure 6, can reach up to 75.000 kNm peak moment. The comprehensive calculation of a “Golf-Kilometer” bending moment results in six fully equipped Volkswagen Golf, standing on 1000-meter-long lever, connected to the pitch bearing.

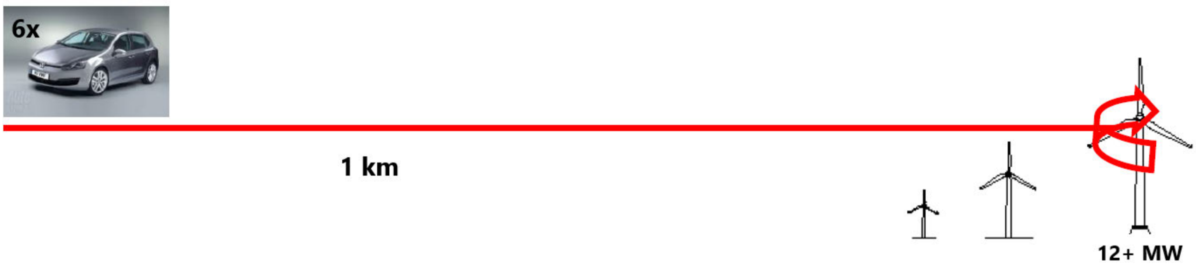

Figure 8: Load comparison, modified of [19]

These massive moments and smaller vectorial loads lead to deformations due to semi stiff ring, hub and blade boundaries and finite stiffness of the hertzian-/ and- or lineal contact zone of roller and raceway [11]. Additional wind speed turbulence and 1 to 3- periodic excitation through gravitational and centripetal forces lead to positive dynamic loading in multiple degrees of freedom [3], [9]. These undesirable load cases are displayed in Figure 9 and helps define the most probable area of damage and thereby scope of later measurement approaches. Figure 10 shows a render of a full-size computer aided design model of such a turbine bearing type with the explanation below.

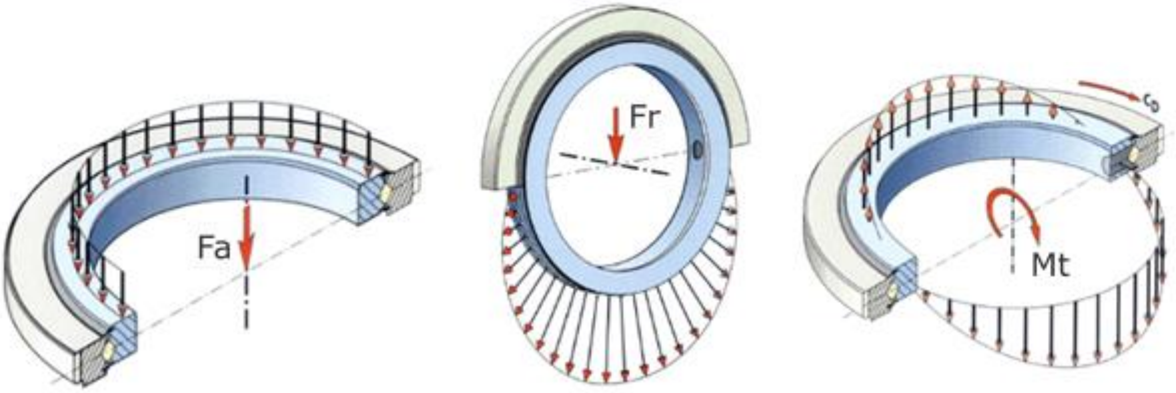

Figure 9: Axial, radial and momentum loading of pitch bearing [20]

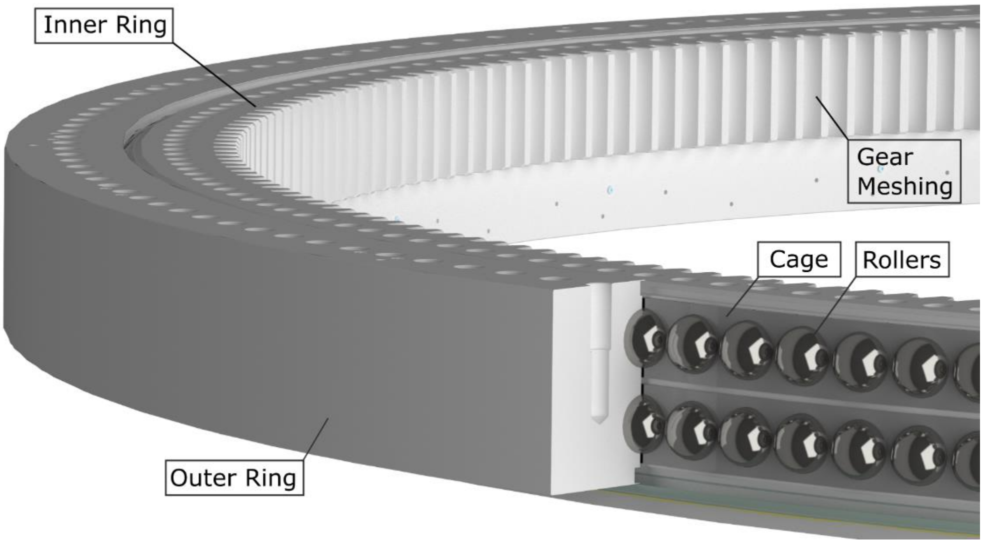

Figure 10: Render of Ø 6-meter four-point contact double row ball bearing [21]

By the knowledge of the author, the main market in 2022 is based on four- point contact bearings, followed by three row- roller bearings and a mixed designed of balls and rollers consecutively displayed from left to right in Figure 11 [11]. Knowing the area of highest loading inside the bearing- / raceway structure could come helpful in terms of vibrational sensor application, hence the load directions in Figure 11 are indicated with orange arrows. Differences appear here in the load direction of the three differing designs. On the very left side, the radial force component is also transduced via the 40°- 45° contact angle of the ball, whilst the others have a separate, pure radial, rolling element. These two are called T- Solid shapes and enter the market slowly since the last years [22].

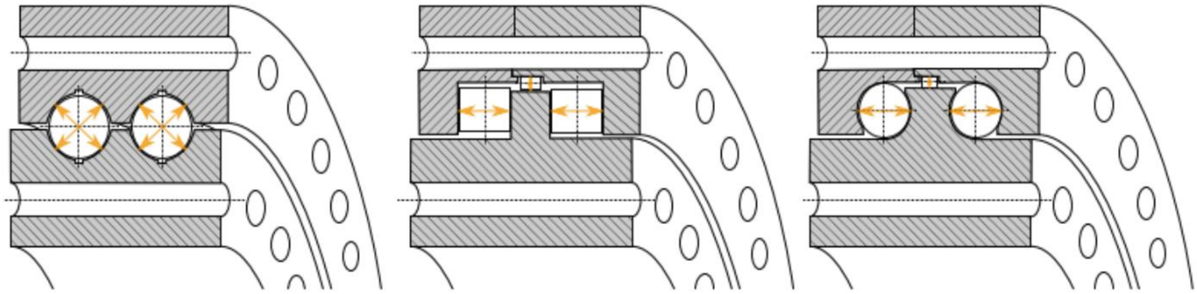

Figure 11: Commercial pitch bearing types [11]

Due to its wide ring deformation abilities and low cost built, the four-point bearings are widely spread and do consequently provide a wide range of fault related knowledge. Their balls are separated by a steel band cage, which induces less friction into the roller section than other bearing type cages as seen in Figure 10. Assembling these bearings, calls for a fill plug to fill up the bearing ball by ball [3]. The arrows of this bearing type show an equivalent radial component of the load direction, leading to higher radial forces transmitted into the bearings outer ring which can result in a tilting deformation of the outer and inner ring. These deformations feasibly conduct to higher load on the raceways edges and will be deeper delineated in section 2.4. On the other hand, pitch bearings with rollers and split ring design allows pre-filling of the rollers into the bearing raceways and does ratify roller pretension via the bolted connection, but suffer under higher costs [23] [22] [24]. As before mentioned, the load distribution and unfavorable movement patterns of the rolling element do strain the bearing components and most probably result in bearing damage modes. These vary from operation and bearing designs and will be the main topic of the next subsection.

2.4 Damage Modes of Wind Turbine Components

As mentioned in section 2.2, pitch bearings suffer highest structural loading and at the same time operating with very small oscillating movements. While Gears are driven with highly fluctuating rotational speeds, but mainly more directional for a longer period. This results in high contact pressure on the meshing contact and slip behavior on the rolling contacts of the inbound bearings. It is understood, then each of these operation conditions can quickly produce a certain amount of contact damage. Figure 12 shows the area of possible damage in a vertically cut pitch bearing sketch which has been created by Dr. Matthias Stammler in his outstanding thesis of [11], pinpointing the most relevant influences on pitch bearing damage in an test lab environment. Each of these numbered Positions indicate the root causes area of several damage modes that might appear due to various reasons. Mostly a mix of these reasons lead to early-stage damage and then accelerates the damage propagation reciprocal [11] [25]. In Table 1 of the next page, wear is a frequently appearing phenomenon, as it appears in all positions of the pitch bearings high loaded areas as a cause of failure.

Table 1: Location and possible damage modes in Figure 12

LOCATION	RACEWAY	RING	CAGE SEALS	BOLTS	GEARS	GREASE
Figure 12 Index	1	2	3	4	5	1 & 5
Damage Modes	Rolling Contact Fatigue / Wear/ Static Overload/ Edge Wear (Truncation)	Core Crushing/ Structural Fatigue/ Corrosion Cracks (Possible Wear Indication)	Wear	Fatigue/ Wear	Contact Fatigue/ Wear	Wear of Thickener Thickener Degradation

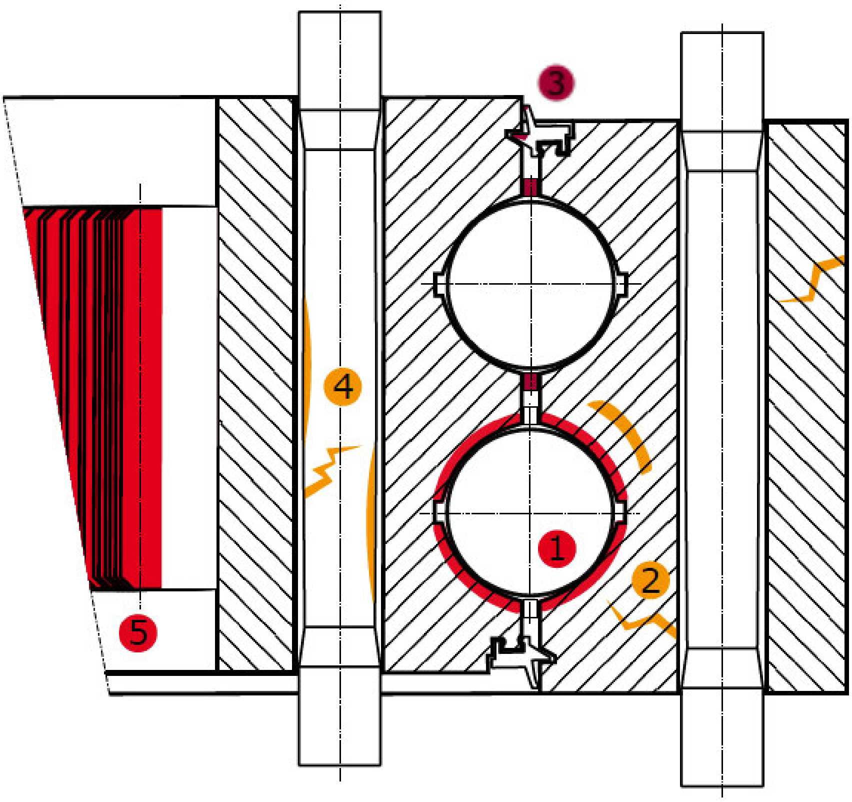

Figure 12: Main damage mode position in blade bearing, modified from [11]

2.4.1 Raceway and Rollers Under the Influence of Wear

The main objective of this thesis is to develop a basic process that one day will help detect early-stage damage of pitch bearings by measured vibrational data on a similar test rig design. In turbine application all kind of component damage has a significant impact due to the vibrational sources which one can be the desired damage type of the pitch bearing for the analysis and the others be noise in the signal that needs to be distinguished and then filtered out. The following subsections will generally deal with the explanation of three relevant damage modes in pitch bearings and give a minor overview of the gear degradation. Distinguishing these three modes has a very practical cause, as the expected vibrational signal, when over rolling these damaged areas in a later state of damage propagation, are differing from one to another. This comes by the position of the damage itself and its geometrical, surface related, properties. Anyhow, the only damage modes that will be taken in practical use for this thesis is wear and ring cracks, but for ones understanding of the real turbine application and the reason for the general scope on wear at the LBL its crucial to explain these root causes in the pitch bearing domain as shown in Figure 12. As mentioned in the earlier section, wear is a prominent root cause for numerous failures on pitch bearing operation. Various research project at the LBL [11] [25] and the IMKT of Leibniz University Hannover [26] aimed on a profound understanding of wear evolution and its influences on other damage modes such as rolling contact fatigue (RCF) and ring cracking. This is so because wear is weakening the surface of a material. It grinds the first layers of material away while enables the eroding influences and thereby increasing the roughness of the contact surfaces. To understand how this exactly happens, one’s imagination may visualize two atomically clean steel cubes. When laying these cubes on each other, with no lubricant between, these cubes will unify withing hours [11]. This happens, in a very similar way, in the contact zones of a roller or gear meshing, as both surfaces do have a very fine machines surface with an optimum of close to zero roughness, as this property reduces harmful friction. Having a constant pitch angle for a longer period like for example e.g., in idling position or constant windspeed production mode without IPC, lubricant gets pressed out of the Hertzian contact zone of the roller/raceway contact and metal contact is given. This contact zone of an angular contact bearing is shown in the following Figure 13.

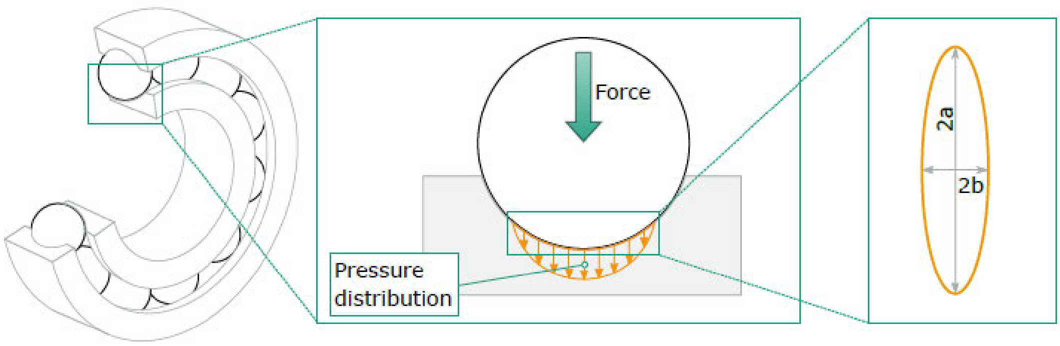

Figure 13: Pressure distribution of hertzian ball contact, modified from [11]

After the first atomic layers unified, movement will rip off fine particles of the raceway or roller surface and form debris. As roller and raceways are designed to withstand heavy loads, their surfaces are hardened. So is the produced debris. When hard particles get compressed between two rigid bodies, an abrasive process effect emerges and produces a wear mark of several micrometers in depth shown in later Figure 16. One parameter that is related to the dimension of wear marks in oscillating bearings needs to be mentioned in this subsection. It draws attention, especially in recent research of the Large Bearing Lab and the IMKT. This is the X/2b ratio which defines the contacted surface of the raceway in correlation of the pitch angle, as well as the contact load represented by the Hertzian contact. See X as the way a roller rolls by a certain pitch angle on a plain when rolled without slip, and 2b as the width of a load related Hertzian contact ellipse of Figure 13. This factor allows to break the limiting boundaries of a particular bearing type by e.g., the load and the roller/ raceway dimensions and makes it possible to compare real size pitch bearings with smaller scaled bearings types like angular contact bearings [11] [27]. Besides the load and the roller travel, the number of overrolling events and the frequency of the repetition has a high influence on the propagation of wear in this area. Of course, there are more influences than pressure and debris particle density involved, such as temperature, solid content and de- bleeding rate of the lubricant, energy density, tribological processes between contact bodies and lubricants and such. But for this thesis a basic overview shall be sufficient. Further information's about these topics were dealt in Dr. Matthias Stammer's and Dr. Fabian Schwack's papers available on the Research Gate website [11], [27]. Following Figure 16 shows a picture of a wear mark on a FAG 7220 angular ball bearing. This bearing type is used in BEAT0 test rigs and allows similar test conditions like four-point contact bearings in WT [11].

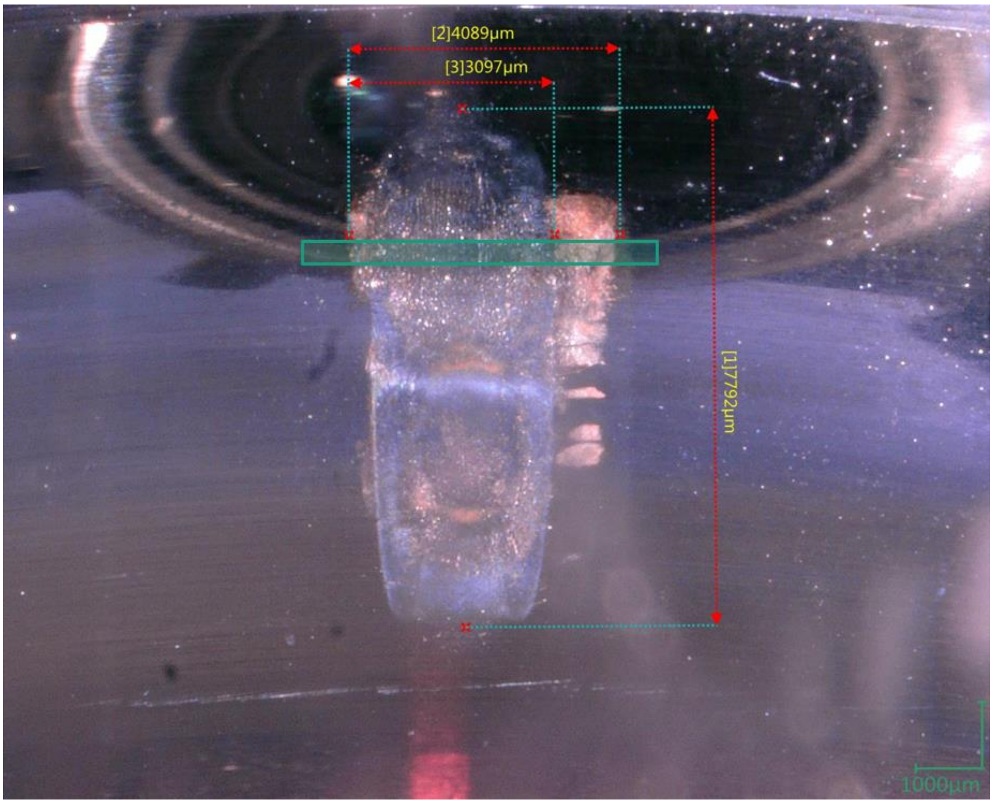

Figure 14: Picture of wear mark dimension and measurement spot, modified from [25]

The green marked area of Figure 14 is the standardized measurement area at the IWES lab and enables the quantification of a wear volume as a description for raceway damage propagation [25].

Figure 15: Zoom on green marked area of Figure 14, modified from [25]

Figure 16 shows a MATLAB surface plot, based on optical microscope measurements performed in the green marked area of Figure 14 and Figure 15, produced within a recent wear propagation related project which is not yet accessible through official papers [25]. Moving along the values of the x- axis of Figure 16, shows a valley formed structure which in fact represents the green area in Figure 14 or zoomed damage area of Figure 15 from left to right. The orange area shows a higher material accumulation and defines the area where fretting corrosion created a debris hump. Green and blue show the area of the damaged surface area, formed like a crater [25]. This is of particular interest for this thesis, as later tests will be performed on a damaged bearings, having an initial damage as shown in Figure 14 and Figure 16 (more information's follow in section 6.1). When over rolling these damage marks with a defined pitch angle or roller speed, the assumption of vibration emission seems plausible.

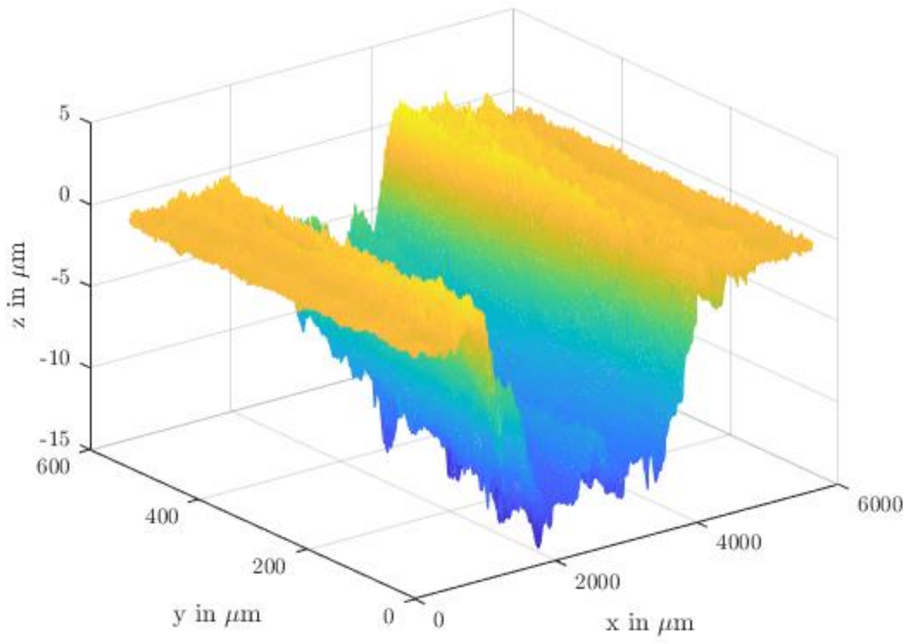

Figure 16: Microscope measurement of defined wear mark area, modified from [25]

2.4.2 Fatigue of Rolling Contacts

Imagining a perfectly lubricated (oil) separated rolling body contact, one's mind would assume an infinite lifetime of this bearing system as, theoretically no thread of debris or such as explained in subsection 2.4.1, occurs. But a real-world production processes are not ideal, and so are not their products. Hence a finite number of impurities in the raceway material emerge and form below surface micro cracks with a high number of load cycles, which in this case is overrolling of a rolling body element [11]. This happens at the area of maximum shear stress below the surface and forms, in initial state, little craters (pitting's). These pitting's grow while over rolled consequently. Due to the higher contact pressure on the edge of the crater, RCF accelerates under following load conditions from this point [11]. Consequently, the raceway gets heavily damaged and loses a big amount of material as displayed in Figure.

Figure 17: RCF on pitch bearing of BEAT6.1 test rig, modified from [25]

Pitting's show a similar structure to wear marks of the previous subsection 2.4.1, as the debris around the crater (orange in Figure 16) also increases the contact pressure locally. So, the idea of a wear induced RCF damage acceleration is likely [28]. The effect of sub surface cracks, provoked by external load, and its acceleration by prior wear damage is still subject to research at the IWES Large Bearing Lab. Having the problem of multiple damage causes and their interaction on pitch bearing surfaces is still not fully understood [28]. Of course, damaged raceway surfaces like the one in Figure 17 will emit massive vibrations into the turbine structure and is mainly detectable by a massive rise of the pitch drive torque momentum [11]. So, considering the RCF damage as a late emerging damage mode while this thesis deals with the initial damage detection, fully developed RCF falls out of scope for the following chapters.

2.4.3 Ring Cracks

Ring cracks can be a product of various causes such as, corrosion, overload, inappropriate interface design or failure in the gear meshing and hardening procedure and thereby most likely of high stress areas. The source of these cracks is subject to a recent research project, connected with ring fatigue, at the LBL [29]. Nevertheless, when cracks emerge with beach marks on the ring elements of a pitch bearing, they weaken its structural strength against ring deformation by reduction of the moment of resistance as the cross section is reduced [30].

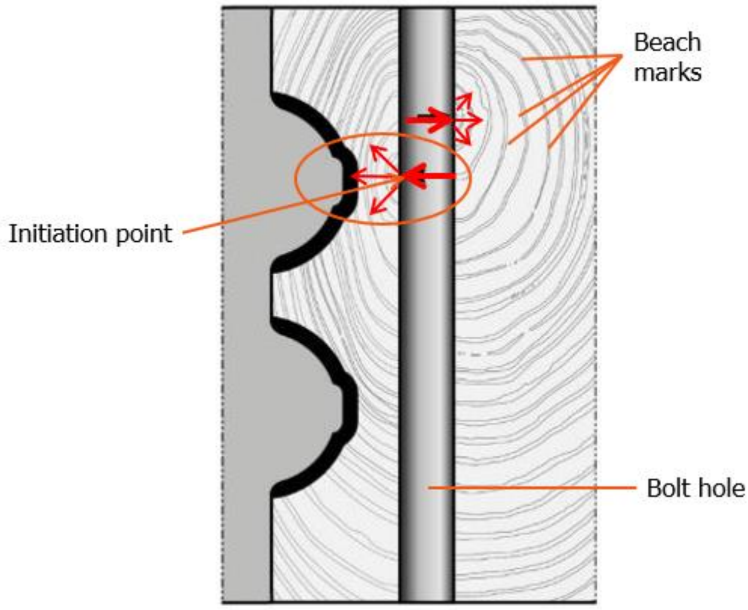

Figure 18: Typical ring crack propagation with beach marks, modified of [30]

As bending moments are the main load case in the pitch bearing system, this weakening is highly problematic as cracks can quickly grow nonlinear and lead to a full split ring. The aftermath of this event can lead to a total loss of structural integrity in the pitch bearing. By widening the raceway diameter tolerance, some bearings lose their rollers, or balls, with the worst consequence of a falling blade and possible further material or personal damage [30]. Considering the scope of this thesis, the detection of such a risky defect would be highly promising in terms of predictive maintenance due to damage related failure effects and costs.

2.5 Machine Dynamic and Structural Acoustic

Machines consist of several components in motion such as rotating shafts, oscillating pistons of hydraulic pumps, etc. while static components may hold them in place or guide a flow of media or force from on source to the desired output structure. Each rotating or oscillating component creates several vibration patterns, with the effect of energy transport through the beforementioned structures in a dedicated waveform. The following Section 2.5.1 will give a brief introduction to the mathematical description of the expected vibration characteristic within bearing test rig components and the practical approaches to handle these environments.

2.5.1 Fundamental Physics for Wave Propagation

Other than waves in water or air, structural waves in isotropic, homogeneous structures such as metals deform in a far more complicated way. This occurs due to their ability to resist shear deformation while fluids cannot. This leads to the fact that compressive and shear waves can co- exist in structures [31]. To simplify this description of the isotropic and homogenous environment, a limitation on structural wave forms is given by longitudinal and transversal wave forms (along and orthogonal to the axis energy propagation).

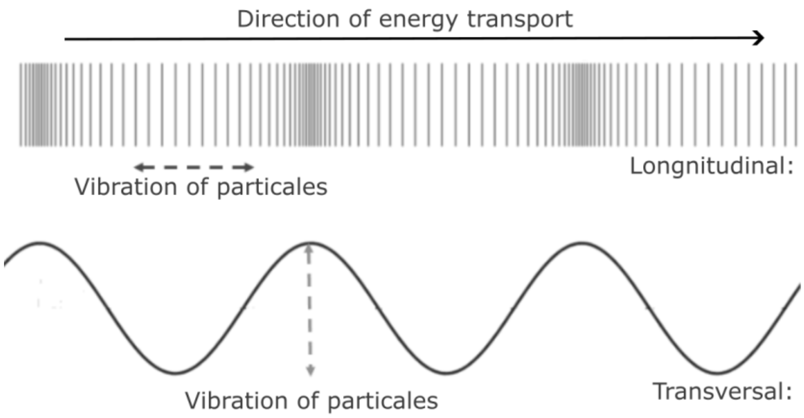

Figure 19: Waveform deformations, modified from [32]

The first waveform is also called compression wave and shows a similar behavior as acoustic waves in fluids. Their general wave function description and definition of the wave speed is given by the following equations 1a and 1b

$$\frac{\partial^2 w}{\partial x^2} = \frac{1}{{c_l}^2}\frac{\partial^2 w}{\partial t^2}$$ *Equation 1*

$$c_l = \sqrt{\frac{B}{\rho}}$$ *Equation 2*

Where the deformation is given by w (also in the x direction), B for the bulk modulus and ρ for the mass density. Having the definition of the bulk modulus in Equation 2, a direct relation of the applied pressure p and the relative volumetric contraction defines. By the combination of Equation 2 and Equation 1b, the increase of sound speed by increase of mass stiffness is explained [31].

$$B_0 = \sqrt{\frac{-p}{\frac{dv}{v}}}$$ *Equation 3*

A problem appears if the vibrational wave lengths exceed one or two of the material dimensions travelling through. From here it makes sense to split structures in two subgroups of volumetrically equal dimension ratios:

- Beams
- Plates

These distinction is for most technical applications (especially considering the test rig environment) a reasonable description of the transversal expansion of the structure along the direction of propagation described by Equation 3.

$$v = -\frac{\epsilon_y}{\epsilon_x} = -\frac{\epsilon_z}{\epsilon_x} \quad \textit{Equation 4}$$

Following the mathematical logic, longitudinal waves in finite structures such as beams and plates are slower than in a physically rare infinite structure. This comes by their differing relative surfaces, surrounded by less stiff material such as air and water which are essentially defined as stress releasing media [31]. For beams and plate structures new equations must be defined as 4a and 4b and added by the Young's Modulus E of Equation 5.

$$c_{l(Beams)} = \sqrt{\frac{E}{\rho}} \quad \textit{Equation 5}$$

$$c_{l(Plates)} = \sqrt{\frac{E}{\rho(1-v^2)}} \quad \textit{Equation 6}$$

$$E = \frac{B(1+v)(1-2v)}{(1-v)} \quad \textit{Equation 7}$$

For typically test rig related structures (manly consisting of steel with a poison ration of $v_{Steel} = 0{,}3$) a longitudinal speed reduction of 10% for plates and 14% for beams, respectively to infinite structures is defined by the Equation 4. Remembering the ability of structural material to resist shear stress, shear waves emerge with the same wave equation as longitudinal waves shown in Equation 1a. They propagate through the structure transversally and simultaneously, but slower than longitudinal waves as their definition relates to the shear modulus G.

$$c_s = \sqrt{\frac{G}{\rho}} \quad \textit{Equation 8}$$

$$G = \frac{E}{2(1-v)} \qquad \textit{Equation 9}$$

$$with\,(G < E)$$

Going onwards more practical applications in finite structures, bending or flexural waves emerge and show a similar transversal characteristic, but a far more complex physical definition as they cause the beam or plate cross-sections to perform an oscillation about the neural axis. Considering the propagation speed of the bending wave, various influences appear as it does not only derive its speed of the Youngs's Modulus and the mass density, but also on their frequency of oscillation ω. This dispersive behavior also comes with a fourth order in space, shown in the wave *Equation 10* (that does not include the wave speed itself) and Bernoulli- Euler definition of the bending wave C_B.

$$\frac{EI}{\rho A}\frac{\partial^4 w}{\partial x^4} = -\frac{\partial^2 w}{\partial t^2} \qquad \textit{Equation 10}$$

$$c_{B_{Bernoulli-Euler}} = \sqrt[4]{\frac{EI}{\rho A}\omega^2} \qquad \textit{Equation 11}$$

Noting, that *Equation 11* only fits for relatively long wave lengths respectively to the beam thickness, the equation gets more complicated when frequencies ω are below 20 kHz (see deviation in Figure 20. If now the shear resistance and the rotary mass inertia would be considered, the equation of the bending wave speed gets very complex and falls out of scope of this thesis. To give a brief overview of the wave speed of bending waves in correlation to the frequency see the analytic results of differing plate structures in Figure 20. So, the conclusion is that structural waves are slower in massive, isotropic, and homogenous material than in thin lightweight material.

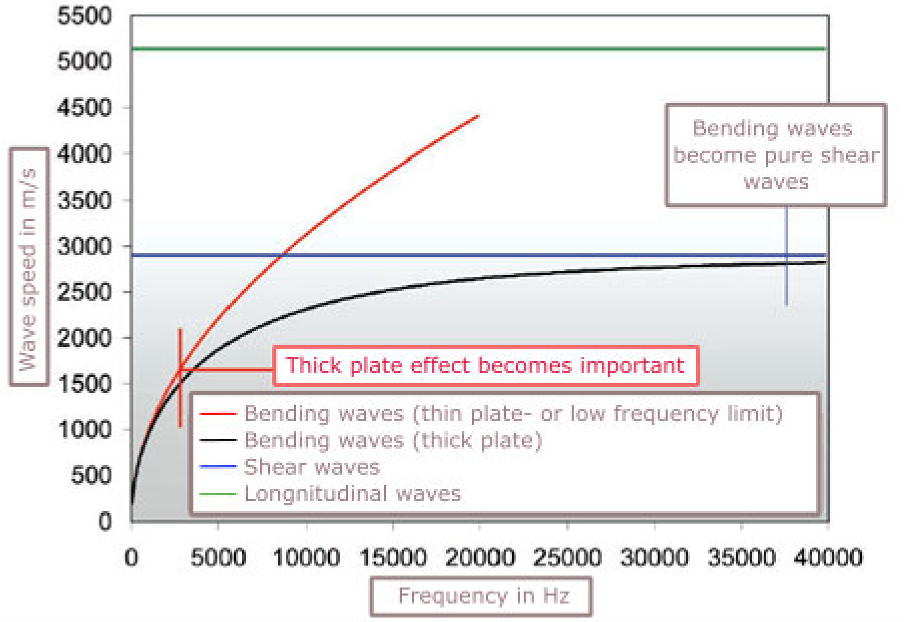

Figure 20: Speed of sound depending on frequency, modified from [31]

Note for later recapture that a vibration measurement system based on piezo electrical devices defines a sensitivity range in correlation with the most relevant area for the speed of sound deviation from 2k to 20kHz in Figure 20 [33]. Next, the intersection of structural connections (supports, gear meshing, flanges, bolts, bearings) brings in reflections and deflections of the wave structures, making a purely equation defined approach for a test rig system impossible, while introducing the modal structure excitation. This introduction of the structural modes again elevates the complexity of the structural behavior. This calls for either numerical approximation via FE simulation or experimental or operational test measurements of the structure's behavior after being excited by external cyclic or fluctuating forces. Also, experimental tests come crucial for non-isotropic and non-homogenous material, such as hydraulic hoses or wind turbine rotor blades, as these structures have highly inhomogeneous stiffness properties making computer based structural modelling (analytic FE- methods) a yet not solved research problem [31]. But for now the author accepts the fact that this thesis does not deal with the simulation of the test rigs structural behavior, the only option to find system parameters is a laboratory test called modal analysis [31]. For further information's of this complex topic a profound explanation is given by Stephen Hambric of Pennstate University [31], Dreisig Et.al. [33] or Brommundt Et.al. [34].

2.5.2 Modal Analysis as a Tool for Structural Analysis

In the last subsection, the introduction of structural modes is given. This comes with the so-called mobility of a structural mass. This mobility concept inherits the effect of structure related cross-mobility points and lead to a certain resonance frequency definition for each structure. As this points depend on stiffness and damping properties of structures (e.g., components of a test rig) and structural intersections (e.g. bolts, flanges etc.), they differ for each state of the structure. Clearly this means, that a different bolt tension torque or load state of the bearing set changes the system response in terms of their damping property. As general damping behavior is subject to many research topics and textbooks of the last decades, a further introduction of this topic can be given by Nashif, Jones, Henerson [35] or Beranek [36] . The most common way of experimental modal analysis is the impulse response process. Besides the ability to Define the internal damping of structure through loss of vibrational energy by deformation, modal analysis provides another two handy outputs. First it utilized to detect natural frequencies or peak responses of a structure (see Figure 21), which can lead to structural failure and predefinition of vibrational measurement results of sensors. Second, it can fade the actual vibration output signals of a dedicated component of the measured system, leading to difficulties with algorithm-based data processing approaches, as these algorithms often work with frequency domain (FD) signal properties. These are depending on complex elastic moduli which thereby lead to complex wave speeds [31] [36]. Finding the statement of Rainer Wirth in [5] bending waves are the dominant wave form of impulse transmission inside a machine structure, a wave speed description for vibrational analysis is also relying on these test methods.

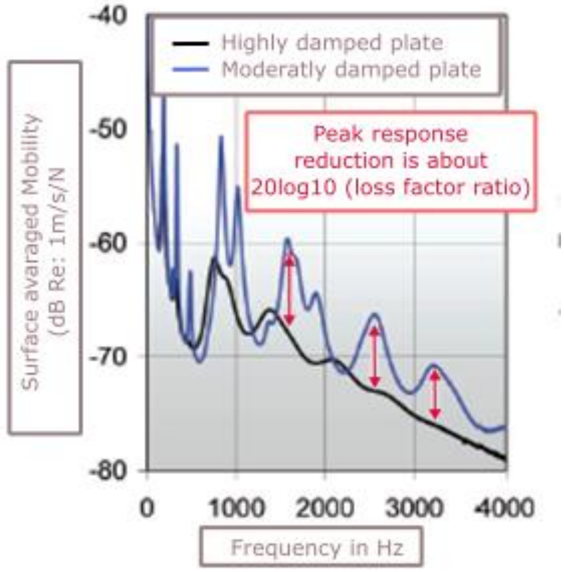

Figure 21: Peak response of highly and moderately damped plates, modified from [31]

Having two possible application environments of an algorithm-based vibration measurement system, the effect of the amount of damping (see Figure 21) comes up. Thinking of a real size wind turbine with non-isotropic and homogeneous structures (like rotor blades) connected to a pitch bearing, the damping rate due to the complex structure properties falls out of scope for this thesis. A considerably solid steel construction, like one of Fraunhofer's basic bearing test rigs, would reduce the complexity of the test environment and is deliberated in Chapter 3.

2.6 Condition Monitoring Systems in Wind Turbines

The purpose of a condition monitoring (CM) is in the first place simply derivable from its name. Parts of a machine are monitored by sensors over a period and thereby mainly defined in its physical state of condition via sequenced trend based or online (real time) analysis. Major topics are security aspects i.e. earthquake detection systems, trip systems, and most relevant for this thesis, scheduling predictive maintenance and fault detection. The importance of CM in wind turbines is due to the cost intensive exchange of faulty components and a lack of income through turbine downtime during such an exchange, especially in remote and complex weather environments as offshore wind parks. These costs are defined through planned and unplanned operational expenses (OPEX) which accumulate with the capital expenses (CAPEX) to the lifetime cyclic costs (LCC). Total maintenance expenses of wind turbines sum up to 25-30% of the total planed LCC, and builds a reasonable lever to increase profit, as *Bachmann Monitoring GmbH* assumes that statistically every 10th monitored turbine suffer from relevant component damages [37]. Besides the structural health monitoring of towers and structures, performed through load cycle counting and S-N curve related processes [38], the vibrational analysis of bearing systems drives the leading amount of CM related measurement processes along the drivetrain system [6].

2.6.1 General Bearing Damage Analysis Approaches

Amongst others the VDI 3832 rule “Measurement of structure-borne sound of rolling element bearings in machines and plants for evaluation of condition“ is widely applicated and defines vibrational measurement processes. But these standards have a shortcoming due to the demand of minimum bearing frequencies of more than 2 rotations per minute In correlation to modern wind turbines main bearing system, with a very low drive frequency of about 0.2 Hz, these traditional rules and standards do not apply [39]. Neither there is one for pitch bearings [6]. A CM process on main bearings is described by Nicolas Waters in his *WindPower* article “A word about sensor selection for condition monitoring systems.” He quotes that most engineers have a rough understanding of signal analyzing via Fast Fourier Transformations (FFT) analysis that helps transforming time domain (TD) vibrational signals to the FD, looking for amplitude peaks in defined areas of the drivetrain frequency outputs. As it is major content of the later performed signal analysis a deeper explanation in the following application related subsections is given. This is what most vibration related CMS do and is the primary approach on slow rotating main bearing systems due to Waters. Later he describes the appropriated type of vibrational sensors used to perform these tasks, which is the main information used in chapter 5. For now, it is enough, to know, that even slowly rotating bearing systems utilize the option of using classical CM analysis and builds the base for later algorithm supported FFT machine diagnosis [6]. Taking a dive into frequency domain-based damage detection, Dr. Reiner Wirth of the TH Zittau provides a traditional but excellent overview of the topic in [5], directed to application engineers in the field of machine diagnosis. Based on these, later reference tests are developed and performed in chapter 6. Besides technical aspects of appropriated measurement chains in the field, he defines the most relevant components for a measurement process. This is the ability of the CM engineer to interpret the data streams via extended physical knowledge of the machine dynamic and mathematical relations along with the analysis. This is important, due to the amount of possible diagnosis process, which shall be selected in relation to the machine’s dynamical behavior. The main diagnosis topic of this thesis is the vibrational- depth diagnosis which is than separated into further sub- topics:

- Machine vibration through solid born sounds
    - (Housing structure)
- Relative shaft displacement
    - (Axial and radial)
- Revelational dynamic
    - (Deviations in shaft speed)
- Torsional stiffness dynamic in the shaft systems

First of these, uses the option of multiple source analysis, as all primary events inside the machine can be captured by their propagation of solid born sound over the structural components to a single position on the structure. A later source separation is than possible by profound frequencies analysis and mathematical categorization. Second, is the relative shaft displacement which is used to localize the area of damage along a complex drivetrain more precisely but demands more sensors and relatively complex measurement environments. This and the other approaches in the list have very little in common with pitch bearing measurements along the bearing ring and will be outlined for this thesis. To help the author and field engineers to pre- select the approach for a test rig system or a wind turbine bearing system, Wirth is defining three primary events along with the physical effects to expect. These are defined by:

- Harmonic force excitation
    - (e.g. unbalancing, misalignment, surrounding fluid turbulences)
- Modulated force excitation
    - (e.g. gear meshing with drive frequency)
- Impulse excitation
    - (e.g. overrolling of raceway or roller defects, cage failure)

Anticipating to the selection of a simple suitable test environment for this thesis and the findings of dominant damage modes of a pitch bearing in chapter 3 and section 2.4, the first and the latter are the most relevant effects on the examined bearing defect [5]. Finding the mathematical description, the effect of superposition is defined in *Equation 15* of the harmonic force excitation and multi- signal modulation which is related to impulse excitations in junction with e.g. the drive frequencies in *Equation 16* [5].

$$x(t) = x_1(t) + x_2(t) + \ldots + x_n(t) = \sum_{i=1}^{n} x_i(t)$$ *Equation 12*

$$x(t) = \hat{x}_T cos(2 \cdot \pi \cdot f_T t + \varphi_T) \cdot [1 + \hat{x}_M cos(2 \cdot \pi \cdot f_M t + \varphi_M)]$$ *Equation 13*

So, the first is also a relevant topic when it comes to transfer of measurement approaches to a large test rig or wind turbine with high gear meshing and hydraulic or aerodynamic whirl related vibration shares. For this thesis, a brief explanation of the impulse excitation and its modulation as well as the possible analysis methods is sufficient and defined in the next subsection.

2.6.2 Impulse Related Damage Detection

While two solid bodies collide, they create a shock pulse. This is, for example, the case when each roller passes a defect on a bearing raceway. The flank deviation of the vibrational acceleration is a quantification for its frequency response. Having knowledge about this area of the frequency response creates the ability to examine the eigenfrequencies of a structure which amplifies the impulse in this specific frequency band. As a quick recall, the test rig housing structure is very stiff and expects thereby a high eigenfrequency bandwidth, with the effect of low LF contents. This gives the impression of a low vibration amplification of this specific and most relevant area. On the other hand turbine structures are expected to be partly softer, hence this may simplify the detection LF vibrations at this basic state of the examination. To understand the theoretical approach of the frequency response, the convention of an impulse convolution is introduced and defined in *Equation 14* [5].

$$y(t) = \int_{-\infty}^{\infty} x(\tau) \cdot h(t-\tau) d\tau \qquad \text{Equation 14}$$

This linear time variant system with the unit pulse transfer response $h(t)$ demands for an infinite pulse, called Dirac pulse. As this Dirac pulse is physically impossible to induce, the unit pulse transfer can't be calculated, calling for an experimental approach with a real shock impulse of an ideal hard pin. Note, that a real will not excite all relevant spectra of the frequency range. This is predefined in subsection 2.5.2 and now transferred to a bearings outer ring of the bearing ring. The impulse response in time and FFT transformed FD is displayed in Figure 22. The TD shows the acceleration amplitude declining through damping. And below the frequency response defines fine peaks for the natural frequencies, between 1800 and 5000 Hz. Note that the 7220- type bearing [5] has very similar dimensions to the 23026-pendulum roller bearing with 200 mm outer bearing diameter, so this frequency response is assumed to be transferable. Hence the main frequency range is located within the limits of the data rate reduced DAQ system of the BEAT0.1.

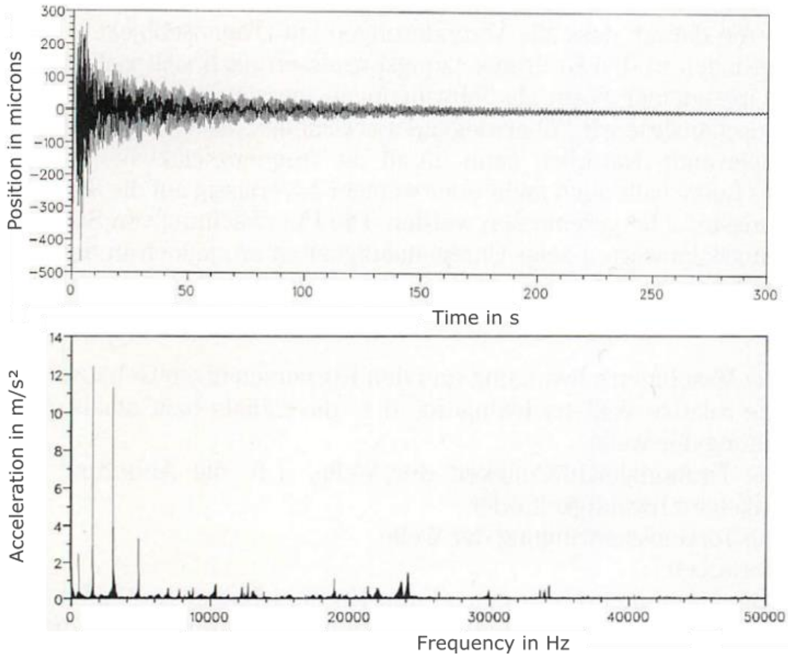

Figure 22: Impulse and frequency response 23026-type outer ring, modified of [5]

Rethinking the definition of frequency dependent sound speeds inside a solid body, the impulse response of two spatially separated sensors might help detecting the signal delay of the wave propagation between them. So a number for a runtime difference between vibrational signals might be defined in the application subsection 6.2.1. Now the definition of the eigenfrequencies is clear, leading to the effect of rotation induced harmonic vibrational patterns. Aiming for the detection of a harmonic primary event, which correlates with the defect of a component, a further processing method is needed. As harmonic events are described as additive sinusoidal components, a FFT analysis enables the examination of frequency and energy content of the peak signals, related to the number of repetition, within a defined signal length [5] . Without getting to deep in the mathematical description (see therefore paragraph 4.2 in [5]), the output of the interpretation of *Equation 13* with a modulated integer frequency form f_M reveals three spectral components. First is the carrier frequency f_t, left side band frequency $f_t - f_M$ and right sideband frequency $f_t + f_M$. This will create three peaks, instead of two in the signal, for this integer case. But most measured frequencies will not match an integer criteria, creating a abruption effect that creates a dispersion of the observed main vibrational amplitude into a several declining peaks around this expected single peak amplitude (see Figure 23).

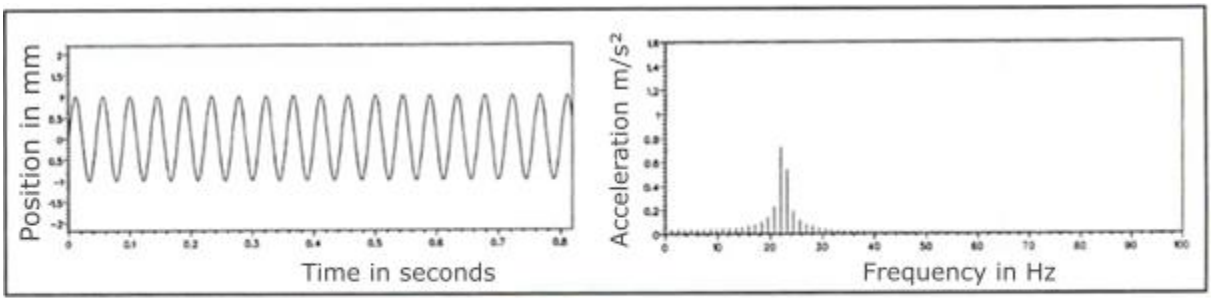

Figure 23: Abruption effect of a single dispersed non- integer sinusoidal wave [5]

Even though a single input harmonic is given, the definition of an output peak frequency is impossible, calling for a windowing function like e.g. Hann, Hilbert or Hamming window functions [40]. This function takes a certain order of the highest non- zero values of the FFT or DFT function and smoothens the signal to a more defined peak. The definition of the window order is complex process and leads to an application advice in [41]. For signal processing with *Matlab* or *Python*, a simple function block is given with the inherited Hilbert window function, aiming on spectral analysis. This function is called the envelope curve function and is used to pre- process coarse vibrational TD signals for FD transformation. It is the base for a powerful tool in vibration analysis, the BEA. This tool is superior to basic signal processing approaches like vibrating strength methods or the crest method, especially when it comes to LF vibration examination [5] [6]. Following Figure 24 shows the difference of a purified signal via BEA vs. the spectral analysis of the original signal with an overrolling pulse frequency of 52 Hz of a standstill bearing outer ring, such as the BEAT0.1 configuration.

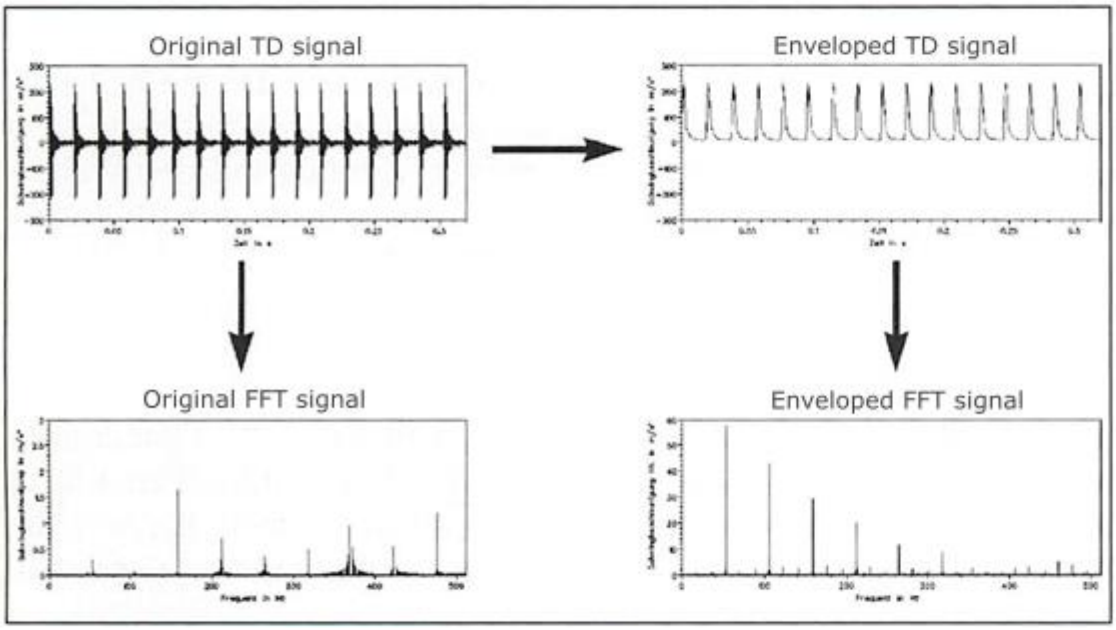

Figure 24: Signal purification, BEA with 52 Hz impulse frequency, modified of [5]

Obviously, the non- BEA spectrum of the original signal does not majorly detect the overrolling frequency of the defect at 52 Hz. After the envelope processing with a suitable Hann window function, the peak and its harmonics are clearly displayed in the lower right corner of Figure 24. These harmonics origin in the FFT structure and are also a topic of the data processing chapter 7. Now the same bearing configuration and parameters are used for an inner ring defect measurement. So another case of a spectral analysis related phenomenon, as described earlier, appears with the modulation of a continuously over rolled defect like shown in Figure 25. The modulation creates the side bands and is derived from the drive frequency which, in case of test bearing with inner gear meshing or the later introduced BEAT0 test rig bearings, moves an inner ring raceway and its defect relatively to the rolling body. The drive frequency is defined with a low frequency, building closely located sidebands to the overrolling frequency of the defect at 52 Hz.

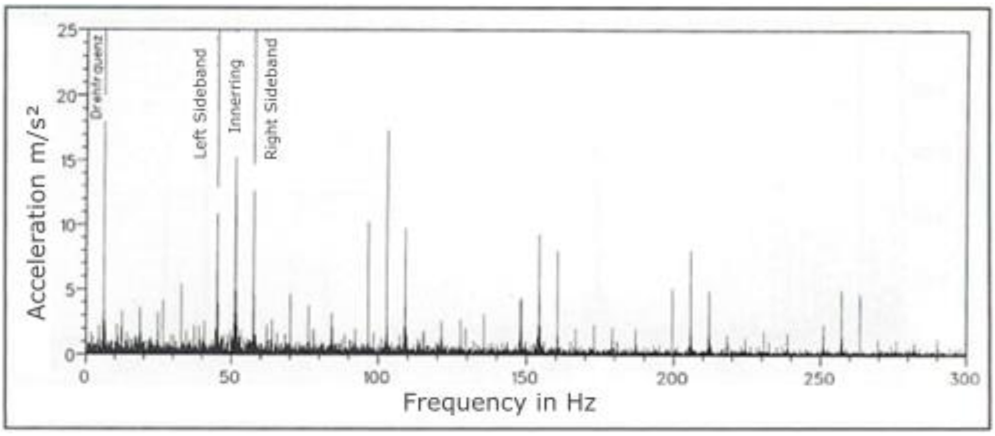

Figure 25: Inner ring defect with modulated side band frequencies, modified of [5]

Now the effect of the modulation, in line with the integer harmonics appears and create peaks along the frequency response range. Note, that the first group of spectral line families does not always define the highest peak. Another special case is the non- homogenous load distribution of a bearing, resulting in roller slip and a so called discontinuous overrolling impulses along with the TD signal. This also happens in dynamic changes of the bearing’s load direction. For the case of the test rigs high load zones, this is unlikely to happen and is therefore cut out of scope for the thesis. What comes crucial in most CM systems, is data trending. Therefor the energy levels of the vibration signal in the FD get frequently stored and checked about deviations within or above a defined threshold [6] [37] [42]. Considering the frequently performed pitch cycles with constant speed at cut in or cut out windspeed, this method could be used along with WT related CM strategies. For now the relevant annotation of the phenomena is sufficiently defined and bases the later signal examination.

3 Test Environments at the Large Bearing Lab

3.1 Purpose of a Test Rig

The Fraunhofer IWES's large bearing lab has, as the name concludes, its aim on research for large bearing systems. The definition of a "large bearing" defines the diameter of the bearings tested on specially therefore developed test rigs. Originally the idea of a pitch bearing test stem from a cooperative test bench for true size wind turbine pitch bearings of the Senvion company located at the head quarter of the IWES in Bremerhaven. This test rig had the ability to rebuild simple load cases as bending moment and thrust forces by a set of tensioned ropes, connected to a real size turbine blade. Even though this test rig design showed a high grade of similarity to a real turbine application this initial test rig design had shortcomings in terms of dynamical load application in multiple degrees of freedom due to control and interface limitations.

Figure 26: First blade bearing test rig in the IWES lab Bremerhaven [11]

From there the idea of a hexapod test rig, with the ability to cover all degrees of freedom, emerges [11]. This design can execute a defined test profile under realistic load situations of a real wind turbine. This high demand on a full component validation, which is based on the V- model design loop according to VDI 2206, drives the development of a bearing endurance and acceptance test rig (BEAT) project located in Hamburg. Besides this full-size acceptance test rig, smaller test rigs with diameters below one meter emerge for functional and parameter isolation purpose on lower costs per test set up (for further information see dissertation of Stammler 2020 [11]).

3.2 Test Rig Design Requirements

To understand the demands to a test rig design, it is crucial to define the expected outcome of a test. There are two main groups of test rigs. One is the function test rig design, with full size wind turbine components fulfilling an acceptance and endurance criteria, and another test rig design which aims on a specific property by the examination of demarcated test parameter, performing on smaller industrial grade bearing types for basic low-cost parameter analysis. Following sub chapters 3.2.1- 3.2.2 define the scope and boundaries or rather limitations of the specific test rig designs, for the criteria of a suitable vibrational test environment in respect with the time scope of this thesis. Focused criteria of the test rig environment selection can be defined by the following and help the later selection for the following vibrational measurements:

1. Reproducible damage modes
2. Possible integration in existing measurement systems
3. Sufficient DAQ capability
4. Simple test assembly of bearing sets
5. Low-cost test setup

3.2.1 BEAT6.1

Although Stammler sufficiently explains the design requirements of the BEAT6.1 in his dissertation [11], a short introduction of the test rig system and its capabilities are given in the following, because later chapters of this thesis will refer to this specific test environment. The numeric code 6.1 of this large BEAT stems from its test capability of the pitch bearing diameter. A diameter of 6,5 meters be tested on this first version of the design principle, with very little limitation to the actual pitch bearing designs shown previously in [11] to the load and motion cases of a real pitch system inside a turbine (except real aerodynamic vibrations) [11]. Following rendered CAD model shows the main components of the BEAT6.1 in Figure 27. It consists of a load platform that can perform all dimensional movements, which then creates reaction momentums of a maximum of 50.000 Nm or radial and axial forces against the fixed reaction frame. These forces are applied by six hydraulic cylinders called load application system (LAS) forming a hexapod platform. In between there are the two-interface adapters which simulates the stiffness of the hub. Connected to these there are two bearings connected, named devices under test (DUT). These DUT are bolted with a force transmitting element (FTE) that simulates the rotor blade connection stiffness of a real turbine. In the back, the hydraulic pressure unit (HPU) supplies the servo valve-controlled LAS and hydraulic pitch cylinder. This pitch cylinder creates the rotational movement of the DUT’s inner ring and the FTE. Internal connection plates enable the optional use of an electrical gear driven pitch drive [43].

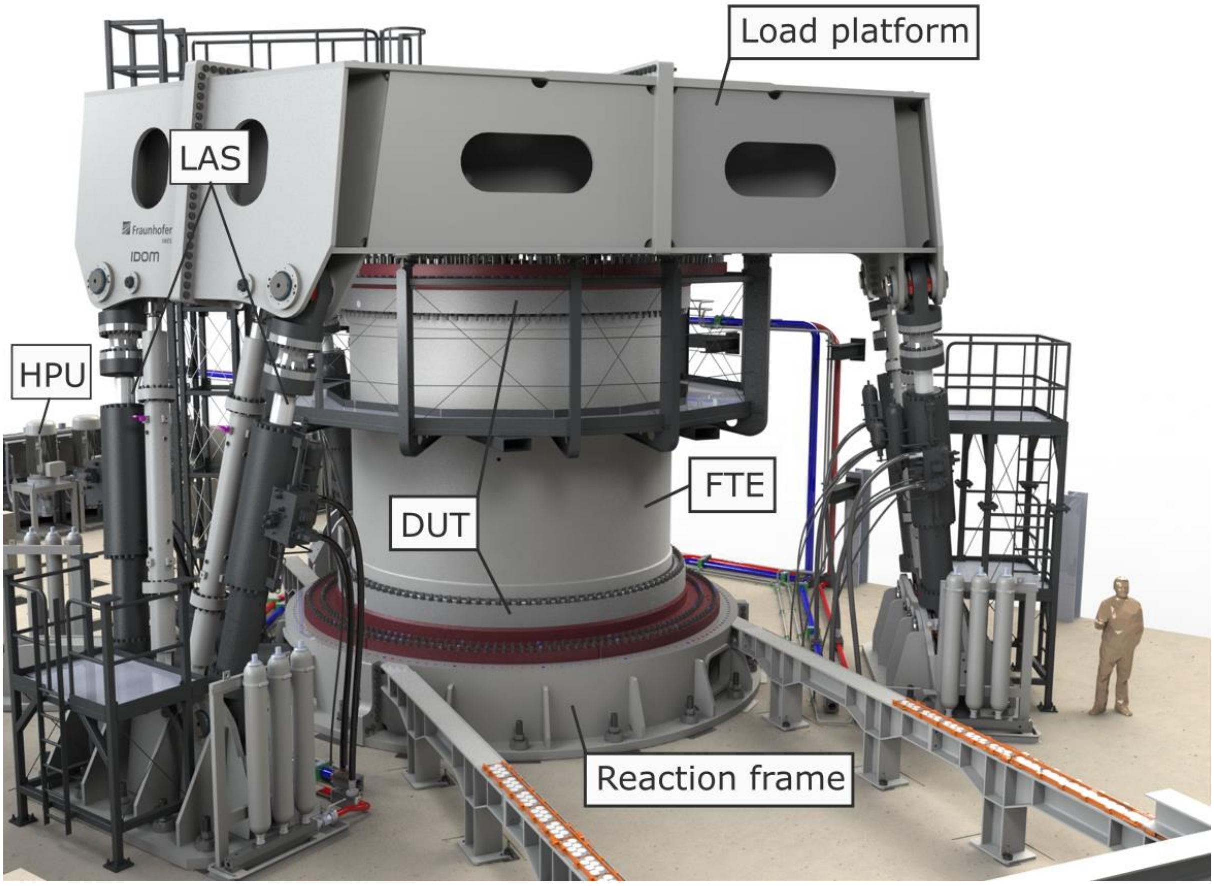

Figure 27: Render of BEAT6.1 and peripheric source of vibrations, modified from [43]

This design aims for the highest similarity level of a real turbine application and is equipped with original components such as bearings and pitch drive units. Consequently, the similarity of the vibrational machine dynamical behavior in term of vibrations is given. Clearly, a stationary test rig system differs from a real pitch bearing system in the field, i.e. aerodynamic, main bearing, gear and YAW- drive vibrations are not available. Nevertheless, the contact vibrations of the pitch bearing could be separated from pitch drive noise and the noise source of the HPU and valve related whirl noise along with the LAS, enabling a “close to reality” contact vibration measurement system validation in a controllable test environment. In addition to this capabilities, the BEAT6.1 rig is equipped with five hundred analog and digital high frequency measurement channels up to 100kHz and a backup database to store large datasets of several months in unsupervised acceptance test operation [23, 44]. Considering the first selection criteria of chapter 3.2, damage modes shall be qualitatively reproducible. To this no contradiction can be defined yet, this test rig is the most complex and precise pitch bearing test rig on the globe with the possibility of wear and RCF production by dedicated pitch and load profile combinations [44]. Criteria number two consists of the possible integration of a vibrations measurement system. Therefore some of the mentioned five hundred channels will be available and sufficiently precise, while the fully integrated large database fulfills criteria three. Focusing the 4^{th} and 5^{th} selection criteria for a suitable test environment from above, one should know about the assembly time for one bearing test, adding up several months of preparation, assembly, and system commissioning. Besides the costs for these real size components, as the two-pitch bearing can be priced up to a half a million US-

Dollars, the overall costs add up to a multi-million range. Considering the time scope of this thesis, the financial limits, and the demanded complexity of a trial-based measurement system within a master's thesis, a direct and fully thesis bound test on this large-scale test rig is not realistic, neither rational. Nevertheless, after the successful implementation of the measurement algorithm on a smaller test rig type, this step is improving a large test rig or real turbine application to a next level (see the chapter 8 and 9 for further information).

3.2.2 BEAT0 Series

As mentioned in subsection 2.4.1 the x/2b ratio enables the transfer of contact phenomena from large ball and roller bearing types to smaller scaled bearings [11]. This interconnection allows to examine smaller scale bearings under similar load conditions and derive knowledge from these results. It is clear, that some influences of a load or motion profile shall be better understood, before being applied to a half a million-dollar pitch bearing set on BEAT6.1. Having the possibility of performing multiple tests within days instead of one test per half year drove the development of a basic roller bearing test rig in 2018. This test rig was partly developed and upgraded in a later bachelor's thesis by the author, so render models and design features do not need a direct quote. Due to its design, it can perform oscillating movements as well as full rotation via a gear supported servo drive. This basic test rig, shown as partly cross sectioned render model in Figure 28, is called BEAT0.1. It derives of its test bearing diameter of less than one meter. The index ".1" indicates that this is the first version of this design. This test stand is used for manually applied hydraulic initiation of static axial forces of up to 120 kN [Fax] in any variation of rotational patterns small oscillatory movements. Because of the high-resolution *SPINEA DRIVESPIN®* encoder and reduction gear, it is possible to carry out precise cycle tests [45]. The housing (Pos. 9) dimension enables to evaluate both, angular ball bearings (Pos. 5) and tapered roller bearings. For the thesis roller bearings be ruled out, due to the broader knowledge of contact and damage behavior of the ball bearing type. The test rig, equipped with these ball bearings is presented in Figure 28 and will now be further explained, as its general properties meet the needs of a basic test environment for a defined vibrational measurement set up.

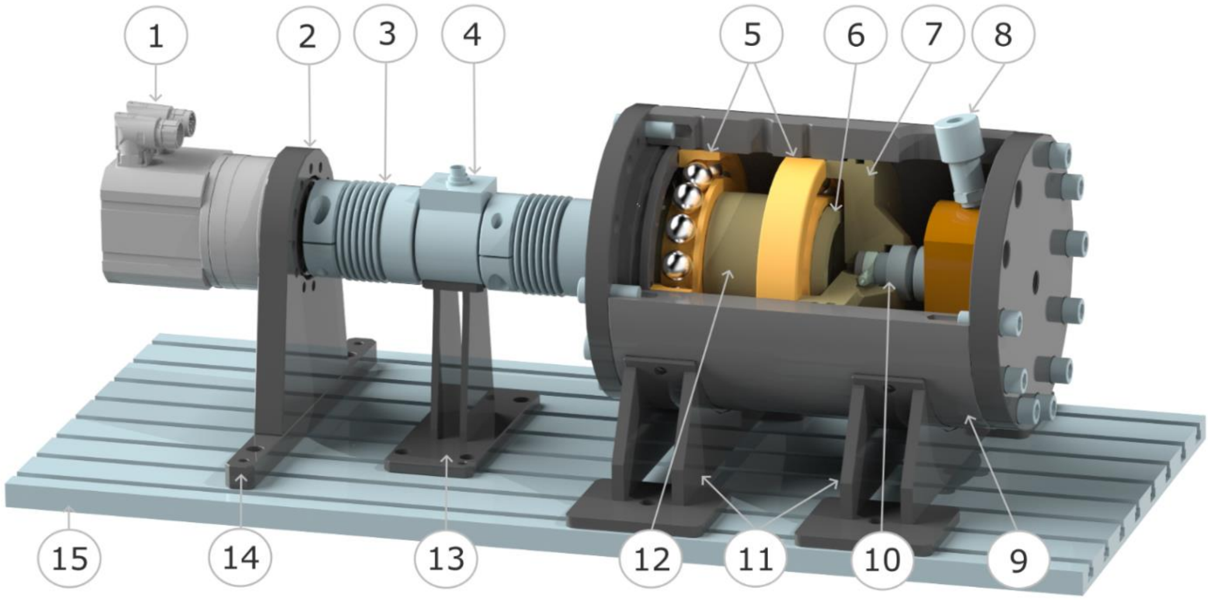

Figure 28: BEAT0.1 axial load test rig with gear-servo drive

The drive assembly essentially consists of a servo motor (see Pos. 1 in Figure 28) and two torsional stiff steel bellows couplings (Pos. 3). The option to measure the torque is given by a HBK T22-type torque sensor (Pos. 4). It transmits the dive torque to the main shaft with the test bearings (Pos. 5) mounted in X- configuration on it. Pos. 8 &10 shows the axial hydraulic cylinder and swivel peace which induce purely axial loads with up to 120kN. The servo motor has an internal angle encoder, with an accuracy hysteresis of < 0.025 °. The reduction gear (shown in Figure 29) allows high load cases and defines the technical specification of the drive system derived from technical datasheet of *SPINEA DRIVESPIN®* servo gear 070-series, while the gear stages are shown in the following Figure 29. Comparing with the planetary mashed type of Figure 7, a far similarity of these multistage reduction gearboxes could be derived, and so could their vibration or noise emission to the examined bearing system. Even though the similarity is given, the gear type totally differs, as Spinea uses rollers as gear meshing of a trochoidal gear type. Unfortunately, the Datasheet only provides the input output gear ratio, so the frequency bandwidth of the internal gear stages can't be derived or defined by the specification information's in [46].

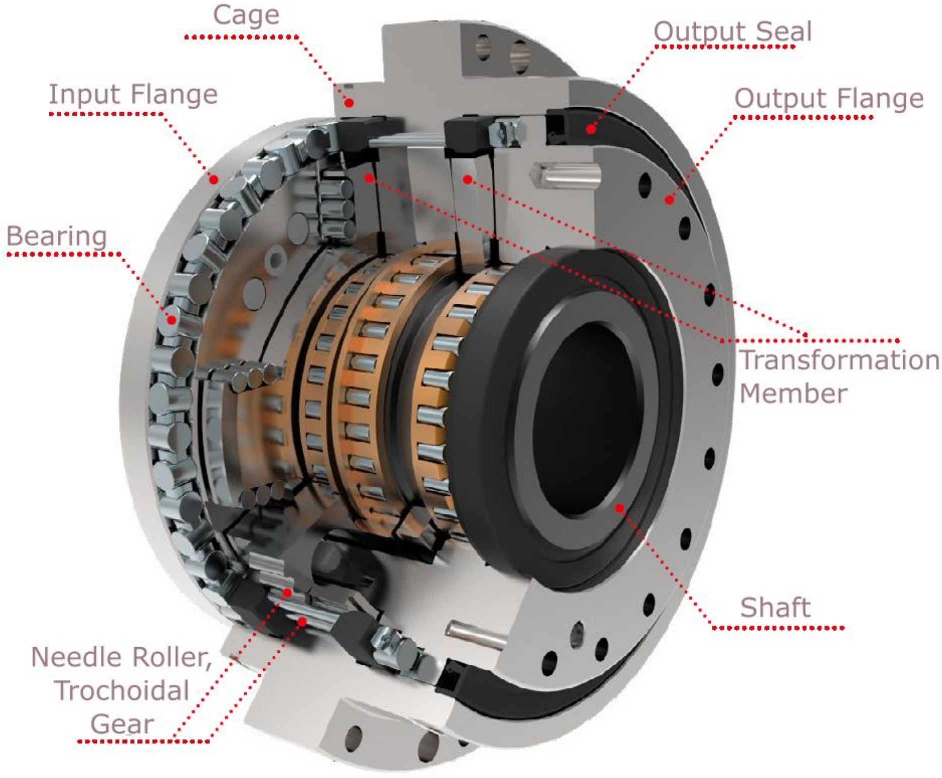

Figure 29: Cross section of SPINEA DRIVESPIN® M-Series reduction gear [46]

Table 2: BEAT0.1 gear properties [46]

Rated properties		
Output torque	50 Nm	
Input speed motor	2000 rpm	12000 °/s
Output speed	35,087 rpm	210.52 °/s
Reduction ratio	i=57	
Tilting stiffness	150 Nm/arcmin	
Torsional stiffness	22 Nm/arcmin	
Hysteresis	< 0.025°	

The torque sensor (type HBK T22) measures the applied torque of up to fifty Nm. It is located at Pos. 4 between the steel bellows couplings Pos. 3. The torsional rigid couplings can compensate for small angular misalignments between drive shaft and the bearing equipped main shaft Pos. 12. The bearing assembly contains the grease lubricated angular contact ball bearings of 7220 type (see dimensions Pos. 5 of in Figure 31). These bearings are explicitly discussed in Chapter 3.3. The static force is applied by a hydraulic lifting piston cylinder (Pos. 8) that transduces the desired axial force [Fax] up to 120 kN through the applied oil pressure. The introduced power flow goes over the spherical pendulum pressure piece through a load cell (Pos. 10), to the pressure plate (Pos. 11) and then on the outer ring of the bearing. The pendulum pressure piece enables a fully axial force application due to the spherical shape and an even distribution of the contact force on each ball [11].

3.2.3 Final Selection and Sources of Vibration

Examining the general sources of vibrations around the BEAT0.1 test rig system, the demand of a basic test environment is fulfilled. Leaving the possible noise immigration over the foundation and the tiny roller bearings inside the torquemeter off scope, then in fact, there is only the drive related active noise source which has a major impact on the desired examination of the contact related bearing vibrations. Having a simple noise isolation option for each component comes crucial to investigate the noise sources solo and later use this data to validate the possible results of a separation algorithm.

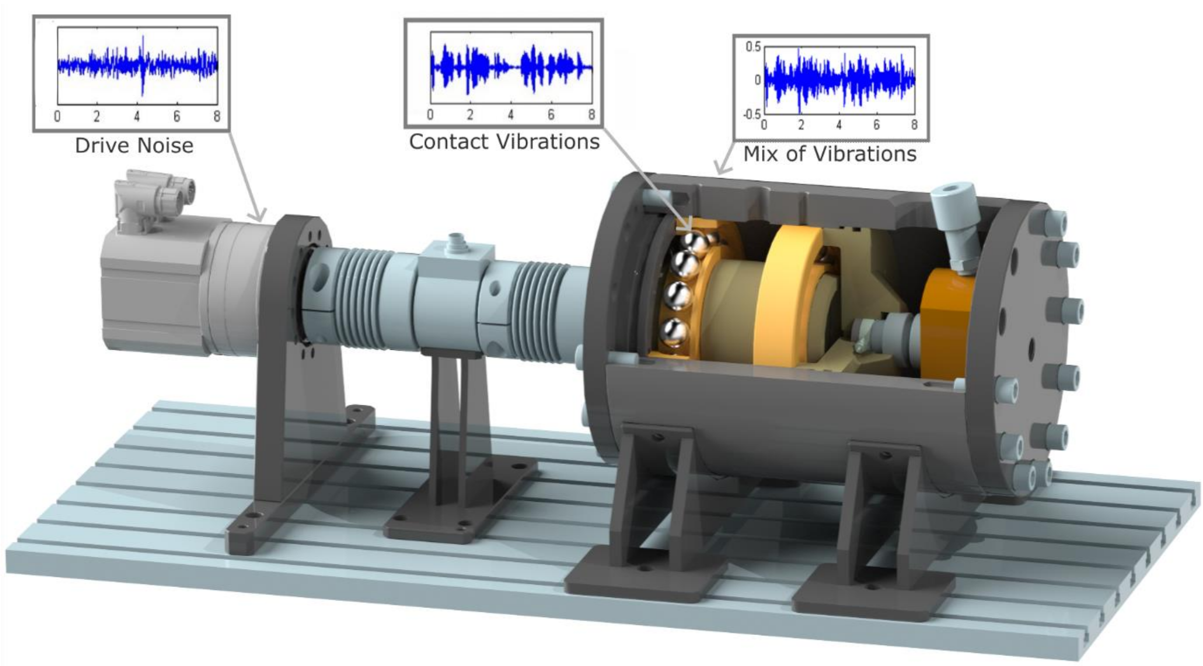

Figure 30: BEAT0.1 test rig with sources of vibrations

3.3 Test Bearing Geometries and Kinematics

The further description of the test bearings geometry and derived kinematic properties is an important step to conceive the tests performed in Fraunhofer's Large Bearing Lab. Especially the roller speed and the associated ball pass frequencies, relatively to raceway damage zone come with the upmost importance in terms of vibrational damage verification in the test developing chapter and result examination in chapter 6 and 7 [5]. Having the example of an angular contact angle bearing with the ISO specification of a 7220 series, kinematic relations can be calculated with the dimensions shown in Figure 31.

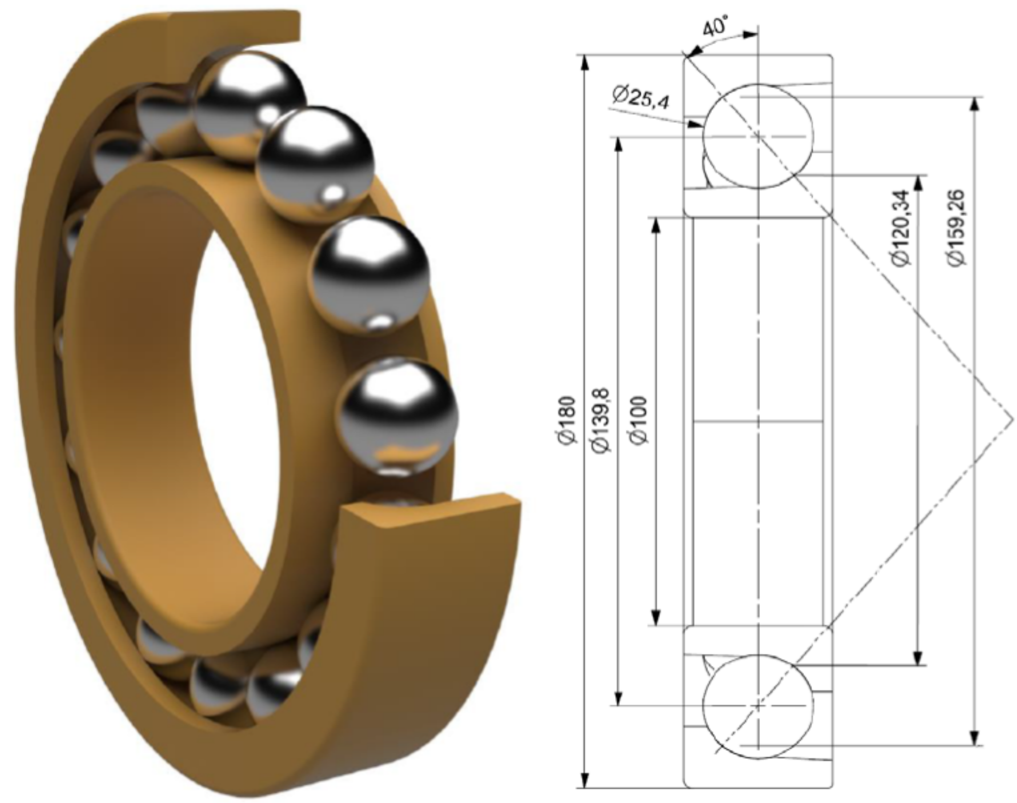

Figure 31: Dimensions of 7220 type ball bearing [21]

These bearings have a contact angle of 40° (see dotted line in Figure 31) and a plastic cage (not shown in Figure 31) that holds the 15 rolling elements at regular intervals of 24° along the raceway. Its outer diameter is 180mm with a shaft diameter of 100mm. There are three additional information's for the later performed kinematic description of the rollers, which is necessary to perform later function tests in chapter 6. These are the contact diameter of the roller/raceway combinations. One is the outer contact diameter D_{Outer} is 159,26mm, second the inner raceways D_{Inner} is 120,34mm, and last the ball's center diameter (pitch diameter D_{Pitch}) of 139,8mm [21]. Note that these three diameters are measured in unloaded condition. The values change with external load applied. These changes have not yet been quantified completely [23], but they are irrelevant for a rough compare of the kinematic properties compared to a full-size pitch bearing. The full- size pitch bearing structure is defined in Figure 10 with a standstill outer ring and a driven inner ring in relative movement to the rollers. Its pitch diameter is 5 m, assuming this for a standard diameter for 10+MW offshore turbines of the most recent generation.

3.3.1 Comparison of Roller Speeds in Test Bearings

Considering later test structure developments in Chapter 6, the information of the rolling contact speed on the inner raceway V_i is an important value to compare both systems. This also is used in the outlook Chapter 9. Anyway, for now the calculation of this roller / ring speed ratio full fills the need of this thesis. This ratio differs significantly between the small 7220 test bearing and a pitch bearing. The so-called ball/ring diameter ratio highly differs between the two bearing types, hence their kinematical description does as well. Figure 33 defines a basic scheme of the kinematic relation of angular speed of a rolling body in a turbines blade bearing or the drive speed of a small bearing test rig. The tangential speed of the inner ring is V_i is the product of the angular speed $\dot{\rho}$ times the inner contact radius r_i. [47]

$$V_i = \dot{\rho} \cdot r \qquad \textit{Equation 15}$$

In a general approach related to rollers on planes or very big pitch diameters with small roller diameters, the outer roller motion is set to zero, hence the tangential speed on an inner ring V_i is defined by the kinematic relation of the vectorial addition of the roller center speed, also known as cage speed V_C with the rolling body speed V_{rb} derived from the diameter D. Therefore the simple relation of the tangential speed of $V_{rb,pb}$ is half the translational speed ($V_i \cdot 0{,}5$). This rolling body speed is the equivalent of the way $\dot{X}_i$ the ball rolls along the raceway in a certain time span [47].

$$\dot{\rho}_{rb} = \frac{V_{rb}}{0{,}5 \cdot D} = \frac{V_i - 0{,}5 \cdot D}{0{,}5 \cdot D} = \frac{V_i}{D} \qquad \textit{Equation 16}$$

$$V_{rb,pb} = 0{,}5 \cdot V_i = 0{,}5 \cdot \dot{\rho} \cdot r \qquad \textit{Equation 17}$$

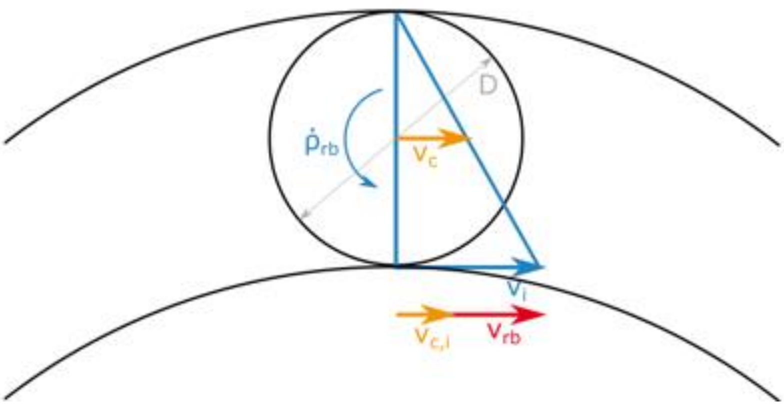

Figure 32: Kinematic scheme of full-size pitch bearing and 7220 bearing series, [23]

Having the smaller 7220 bearing dimensions in mind, this simplification does not fit due to an add up of the outer rings tangential speed component. Now *Equation 17* must be updated by the ratio λ. This ratio is defined by the bearing geometry and defines for a 5-meter pitch bearing with 80mm ball diameter a neglectable value of $\lambda_{pb} = 0.012$. For the 7220 bearing it is $\lambda_{7220} = 0.139$ [47].

$$V_{rb,7220} = 0{,}5 \cdot \dot{\rho} \cdot r \cdot (1 + \lambda)$$ *Equation 18*

Now the definition is set and provides the Option to compare a simple motion case of a 5-meter WT bearing with the drive speed test parameter in a BEAT0 test environment. Anticipating later test program structure the example of a the pitch angle adjustment from standstill to idling ($90°$ to $\sim 65°$) or emergency brake event at a speed of around $\dot{\rho}_{pb=} 4\, deg/s$ is calculated for *Equation 17*. Comparing to this, a test profile related roller speed for the BEAT0 test bearings with an angular drive speed of is defined by *Equation 18*. (Note that the linear relation of *Equation 19* to *Equation 21*, allows to describe the pitch angle speed and ball pass frequency for an IPC motion at around quarter or half of the emergency brake speed [45]). Taking these results in account, the difference of an overrolling speed of a defect on both bearing types is very similar and provides a solid base for later thesis related test developments.

$$V_{rb,pb} = 0{,}5 \cdot \frac{4\, deg}{s} \cdot 2{,}5m = \frac{5m}{s}$$ *Equation 19*

$$V_{rb,7220} = 0{,}5 \cdot \frac{100\, deg}{s} \cdot 0{,}12034m \cdot (1 + 0.139) = \frac{6{,}85m}{s}$$ *Equation 20*

3.3.2 Ball Pass Frequencies of the Angular Contact Bearing

In traditional FFT- based CM processes [5] as well as the further examinations of this thesis, the ball pass frequency affects in terms of sensor selection, data processing (see chapter 5) and source separation validation. It allows to define the overrolling frequency for components like the inner ring f_I , outer ring f_O, and roller defects f_R by their bearing type related geometrical correlation. The cage pass frequency can also be defined but does not find an important role in this thesis and is outlined. To calculate these three, a set of values shall be extracted from Figure 31. Most relevant values are the pitch diameter D_P, roller diameter D_R, drive frequency f_{Drive}, number of rollers z and the contact angle α_C of the 7220-bearing type [5].

$$f_I = 0{,}5 \cdot\ f_{Drive} \cdot z \cdot \left(1 + \frac{D_R}{D_P} \cdot \cos \alpha_C\right)$$ *Equation 21*

$$f_O = 0{,}5 \cdot\ f_{Drive} \cdot z \cdot \left(1 - \frac{D_R}{D_P} \cdot \cos \alpha_C\right)$$ *Equation 22*

$$f_R = f_{Drive} \cdot z \cdot \frac{D_P}{D_R} \cdot \left[\left(1 - \frac{D_R}{D_P} \cdot \cos \alpha_C\right)^2\right]$$ *Equation 23*

The design of a reference tests is described in chapter 6 and demands for the results of the ball pass frequencies. In relation to the beforementioned motion state of the test bearing in chapter 3.3.1 the drive speed of $\dot{\rho}_{7220} = 100\frac{deg}{s}$ and a reference value of $\dot{\rho}_{7220\_ref} = 10\ deg/s$ is selected. (Note that this reference is a non-correlated, scientifically based value and has its origin in demands of relubrication of the contact at low impact energy levels inside the rolling contact [11]). Hence, Table 3 for the output values is generated and provides the appropriated values for the data processing chapters 6 and 7. Additional to this, the drive frequency at the output shaft is quickly correlated to $\dot{\rho}_{7220} = 100\frac{deg}{s}$ and $\dot{\rho}_{7220\_ref} = 10\ deg/s$ with the frequency values $\boldsymbol{f_D}$ and listed for later reference.

Table 3: Ball pass frequencies over drive speed

$\dot{\boldsymbol{\rho}}$	$\boldsymbol{f_D}$	$\boldsymbol{f_I}$	$\boldsymbol{f_O}$	$\boldsymbol{f_R}$
$\mathbf{100\frac{deg}{s}}$	*0.278*	2.373	1.793	1.499
$\mathbf{10\frac{deg}{s}}$	*0.0278*	0.237	0.179	0.149

4 Definition of a Suitable Machine Learning Algorithm

4.1 General Definition of Machine Learning in Wind Turbines

Nowadays artificial intelligence (AI) is a buzzword that finds home in a vast amount of technical research project and applications. It hosts several subtopics which are interconnected and overlapping. In wind energy, the applications reach from the supervision of the production process, to yield performance optimization, load calculation for lifetime prediction as for e.g. in respect to the estimated life time defined by the IEC 61400 standard through condition monitoring solution in the field of predictive maintenance [48] [49]. Last mentioned account to the “predictive analysis” type and build a major branch of AI based supervised and unsupervised machine learning applications. The advantage comes with live machine condition overview of degradation processes and faulty machine states such as rotor imbalance, yaw misalignment or bolt connection state. As described in the earlier CM chapter, this data sets enable to react before defects appear randomly and produce high costs. While some approaches rely on today’s standard signals as for example low frequency SCADA data [50] [51]. No matter if data sets are recorded in LF SCADA data or in HF CM systems, the predicted lifetime of a turbine of 20 years produces countless data points that need pre, post, and cluster processing. This is the key in AI, as large datasets can be clustered efficiently and e.g. adapt thresholds of alarm states via general machine state information’s [50]. In terms of vibrational data, the expected and predefined sampling frequencies are very high and reach up to 20 kHz per sensor [48] [52]. This demands for very efficient algorithm structures and extensive developments in terms of algorithm adaption to the examined base problem. Consequently the following subchapters will introduce a promising algorithm structure for HF l processing and separation of the test rig vibrational signal.

4.1.1 The Traditional Cocktail-Party Effect

The cocktail party effect is structurally defined by the ability of the human brain to perform a selective and intelligent use of the auditory sense in the physiological acoustic frequency range from 20 to 20,000 Hz. It constantly performs a source separation of the environmental sound sources, even though it’s only source of information is the overall sound mix of the total environment [53]. Having the example of a cocktail party, where human voices and a piano interfere in a defined room, provides an easy example to the rudimentary physical phenomena of the intelligent reduction of background noise performed in a human brain (see sketch in Figure 33). This reduction can reach up to 15 decibel (dB), thus an amplification of the focused signal, e.g., a human speaker in the room, by factor three is possible [53]. Besides the capability to reduce noise and focus on a speaker, locating the speaker in the room requires using both ears equivalently. Further our brain manages to filter reverberations from walls or ceilings of the mixed sound signals entering the ear drum [53]. When transforming this effect into a technical structure comparable ear-/ brain analogue a combination of two microphones as the signal recording and a computer as a signal processer (see sketch in Figure 33) comes closest to the physiological system.

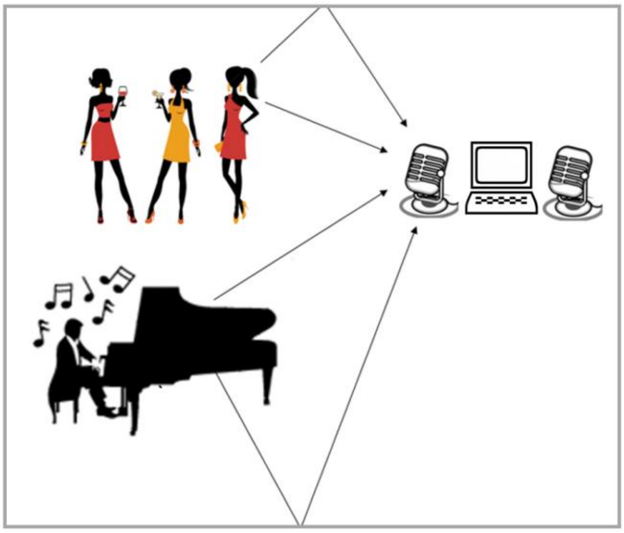

Figure 33: Basic recording environment with two sound sources, modified from [54]

But in real world, computers are not (yet) performing as good as the human brain, struggling to separate various sound sources by only two microphone devices. Not to mention, that most of the recent applications only have one microphone, such as e.g., smartphones or verbal interfaces of modern entertainment systems which bases on automatic speech recognition (ASR) and thereby uses advanced noise filters and separation algorithms. Recent research [55, 56, 57] still deals with the problematic of an appropriated way to use cocktail party algorithms for sound separation. As multi-source sound propagation works as well in other media such as fluids and solid body, the effort of pure sound applications such as editing, music information retrieval and stereo rendering, gets overtaken by signal processing, mathematical, neural networks, and machine learning applications in countless technical processes.

4.1.2 Target Challenges and Basic Algorithm Notation

Yet these processes are far from perfect but enable a variety of uncommon approaches such as solid born sound investigation which is inhabited in the field of structural acoustics of solid bodies [53] [58]. To get back to Chapter 2.5, these sound waves propagate through a structure, like a sound wave propagation through the air, with a specific speed of sound depending on the material [58]. Having the finite wave propagation speed of structural waves in mind, the idea of a runtime difference of finite defined measurement spots along the structure or medium comes into one's mind (see Chapter 2.5). Human ears have a finite distance between each other, same as the points of sound emission and reverberation objects along the traveled sound propagation path. In Figure 33 these properties are visualized and transformed on a set of microphones. Differing the times of the individual energetic impact of the sound wave on the ear drum, the human brain performs a so-called cross correlation process. Which has the mathematical description of the following Equation 24 [58]. $X(t_1)$ is the first time depending signal source in the system, $Y(t_2)$ is the second source with its TD wave propagation. Imaginable, that additional sources of sound, or noise signals will increase the complexity of the mathematical expression.

$$R_{xy}(t_{11}, t_2) = E\{X(t_1) \cdot Y(t_2)\} \qquad \text{Equation 24}$$

Cocktail party algorithms mainly depend on this equation, as runtime differences define the delimitation of the individual source signal and combined the individual signals on their determined signal shares on a single axis [58]. This specific audio separation aims to provide machine listeners, with the help of microphones that are in fact vibration sensors, the ability to extract signals or sources from a given sound or vibrational mix. This mix can be recorded at a relevant position in the system, e.g., in case of a human ear at the position of the listener, or in case of a machine diagnosis of a damaged bearing close to the position of damage. Least is the desired outcome of this thesis. To get an idea about the process, the author tries to find a possibility to apply an acoustic algorithm structure to a mechanical problem? Beforementioned algorithm is defined as a blind source separation (BSS) algorithm. Hence this algorithm can separate the mix of vibrations, recorded on a defined position (see central signal of Figure 43), and splits it into a defined number of calculated and thereby algorithm estimated source signals [54]. This algorithm does not have the ability to measure the sources of input sound directly which is the name giving definition of a blind algorithm. By this, a validation of the calculated output signal is rather complex but, in case of a human voice estimation, comparable with the speaker's voice samples. In technical application its mostly impossible to validate without source measurements and could only be an assumption. Due to this, further options of source information shall be given to increase the applications validation capability, even though the recorded source signal is corrupted by reverberations and other interfering vibrations as defined in chapter 2.5.1. To describe the recent and the following cases correctly, the basic notation of determined mixtures are introduced by the relation due to numbers of source J and the number of sensors I. To define each possible setting of the source-/sensor setting the algorithm can be fed with optional information's via additional sensors. So, there are there are three main cases of the measurement or input setting:

- Determined Case — Equal Source and Sensors — $J = I$
- Underdetermined Case — More Sources than Sensors — $J > I$
- Overdetermined Case — More Sensors than Sources — $J < I$

Furthermore, there is the quantity of defined source that is named as:

- Single- Channel Case — $I = 1$
- Multi-Channel Case — $I > 1$

While the target mixing position or, in case of the test rig, the mixed signal sensor environment has a further definition of the interfering surrounding conditions named:

- Instantaneous
- Anechoic
- Reverberant

First of the mentioned is an ideal mix of both sources with no time delay. Means, it is a mix of both source signals without any interference, simply describable as a superposition of both synchronous signals. In technical applications this case appears close to never. Anechoic describes a direct recording environment with time delay between source and sensor, but neglects reflections of the soundwaves on surrounding mater. In acoustic this could be an open air, or studio performance, in technical application more a highly damped and isolated environment, even though this case still not ideally exists in real world, as even damper and isolators reflect a tiny bit of energy back into the initial source system [58]. But let us keep this option with low interference in mind for further discussions. The main task will take place in the last of the three, and most complex, settings. Reverberant conditions are the conditions that must be expected in the acoustical systems, specially of low damping isotropic properties of steel structures as test rigs (see Figure 43) and wind turbine systems [58].

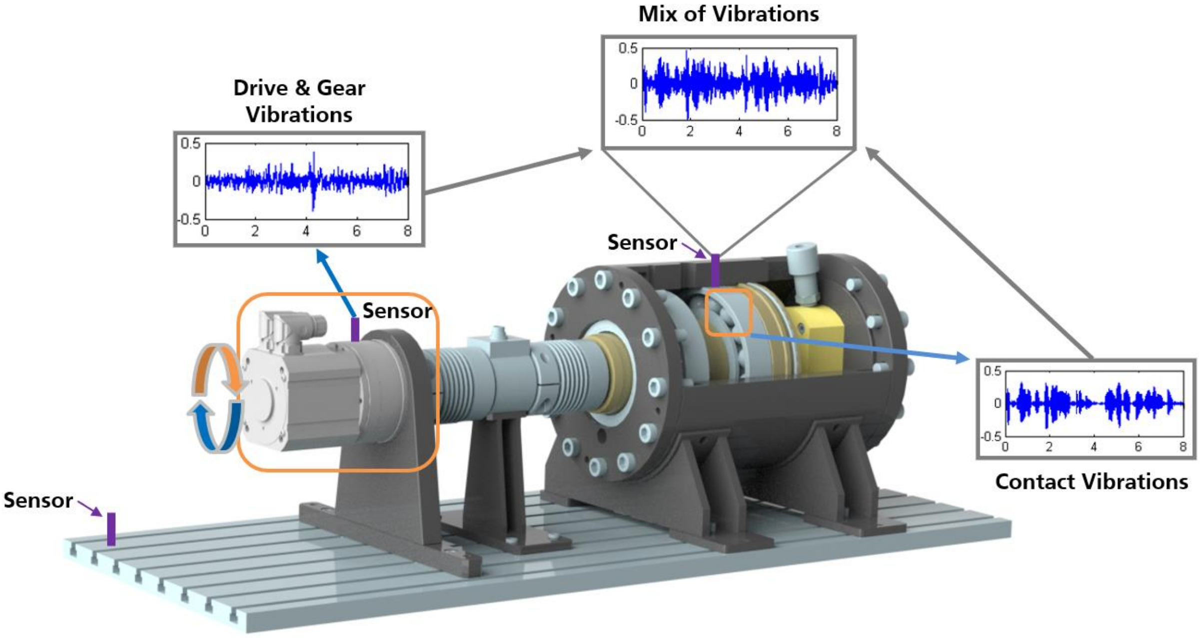

Figure 34: Test environment of sensor equipped BEAT0.2 [21]

Having the annotations of multi or single channel cases in mind, Figure 34 gives a first idea of the simplified test environment which has been selected earlier in Chapter 3. Simplified, because of the lack of external noise sources, which might be introduced through the machine basement, such as surrounding vibration emitting machinery (e.g., BEAT6.1 hydraulic pumps, cooling fans or trucks on the near highway). These influences won't find place in this examination and description of the test environment, as all surrounding machinery of the LBL is turned off before starting the later described test programs and measurement campaigns in chapter 6, assuming a noise free setting due to low noise amplitudes measured in at a reference test in standstill of the BEAT0.1 test rig. Anyway, Figure 34 gives a defined view of a basic introduction of the planed sensor equipment of the test rig. There are three vibrations signals visualized in the TD of the main positions of interest.

- Drive and Gear Vibrations — Noise signal of the drive system
- Contact Vibrations — Desired measurement result of the contact area
- Mix of Vibration — Measured vibration on the housing surface

So, in the case of Figure 34, there are two sources of vibrations $J = 2$, Drive noise and contact vibrations. These sources are displayed on the left side of the following process chain in Figure 35Figure 35. As described earlier, the idea is to extract the contact vibrations inside the bearings contact zone. The bearing is mounted inside a bearing housing, with no option of internal measurement (which would be more beneficial), hence the only possible measurement location is on the housing surface. This is displayed in the center of Figure 35Figure 35. Now there is the desire to keep the system in a determined or even overdetermined case of observation, as [54, 58] define these cases as beneficial for algorithm processing. Thinking of the number of needed vibrations sensors the definition the number of sensors shall be at least $I \geq 2$, hence a multi-channel case is defined. One sensor is obviously reserved for the housing spot, one is set to be the drive observer sensor, as this source is estimated to induce the highest vibrations amplitude in the system. A determined setting is achieved by that. To support the assumption of a low external sound immission over the environment, a third sensor is placed along the machine base plate. Due to the later test results, the final annotation is set to the case multi-channel case with $I = 3$ and J$= 2$, as a third noise source can be neglected. (Note that this definition of the possible cocktail party annotation only suits for this basic BEAT0.1 test rig).

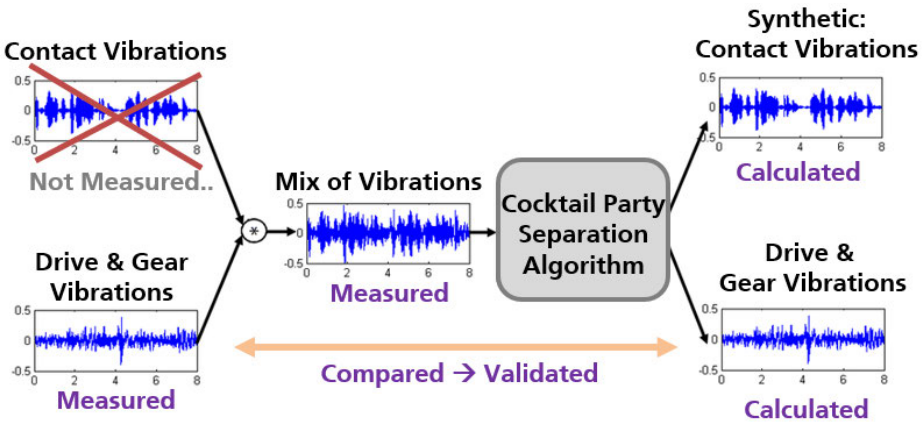

Figure 35: Basic scheme of the separation process, modified of [54]

4.2 Selection of a Separation Algorithm

The evaluation of the findings along with the process of algorithm capabilities quickly boil down to less than a hand full of options. To acknowledge the options of a variety of predefined algorithms instead of programming a solution by itself, the author takes account of the statement of Andrew NG in his *Coursera* lecture about machine learning algorithms for audio source separation in forms of a single value decomposition (SVD) algorithm. He defines this option audio processing with a double input SVD algorithm, performable by very short lines of code, but also admits that this short statement takes researcher a very long time to develop it [59]. Same is for the complexity of the example on the deep learning platform at the *MathWorks* website, showing an example of binary and soft mask training algorithms of a single mixed input signal and output evaluation options [60]. Summarized, a limited overview of possible algorithms are named in [54] [59] [60] [61] [62], but leave no doubt, that each code approach is specifically tailored on a certain application environment which basically defines by the beforementioned determination cases of chapter 4.1.2 and the processing structure. Most of the ideas base on single inputs with a mix of speech samples, processed individually to a state where the separated input signals get compared to voice samples of the input speakers or instruments in time or FD (via FFT or STFT) signals. Another factor of the selection of a suitable algorithm shall be given by the amount of computing power for signal analysis. In case of the binary mask example on *MathWorks*, processing 20 seconds of a mixed voice sample takes 90 minutes of processing time (based on an *Intel* i7-9850H CPU with 2.60GHz and 16 Gb of DDR3 RAM). For a first impression this defines a massive effort considering the thought use as real time signal processing application on a test rig or wind turbine. Second, the structure of the used processing method is attempted to be rather simple in terms of programming, as the complexity of base problem, remembering that the aim of this thesis, is the transfer of a speech recognition approach to machine dynamic properties, is already extremely complex. Due to the prior definition of a multi-channel case with $I = 3$ and J$= 2$, and its unique ability to feed two signals into the algorithm, as well as the direct dependency of the input sensor position and wave speed parameterization option qualifies the SVD algorithm approach for further explanation and investigations of the noise signals of the test rig. Therefore a brief introduction of the algorithm structure is given.

4.2.1 SVD Definition

The SVD is a technique that can derive important parameters of a given signal and is widely applied in the field of inverse matrix problems. Singular value decomposition performs a factorization of real or complex matrix systems in a linear algebraic environment. The similarity to the main task of this thesis, is the SVD assumption that noise in the speech or vibrational signal is uncorrelated and additive to the original or pure signal. Using the SVD technique might enhance the noisy signal with the retention of singular values of the overdetermined and over extended data matrix decomposition. The noisy part of the signal is supposed to be associated with these singular values and are deleted via spectral signal comparison for each sample period. One field of signal analysis is the eigenvector correspondence to the largest singular value containment of signal information, while smallest eigenvectors point out the definition of noise. This helped enhancing the reconstructed signal by use of this largest eigenvector [63]. The basic annotation of a SVD processor can be described by the following Equation 25 of the short time Fourier transformation (STFT) which is then stitched together by the *repmat* function of Equation 26 to build a spectrogram .

$$S_{(\omega,t)} = U_{(w,t)} \cdot E_{(\omega,t)} \cdot {V_{(w,t)}}^{T} \qquad \text{Equation 25}$$

Proposing a speech signal to be $S_{(\omega,t)}$ any singular matrix, which specifically defines the spectrogram of the given signal speech signal $s_{(t)}$. ${V_{(w,t)}}^T$is a conjugated unitary transposed matrix of $k \times N$ dimension, and $E_{(t)}$ is a $k \times k$ unitary matrix [64] .

4.2.2 Preselection and Application of a SVD Example

Now the adaption of this algorithm on a speech related problem is defined by a single line of code, which contains the ability to perform the beforementioned tasks of speech separation due to runtime differences of the input signals via spectrogram decomposition. This is given by Andrew Ng as a code, which need quick explanation of the environment assumption in advance. The algorithm bases on runtime difference inspection and is used to demonstrate microphone separation distance sensitivity. Transferred to the problem of the test rigs vibrational measurement, this system also uses two microphones for two sound sources. The analogue is given by two spatially separated tone generators, centered inside a circle with two microphones. In this thesis the sound sources are the drive vibrations and the contact vibrations that have a structural connection (shaft, supports, couplings) between each other. In Ng's example, this connection is the option to transmit vibrations through the air. As described in the previous Chapter 2.5.1 the wave speed and form differ from air to a solid multibody system. But having the idea of runtime differences, as source recognition parameter, seems a promising option to the author. So let us have a closer look to the code itself, as adaptation to a solid body environment rely on the parameters given in the example on [65]. The basic structure of the performed octave simulation on *Matlab* are two spatially separated tone generators, with two microphones, centered around them in a specific distance called d_{Mic} and d_{Src} similar to the set up in Figure 38. These tones are generated sine waves with an amplitude of one. Note that the examined cocktail-party algorithms need an normalized input data amplitude to create a comparable computation base, this circumstance gets picked up in the definition of the signal input within chapter 7 [59] [60] [61]. The frequency of the first tone generator is 1100 Hz and differs from the second one with 2900 Hz. The distance between the microphone and the center of the setup up is set to 1 meter and the sources are centered with a radius of ten meters. The speed of sound in this case of an air transmission scenario is 340.29 m/s. The inputs of the SVD function, Mic_1 and Mic_2, now are mixed signals, containing tone one and two and can be calculated through the inverse square attenuation of the amplitude intensity, regard to the transversal sound propagation in the air. So the inputs get a direct parametrization of the runtime difference through their geometrical position of a spherical environment. Storing the mixed microphone signals in the TD is realized through a column vector called *x*. To process these arrays, a SVD function is defined in terms of a *Matlab* syntax given in the following Equation 26 and then related to Equation 25 through an elementwise correlation, as the structure of this relatively simple line of code contains relevant information. First in Equation 26 the *svd* function is called in *Matlab,* bracketing a *repmat* array repeater that returns values to the *svd* and thereby builds a *svd* input array with the size of the array length of the input array *x*. By this the double column matrices *W,s,v* are filled with output data and defined in a later paragraph. The *x* array is, due to the *repmat* function, physically corelated to a power spectrum with input of a TD channel or microphone signal $x_{(t)}$. So the input for the *svd* function is defined with the first matrix $U_{(w,t)}$ in Equation 25, marked red in Equation 26. The green marked multiplicator in the code represents $E_{(\omega,t)}$ in Equation 25, while the light blue transposed x' value is ${V_{(w,t)}}^T$.

$$[W, s, v] \ = svd((repmat(sum(x.*x, 1), size(x, 1),1).x) * x') \qquad \text{Equation 26}$$

Due to limited information in the lecture of Prof. Ng, the only reference is related work of scientists like Te-Won-Lee, Sam Roweis and Yair Weiss, but without explicit definition of the papers leaving the deeper structure of the code partly unclear [59]. Getting back to the output of the code example, a definition of the output arrays is given by [66]. The explanation of the diagonal value *s* is given as the magnitude of differing spectrum components. *W* and *v* are rows and columns in orthogonal vectors or *Matlab* arrays that can be used to map the frequency component in respect to the corresponding magnitude to *x* in space. So the focused output array of the code is the first and second row of *v* [59]. From here a little plot series of a very short signal duration of 5 milli seconds will help the basic idea of the author to use the code and further analysis via FFT which is not part of the provided example on *Coursera*. First a comparing plot of the input and the output signals of the SVD function of the standard configuration in TD is displayed in Figure 42. Without surprise, similarities in the signal are not directly distinguishable.

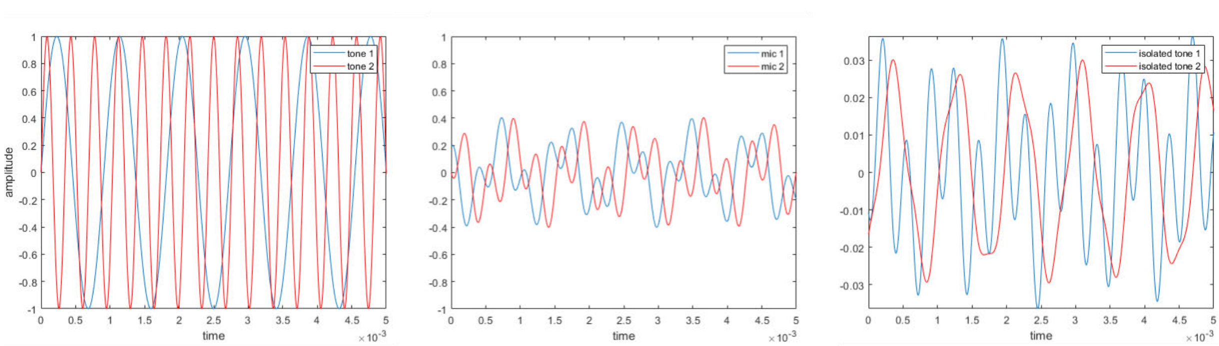

Figure 36: Plot of tone generator, mic and mixed signal SVD input in TD

So the information inhabited in the tone generator and microphone signals are now compared with the output signals of the array *v* of the *svd* function in FD(see Figure 37). As described in the course [59], the accuracy is astonishing. The SVD function manages to separate the mixed mic signals efficiently, as the amplitudes of the isolated tone signal, compared to the mic signals in Figure 37, get properly assigned to their original frequency of the tone generator. The elapsed time, measured via *tic toc* function in *Matlab* for the pure *svd* process is measured with 7.385 seconds. The amplitude of the output signal is about seventy-two times smaller than the input signal and does not allow a direct compare. But, nevertheless in terms of frequency accuracy of the split signal, the result is promising for the application in a machine dynamical problem. Note that, a direct distinction of the output related row number of *v* to the input number is not possible, as the algorithm reacts on the signal properties instead of the defined input signal number. In this case, the output signal *SVD Output 2* correlates to the tone generator signal. To get a quantification of the reduction ratio, which is comparable to the algorithm's separation efficiency of the SVD output signal, see the SVD Output 1 and 2 plot in Figure 39. Here the outputs show a clear amplitude reduction, towards the tone generator signal of the actual input. As the SVD function normalizes amplitudes in the profile, a relative value appears as more convenient. Considering the input of tone 1 as 100% input value, the frequency wise correlating *mic 1* amplitude with 24.323 is mixed with a power part of 16.397 of *mic 2.* So the relative component of *mic 2* at 1100 Hz is 67%. Same relative quantification calculated for the *tone 2* frequency of *mic 1* in *mic 2* at 2900 Hz. Note that the deviation from the given *tone 1 & 2* input frequencies and the actual displayed frequency of 1104 and 2888 Hz in Figure 37 stems from the sampling frequency calculation of the FFT function and is neglectable. Looking at the *SVD output 1& 2,* at the 1100 Hz frequency range, a reduction to around 32% is achieved, which is nearly half of the mix signals amplitude power within the signal's length of 5 ms. At 2900 Hz of *tone 2* the reduction is around 96%.

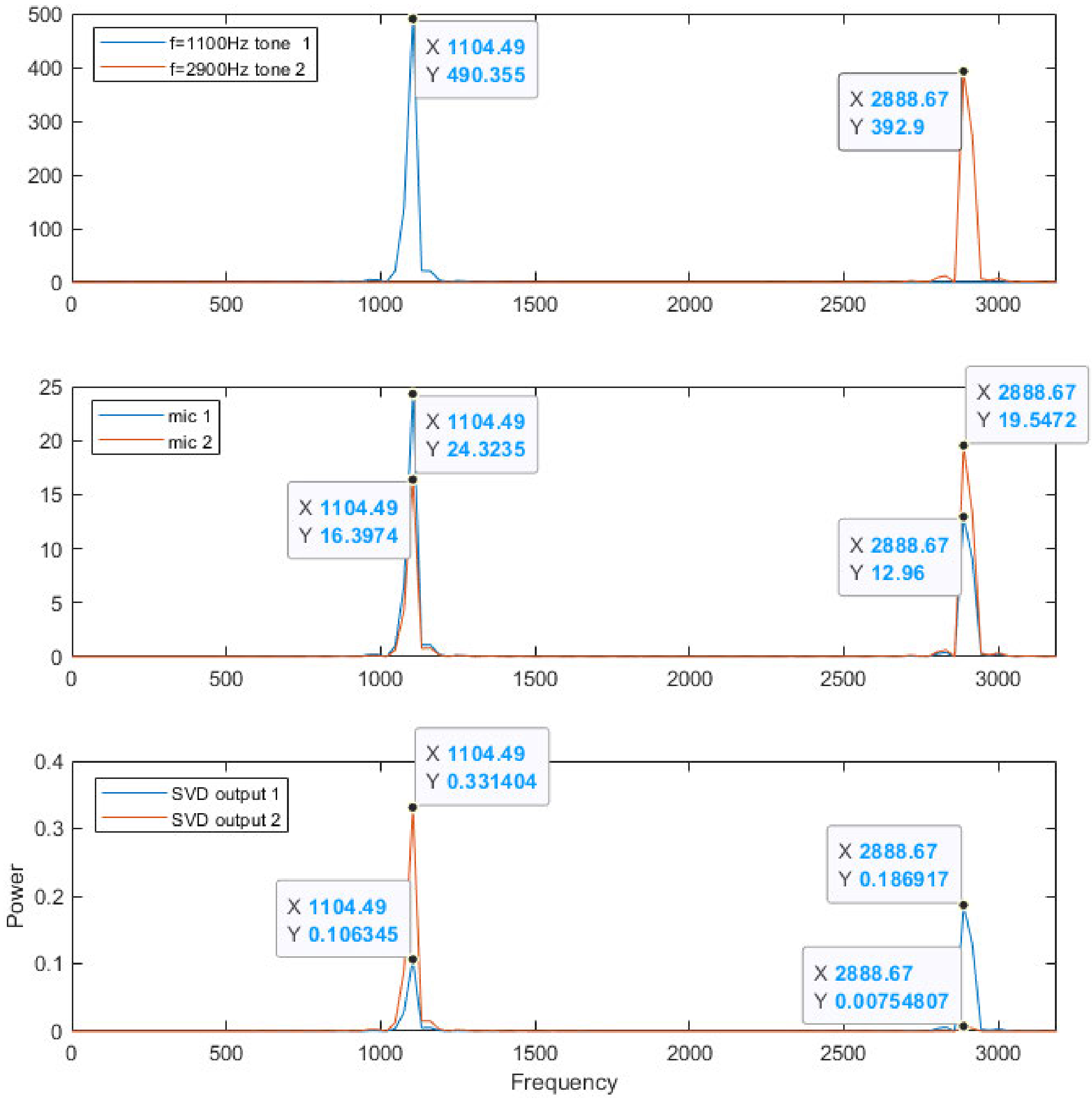

Figure 37: FFT analysis of SVD input and output in an air transmission environment

From the first impression, at the first milestones of the thesis research phase, this algorithm suits well for the planned implementation in the vibrational data examination process. So the development of the measurement chain, application of the sensors and selection and development of the test environment and test profiles were forced. Also the data pre- processing and CM based inspection of the relevant test data is done and leaves the SVD implementation as last step before all relevant tasks of this thesis can be ticked off. Unfortunately, the results of this last step, the SVD based signal processing in chapter 7.2, shows poor performance and did not satisfy in terms of signal assignment and separation. The adaption of the code in terms of the solid born sound speed as well as the geometrical adaption of the sensor distances were missed out in the beginning but performed after the later described results of the data processing with traditional CM approaches and SVD approach in chapter 6.

4.2.3 Parameter Adaption of the Selected SVD Example

To double check the ability of the code, a performance evaluation under a test rig related geometry state is performed. Therefor the speed of sound and the expected distance of source and microphones are adapted. These values are subtracted of the wave propagation behavior of chapter 2.5.1 and the following selection of the sensor type in chapter 5.1. So the assumption is the propagation of longitudinal waves, measured with a suitable vibration sensor set. So the extraction of the expected, and nearly frequency stable wave speed of 5918 m/s for SAE AISI 4340 steel type due to the housing, bearing and shaft steel mix properties. The centers distance of the sources (bearing contact zone diameter) marked in magenta in Figure 39 define on a diameter of 0.4 meter. Due to the small sensor/ source distance a value of 0.42 meter is set.

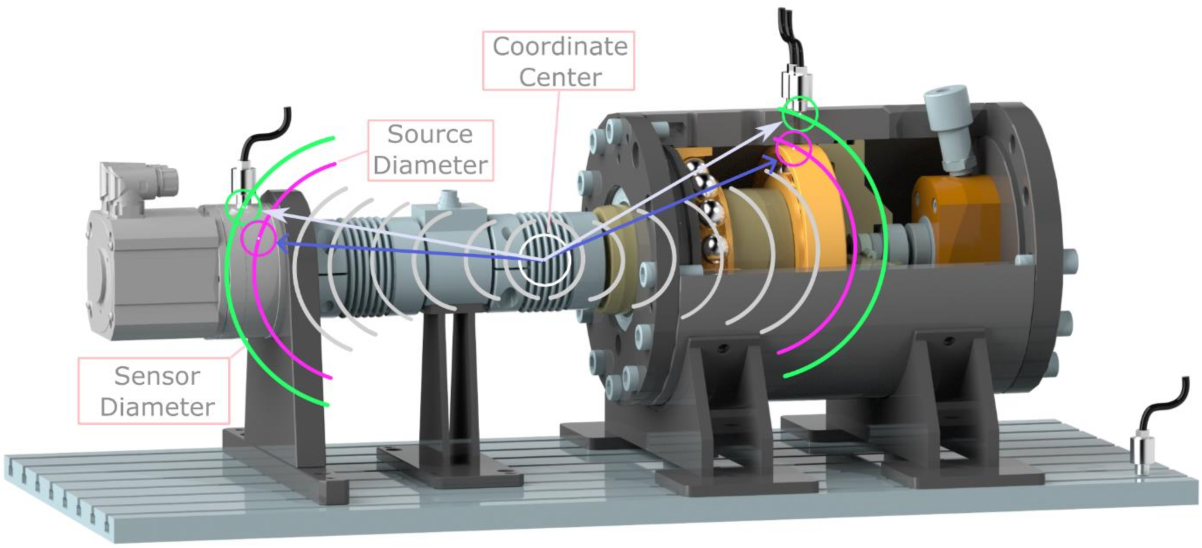

Figure 38: Test rig geometries in relation to the source and sensor diameter [21]

First the adaption of the speed of sound is made with the standard geometrical distances of the *Coursera* example, and give a very promising picture of the expectable frequency effects in Figure 39, defining the very same output frequency of the SVD function like in Figure 37. Only the power of the amplitude varies in the *SVD Output 2* and might be a result of the same sampling frequency at the high transmission speed and smaller distance between source and mic. One mind would assume the TD signals with congruence to Figure 36, which is correct and makes another data plot obsolete. Note that the FFT plot of the tone generator input is not displayed in the upcoming figures, as it stays the same. Now the adaption of the test rig's geometry, displayed in Figure 38, is added to the property of high-speed solid born sound. The elapsed time for the *svd* process is measured with 8.667 seconds. To get a quantification of the reduction ratio, which is comparable to the algorithm's separation efficiency, of the SVD output signal see the SVD Output 1 and 2 plot in Figure 39. Considering the input of *tone 1* again as 100% input value, the frequency wise correlating *mic 1* amplitude with 24.38 is mixed with a power part of 16.16 of *mic 2.* So the relative component of *mic 2* at 1100 Hz is again 67%. Same relative quantification is also calculated for the *tone 2* frequency of *mic 1* in *mic 2* at 2900 Hz, matching the idea of sound speed independency. Taking a look at the *SVD output 1& 2,* at the 1100 Hz frequency range, a reduction to around 24% is achieved, which is a higher win on separation performance than displayed and discussed in the air environment of Figure 37. At 2900 Hz of *tone 2* the reduction is around 98%. So the process efficiency seems promising, but also could be affected by loss of information due to the high-speed parameter of sound, compared to the lower sampling frequency of the algorithm.

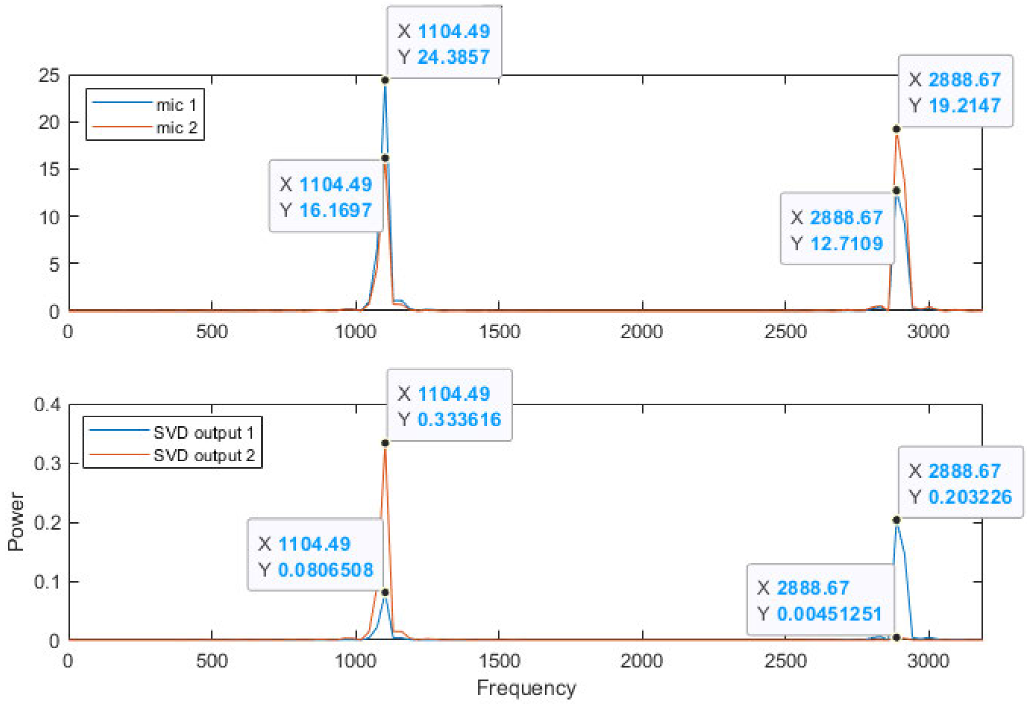

Figure 39: FFT analysis of SVD input and output in a steel transmission environment

Having the knowledge about the result independency from the speed parameter, this prevents another plot with air speed and test rig geometry at this point. Now the TD signals add some information value to the discussion, so there is a plot series in Figure 40 with the tone generator signal (same to tone 1 and 2 in Figure 36) excluded. Having the diameter of the source and mic (sensor) reduced from 10 and 1 meter, and a swopped source/ sensor position, the recorded sound amplitude of the microphone is increased with a factor of 250.

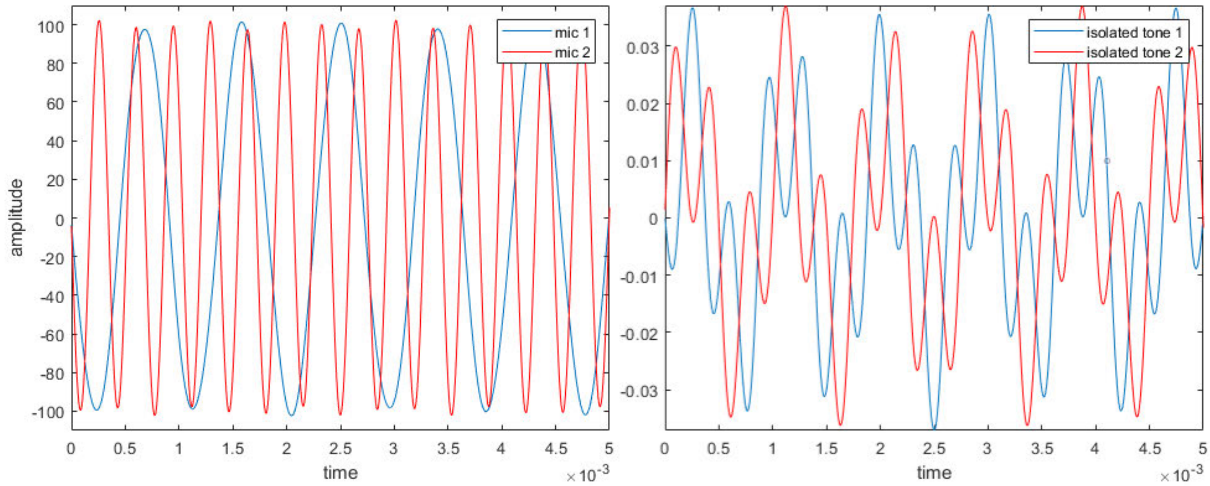

Figure 40: Mixed mic signal and isolated SVD output in full test rig parameter setting

Through the definition of a transversal wave mix function for the mic, this appears as correct. Also the SVD functions is defined as a spectrogram differentiator with normalized inputs, leaving the effect of amplitude neglectable compared to the frequency content [59] [66]. The elapsed time for the *svd* process is measured with 7.042 seconds. Significant findings are, the reshaped mix signal, that differs highly from the mic signal of the air related measurement, as well as the isolated tone which appears like a clone of the mic signal in Figure 36. But again, the FD is defining the actual result in Figure 41. To explain the findings, a quick look at Figure 43 suffice.

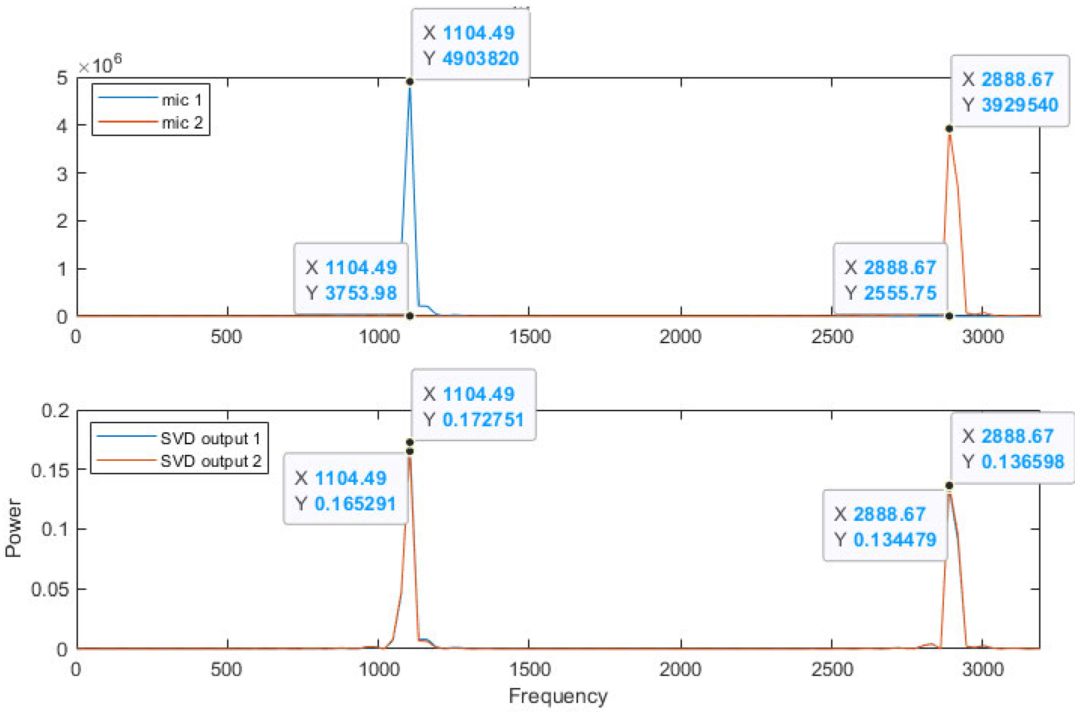

Figure 41: FFT analysis of SVD input and output in full test rig parameter setting

Considering the input of *tone 1* again as 100% input value, the frequency wise correlating *mic 1* amplitude with 4903,820 is mixed with a power part of 3,753 of *mic 2.* So the relative component of *mic 2* at 1100 Hz is 0,04%. Similar relative quantification is also calculated for the *tone 2* frequency of *mic 1* in *mic 2* at 2900 Hz with 0,06%. Taking a look at the *SVD output 1& 2,* at the 1100 Hz frequency range, a reduction to around 4,6% is achieved, which is a higher win on separation performance than displayed and discussed in the air environment of Figure 37. At 2900 Hz of *tone 2* the reduction is around 1,7%. Having these results in mind, the performance is very low. As mentioned in the first sentences of this Chapter, these results were calculated after the SVD algorithm got fed with the sensor data of the test programs in Chapter 7 and contribute to the findings along with this later described performance.

5 Development of a Measurement Chain

One of the most crucial tasks in a bearing damage diagnosis is finding an appropriated measuring chain. This chapter will focus on basic measurement system properties, respecting the physical properties of the test environment and the computing power of the DAQ system as partly defined in Chapter 1 and Chapter 2. As sensor systems for rolling bodies with low rotational speeds are not part of traditional ISO or VDI standards, the selection needs a profound physical description like linearity of frequency ranges and appropriated sensitivity values. On this purpose, an expert team of the CM branch at *Bachmann* Electronics supported the selection process [67]. Before further discussing the measuring value, and final sensor selection a mathematical definition of the signal transformation takes place in the following chapter 5.1.

5.1 Selection of Sensor Type

The main objective of the measuring section is to transfer a time depending, continues physical input signal ($u_{(t)}$) into a storable output value ($y_{(t)}$). Besides the input value ($u_{(t)}$), the input ($z_{(t)}$) represents various noise sources, transduced into the state space function block ($z_{(x,u,z,t)}$) of Figure 42. The approach of detecting, more explicitly said, distinguishing these specific error signals or noise sources takes a major position in this thesis [68].

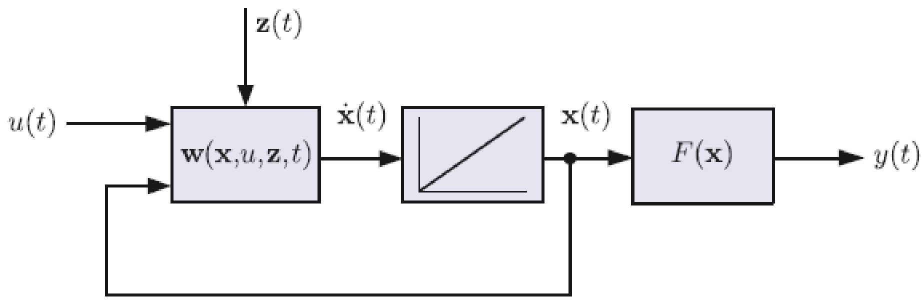

Figure 42: State space measuring section

Equation 27

$$\dot{x}_{(t)} = \frac{dx_{(t)}}{dt} = w(x_{(t)}, u_{(t)}, z_{(t)}, t)$$

Equation 28

$$y_{(t)} = F_{(x)}$$

This model graphically represents the input vector equation of state $x_{(t)}$ which gives information about the input values and their derivatives (see Equation 27). This equation represents the definition of the output signal. In technical systems, these states values are defined, as long the initial value of $x_{(t0)}$ and its course over the time interval of $[t_0, t]$ is known. Beyond theory, real measurement sections will always be affected by internal errors which can cause signal deviation in terms of linearity failures and such. But for now, the input value ($u_{(t)}$) and noise sources ($z_{(t)}$) need further definition and will be focused on the following chapter [68].

5.1.1 Demand and Physical Sensor Capability

Thinking about the appropriated sensor system, one mind could come up with the impression that machines, whether there deemed “healthy” or on their last leg, contribute vibrations. Like mentioned in previous CM chapter 2.6.1, this is true. Having the exact knowledge about the expected vibration frequency ranges defines the physical demand of the sensor itself [6] [68]. Clearly a sensor consists of a variety of electrical and mechanical components with a physically limiting finite electrical resistance or excited mass that transforms physical inputs into an electrical signal. But before this chapter ends up in a vast explanation approach for all kinds of vibration sensors, lets define these first limitations and see how sensor types yet fall out of scope. The most relevant characteristic of a vibration sensor is its frequency response, shown by a qualitative example in Figure 43. The abscissa shows a frequency range in Hertz and starts with a lower edge frequency and an upper edge frequency value. The axis of ordinates defines a deviation of the nominal output in dB or in percentage (%).

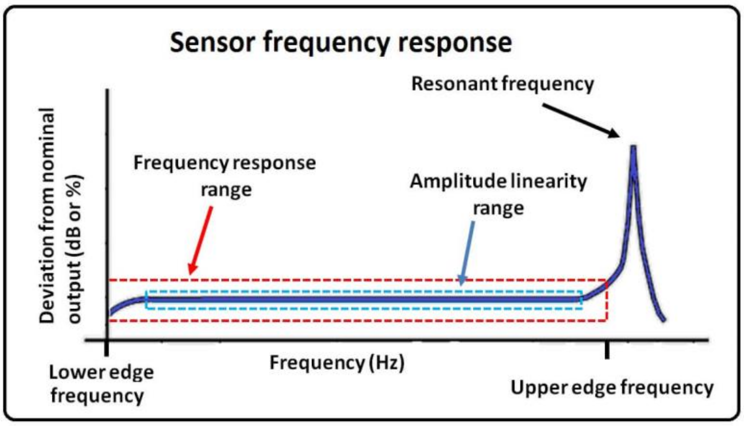

Figure 43: Sensor limits and specifications [6]

The red area in Figure 43 defines the frequency response range where the nominal output deviation is limited to a value of ±3dB. Hence these values can still be interpreted within the range but lack on accuracy. Waters takes the linearity range of a sensor set into special account, as these nominal output values provide a solid base to quantify the physical input with a high accuracy. In general frequency response applications, the widest range of frequency, with the lowest lower edge frequency and tightest tolerance shall be considered. When benchmarking a sensor set against another, the sensitivity of a sensor set is described as another significant property. Here a distinction comes by between high and low frequency applications as well as the maximum capacities, measured in the gravitational constant g [6], [69]. The question for a suitable sensor types now relies on a single value, with a limitation by the maximum measurement range for the amplitude. Rewarding the previous examination of the most relevant frequency in Table 3, which is defined by the lowest appearing ball pass frequency of the roller defect frequency f_R within the boundary of the $\dot{\rho}_{7220} = 100 \frac{deg}{s}$ test set up at$f_R = 1{,}499\,Hz$. (Note that the reference test $\dot{\rho}_{7220\_ref} = 10 \frac{deg}{s}$ is not relevant for the further examination and is only recalled as a reference speed along with later test distinction of chapter 66.

5.1.2 Quick Selection of the Sensor Type

Considering the preselection of suitable sensor type, two types go along with most vibration measurement approaches. First is the micro electro- mechanical system (MEMS) second is the integrated electronics piezo electric (IEPE). First of these is widely applied in smartphones, mobility and drone systems and very low frequency structural health monitoring (SHM) systems in wind turbines, second takes a major lead in precise CM of wind turbine with higher frequency drive train vibrations [70]. As knowledge of the lowest expected frequency along with the measurement approach is defined in the last chapter, lower edge frequencies do not demand for the typical MEMS applications of frequency responses of $\ll 0{,}5\,Hz$. Second, the high background noise levels of the MEMS do disturb the analysis and possible separation approaches of the next chapters. Third, the large temperature drift of MEMS would not fit the precise measurement environment along a test rig or rotor blade [69]. Last to mentioned is the massive development of high accuracy LF IEPE systems, with a suitable range and cost reduction over the last decade [6] [70]. Hence, MEMS fall out of scope, leaving the IEPE sensor to further description.

5.1.3 IEPE Sensor Structure

The function of a IEPE sensor is described by the piezo electric phenomenon. A seismic mass is accelerated by an external force and transmits force to a PE- crystal element. The output voltage of the crystal structure is proportional to the induced force. In the early 60s *PCB*© electronics patented the ICP© sensor build (see Figure 44), which still dominates the market of single axis IEPE accelerometers. (Note that three axis accelerometers are not part of this thesis, due to the defined vibration properties of chapter 2.5.1). The *ICP*© design of an exemplary delta sheer type sensor is basically described in Figure 44 and thus not need further explanation, as the direction of acceleration is also given with the small vertical arrow on the right side. *ICP*© sensors comply with two wire connections, as the static sensor signal and the dynamically amplified output signal is connected to one wire [42].

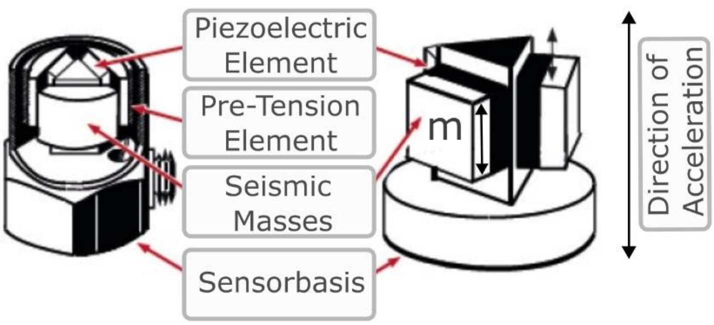

Figure 44: IEPE sensor with ICP© delta sheer type configuration, modified of [42]

5.1.4 Expert Talk and Final Selection

Nicholas Waters, north American key account manager of *Bachmann* electronics, speaks in [6] about the application scenarios and limitation of low and high frequency sensors in wind turbines. He recommends *Bachmann*'s BAM500 LF sensors with 500mV/g sensitivity, for slow rotating machinery (e.g. main bearing) and the BAM100 as HF sensors with 100 mV/g for more dynamic monitoring tasks (helical stage and generator). These declarations fit to the planed test environment of Figure 34 with LF contact vibration along the housing and HF drive noise. He quotes that HF sensors would give a bigger picture of the systems overview but struggle to detect low energy contents through LF rotating machinery parts. After this highly informative article, the author took a closer look on LF sensor system on the market and compared their physical capabilities as recommended by Waters in [6]. *Bachmann's* pre-calibrated BAM500 and BAM100 series took the lead in terms of the widest frequency range and maximum amplitude measurement limits, and at the same time provides an analog voltage output [52].

Table 4: LF and HF sensor specifications of *Bachmann* series, modified [52]

	BAM100	**BAM500**
Sensitivity	100 mV/g	500 mV/g
Acceleration Range	80 g	10 g
Frequency Response ±3 dB	0.5 -14 000Hz	0.2 -14 000Hz
Resonance Frequency	30 kHz	30 kHz
Transverse Sensitivity	5% axial	5% axial

Due to a direct E-Mail request with *Bachmann Electronics*, explaining the topic of the master thesis, the key account manager for central Europe, and the product manager offered extensive conversations for general advice about sensor selection and further knowledge trade in the process. *Bachmann's* specialists agree with Waters declarations and mention the option of a parallel measurement close together to compare and verify results of the mix of vibrations signal. This comes from the possibility of HF vibrational components in the acoustic frequency range, which could be missed by the pure LF BAM500. Sensitivity in HF signal parts could come crucial when a precise bearing envelope analysis is performed. Another sensor option is given by the μBridge® sensor type. This could help detecting flexural waves and has a lower edge frequency as the BAM500 type. This option does not find use in the application process due to sufficient frequency response ranges of the BAM sensor types [67].

5.1.5 Sensor Mounting Options and Final Application

When it comes to the selection of an appropriated sensor position, two main aspects shall be considered. Due to Thomas Kuttner and his outstanding book for sensor application practice [69], the maximum contact surface between sensor and measurement object, and the expected frequency range define the mounting process. Following Figure 45 shows the frequency response of a sensor in dependency to its mounting type.

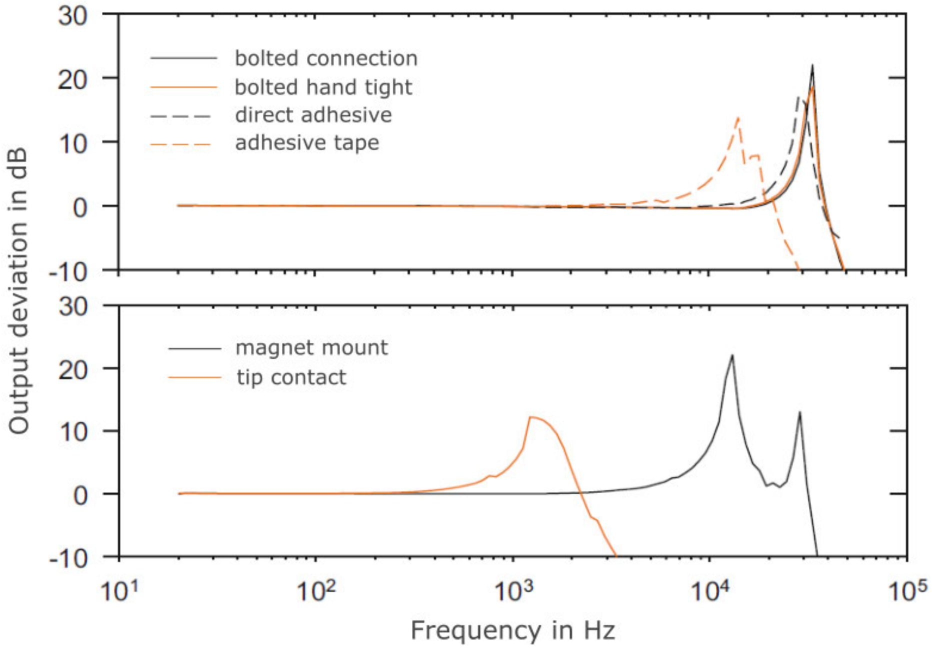

Figure 45: Frequency response ranges of common mounting options

Therefore two promising options for the sensor mount are examined. First is the option with the widest range of frequency response, the direct mount on the bearing housing via bolted connection. Second shall be the tip contact option via transducer pin. The pin option is assumed to utilize a direct measurement of the low energy pulses, decoupled from the stiff housing, directly on the bearings outer ring. As seen in previous rendered figures, Siemens NX 12 provides a suitable environment to virtually integrate the sensor option into the BEAT0.1 test rigs digital twin. Following Figure 51 shows one pin contacting directly on the bearings outer ring. This pin configuration shows a force application via a pre tensioned spring and a shoulder pin. On the right side a housing mount via M8 thread is displayed.

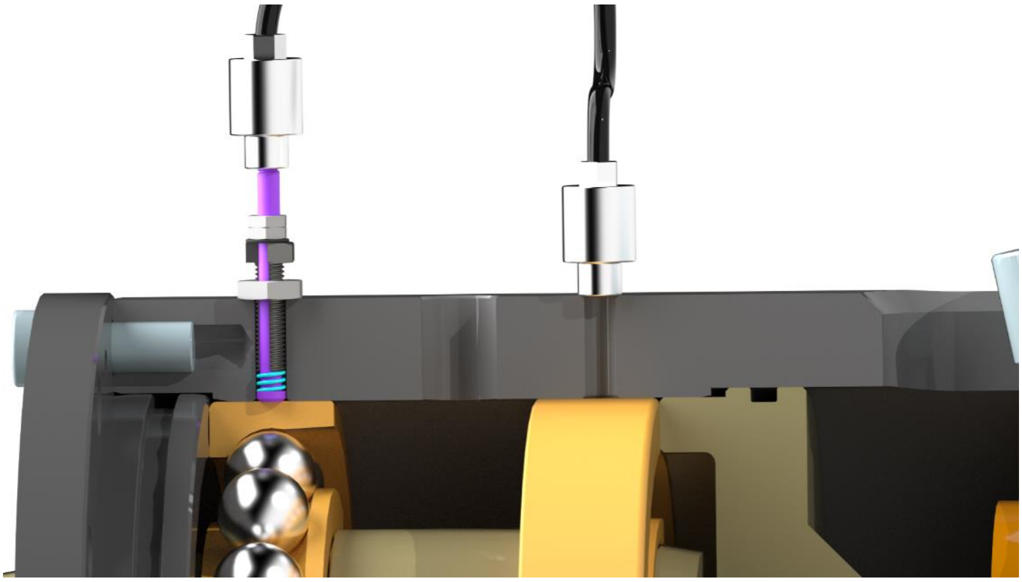

Figure 46: Transducer pin and direct mount sensor option

Even though both options in Figure 46 seem to be a possible option in terms of construction, the doubt about the general benefit of the more complex configuration is predominant. This is based on the maximum frequency response range with 1.5 kHz of the pin configuration in Figure 45, as well as additional natural or resonance frequencies of this multi- body component as described in chapter 2.5. From internal feedback for after internal presentations at the LBL, accretive doubt leads to the preclude of the pin option. So the direct mount option for the bearing housing sensors (BAM100 and BAM500) is used for the investigation of the test related vibrations. Following the assembly instruction of Kuttner [69], the sensors get connected to therefore cut M8 threads. And have shielded 4- wire connector cables attached to their threaded pin head. Also these cables are guided to the cabinet, with respect to the assembly standards of [69]. The sensor sensitivities in relation to their positions in Figure 47 are defined by the following list.

Table 5: Sensor positions and type

Number	**1**	**2**	**3**	**4**
Position	Housing	Housing	Motor support	Base Plate
Type	BAM100	BAM500	BAM100	BAM100
Sensitivity	100mV/g	500mV/g	100mV/g	100mV/g
Range	80g	10g	80g	80g

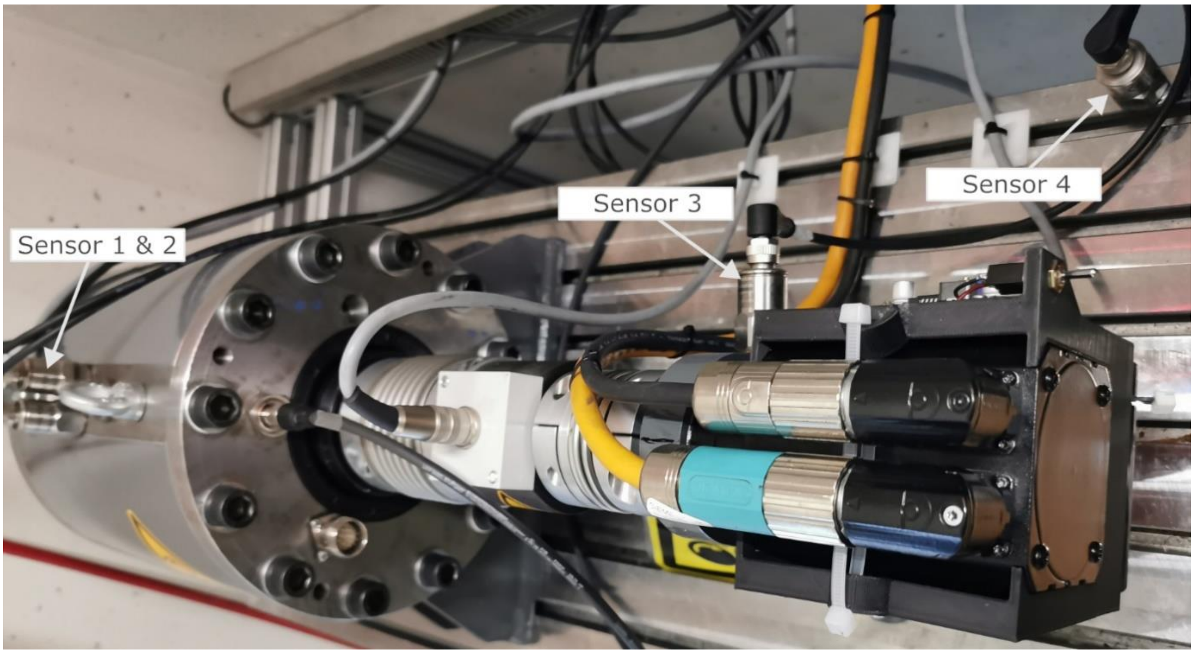

Figure 47: Final sensor set up and sensor denomination at BEAT0.1 Test Rig

5.1.6 Selection of BUS- Interface

Another processing step comes when the sensor output signal is transformed into a digital signal, which than can precisely be interpreted by a computer. This step is only necessary for analog output sensors alike the BAM series, due to their high precision and need of multiple system compatibility. To read the analog data of the vibration sensor sets sufficiently, *Beckhoff Automation* and *Gantner Instruments* provide HF IEPE conform measurement modules of the type *Gantner Q. bloxx A111* and *Beckhoff ELM6430*. Following the existing structure of measurement chains and availability at the LBL, the Gantner A111 IEPE Interface is selected and quickly defined by its features.

Table 6: Module main specifications [71]

Q. bloxx A111

Number of Input Channels	4
Input Voltage	0...10VDC
Resolution	24 bit /100kHz
Linearity	0.01% of Output
Output Protocol	EtherCat
Timestamp Protocol	Unix

5.2 DAQ of High- Frequency Data at the LBL

Sampling HF data of IEPE sensors needs a solid hardware structure to process data point accurately and fast. The option of a real time ethernet for control automation technology (EtherCat) is given by the machine control unit, in case of the BEAT0.1 a *Beckhoff C6915-0010* embedded PC. This performs with an internal *TwinCat 3 runtime (XAR)* software. The processor unit is a single core *Intel Atom E3815* with 1.46Ghz. With 2 Gigabytes of DDR3L-Ram it is mainly addressed to low frequency data processing. The digital output data of each test is transferred into an external *MySQL* data storage.

5.2.1 DAQ Structure

Figure 47 visualizes the path of data processing along with the DAQ system. Having the continuous analog sensor signal sampled with the maximum sampling frequency of the *Gantner* module (100 kHz), would increase the congruency of the physical and digital signal. Reconsidering the limits of an acoustic frequency range reduces the frequency first to 20 kHz, and then the upper edge frequency of the sensors to 14 kHz [52]. While planning the system theoretically, this seems a feasible data limitation. Specialists at the LBL developed an array sampling script to enable the data flow of these HF data with a data transfer frequency of 1ms from the module to the embedded computer. So fourteen values shall be stored in each array and then get transferred each milli second. The data format for the array sets is a comma separated value (CSV) file, transferred via *Beckhoff's* EtherCat protocol [72]. The reassembly of the test data CSV into processable and pre-defined data formats is performed via python script. This script creates hierarchical data formats (HDF5) outputs of the test data and stores them into the *MySQL* data bench. This data base is accessible from remote locations, enabling the author to remotely access the datasets. Besides the HF data sets of the sensor, LF data of the test rigs is stored in the data bench as well. This data includes drive speed, set points, torque, pressure or force values with a sampling frequency of 200 Hz. To combine or compare HF and LF in later data processing a synchronized portable operation system interface (POSIX) time stamp comes crucial and is naturally sampled with 1ns.

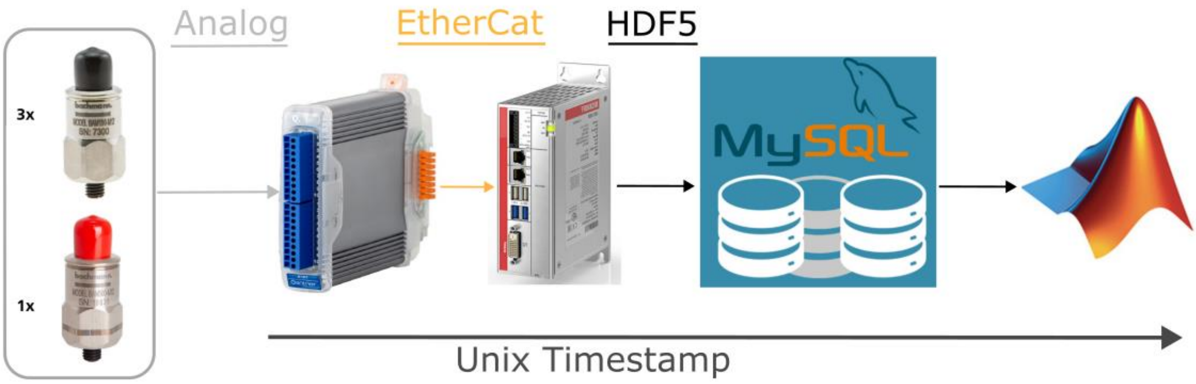

Figure 48: Data path from sensor to final processing [71] [72] [73] [74] [75]

5.2.2 Commissioning of Sensors and DAQ

Even though the BAM sensor system comes factory calibrated, the inbound into the *Gantner* module requires a parametrization due to the sensitivity and measurement range differences of the sensor types. *Gantner* provides a graphical user interface to set the IEPE measurement ranges and the sampling frequency, as well as the over sampling range and filter options. In case of the BAM sensor types, a simple multiplication of the measurement ranges (80g and 10g) with the local gravity factor (Hamburg = 9.813m/s²) suffices the range parameter. For the BAM100 and BAM500 a range of 785,04 and 98,13 defines. Due to the Nyquist-Shannon theorem [76], the low pass filter is set to half the sampling frequency. 10kHz is only half the frequency range of the acoustic bandwidth but should still produce a data set with high accuracy, as the upper edge frequency of the ideally mounted IEPE sensor (14 kHz) is not significantly higher and the expected frequency components shall be rather low.

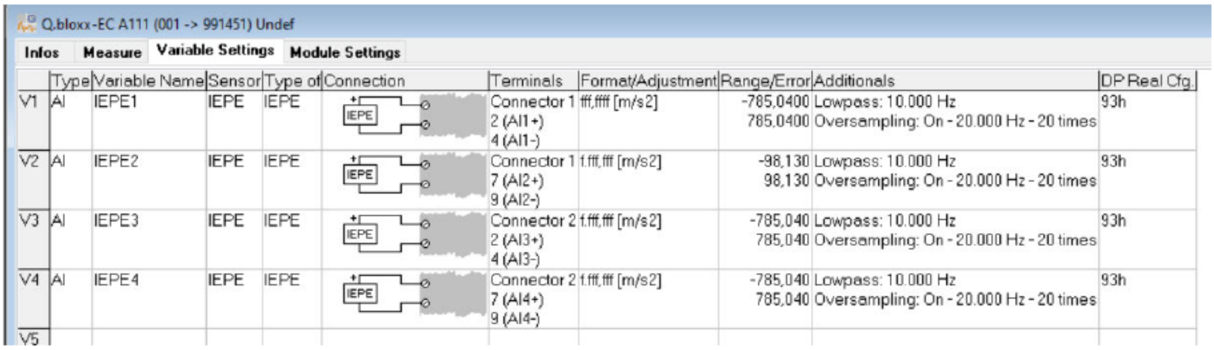

Figure 49: GUI of the *Gantner* module parameter input with inbound sensor set up

Now the setup is completed, and first visualization of the live sensor signals are displayed on the screen of the embedded computer. *Microsoft VisualStudio* in junction with *TwinCat3* enables real time data observation with limited sampling frequencies of 1kHz for a time span of 300 minutes. The sensor offset of all four sensors is zero and displays a very low noise atmosphere as all machinery at the LBL were turned off. Lifting the sensor by hand (before mounted at the test rig) will increase the displayed value and vice versa. Further tests of the calibration are not performed, due to the lack of a reference measurement system [70]. When the first test of the full DAQ system takes place, the limitation of the RAM capacity of the *Beckhoff C6915-0010* limits the feasible data rates. This finding is defined by a 50 minute exceedance test of the data rate stability at 5 kHz and 10 kHz, performed in the *TwinCat3* system and displayed in Figure 50 [77]. The outcome defines a loss of 140 exceeds, each with ten data points. By this, an overall data loss of 0,0046% is reported and acknowledged by the author.

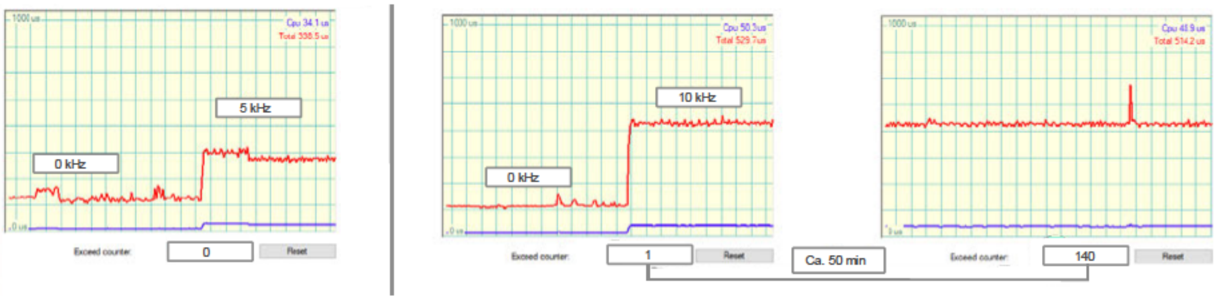

Figure 50: Exceedance counts for 5 kHz and 10 kHz sampling rate, modified of [77]

This is critical, as the maximum processible data rate drops by the Nyquist- Shannon from prior 10.000 samples to 5.000 samples per second. Due to the frequency dependency of the FFT, this limits the observable amount of HF components in the vibrational signal to 5 kHz. Massive supply chain problems at *Beckhoff* and a lack of time to reprogram the control of the BEAT0.1 stresses the plan to set up a stronger embedded PC, leaving the ongoing examination of the tests with these limitations.

6 Test Profiles and Data Examination

To provide a practical test environment, a test rig with high accuracy and load capabilities has been chosen in chapter 3. Following sensor and DAQ system selection of Chapter 5 enables to track down vibrations along the housing structure via IEPE – sensors with a range of 0.2 Hz to about 5 kHz. These two systems provide a test environment to create, distinguish and Investigate wear marks and the with it produced vibrations in a repeatable and clearly defined process [25]. The following chapter will deal with the exact reference test profile design, supporting the before mentioned qualities in the means of a scientific repeatability for validation and propose a test for real turbine damage examination. The idea of creating a repeatable, comparable, and monetarily affordable reference test is a mandatory and major step in test rig-based research processes. These test profiles provide information's of real applications in turbines and-/ or supply deep knowledge by basic analysis of damage inside a bearing system [11]. As research at the LBL is already five years in action, with a significant amount of 260 bearings yet evaluated with specific test approaches and inherit data, an already developed test profile could help evaluating the results of a test to another and additionally provide proven knowledge and conceptional thinking approaches. Besides these more complex approaches, a modal analysis-based test enables a profound understanding of the test rig's system dynamic. This test will be related to chapter 2.5 and show the eigenfrequencies of the loaded bearing system at the measurement position. Further a basic test related to wear damage and RCF of chapter 2.4.1 and 2.4.2. is performed and data sets provided. As the results of these evaluations build the base for the verification of the SVD process, it is also part of the general data examination in the machine learning domain.

6.1 Previous Wear Related Test Designs at the LBL

To gain information about the test perspective and outcome, an examination of earlier tests at the large bearing lab helps finding the most suitable reference test which provides the desired test outcome with high accuracy on repeatability of the wear characterization. Besides the chosen test environment of BEAT0.1 test rig design in chapter 3, wear marks have been examined on all test rigs of Fraunhofer's LBL in leadership of Dr. Ing. Stammler, Karsten Behnke and Arne Bartschat [11] [25]. The most dominant test topics were pointing on examination of the influence of parameters on the wear damage of oscillating bearings. From a current understanding the most relevant impacts on wear are explained in subsection 2.4.1. Test profiles now combine the defined order of load and drive motion patterns in the TD of an input signal. This is called timeseries and needs to be preset for each test and vary from test to test. This variety helps isolating the root cause of a certain damage mode and are repeated several times to clarify the specific influence of the test parameter. Figure 51 shows two examples of test profile types.

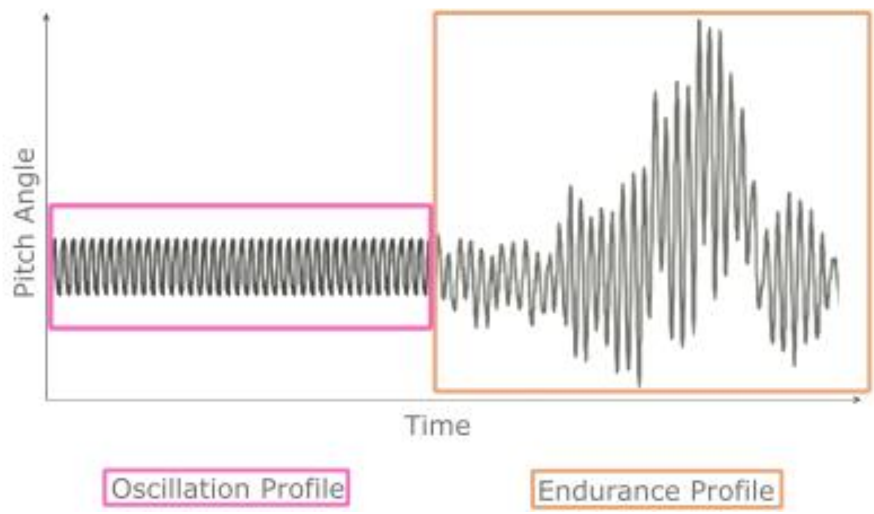

Figure 51: Basic movement patterns of test profile design

The first blue pattern represents a cyclic test with sine profiles and very small oscillation amplitudes of < 2° from peak to peak. These relate to the periodic movement of an e.g., individual pitch control movement of a wind turbine when crossing the tower shadow with no other influence or better said, power production mode under constant wind conditions. This basic patterns, in the field, are highly improbable and differ from the more likely red timeseries which shows a stochastic behavior of pitch angle adjustments of a wind turbine pitch system under fluctuating wind field conditions [11]. This red profile is further examined on projects related to hexapod test rigs and will not be part of this these. For further information about endurance test runs the author refers to Dr. Ing. Matthias Stammler doctor's thesis issued in 2019 [11]. Relying on the test protocols of the LBL, the majority of the yet made tests where cyclic test with a very basic movement pattern e.g., sine profiles or ramps. These pattern sequences are at times combined with defined breaks between each cycle and sometimes so-called redistribution runs to regrease the depleted contact area after a certain number of cycles. These redistribution runs enable a constant overrolling speed and provide a solid base for CM related vibration measurements. Additional to this, the variation of the following parameter examples and environmental test conditions help understand how wear initially begins and propagates over the time frame of a test [11] [25] [45].

Table 7: Test properties and their effects [23] [25] [28]

Test Property	Effect
x/2b ratio	Amplitude of oscillation contacted raceway surface
Load	Contact pressure definition
Frequency of oscillation	Velocity and acceleration of rolling bodies

Number of cycles	Repetitions of short oscillations increase frictional energy input
Number of redistribution runs	Amount of relubrication inside the contact area
Type of Grease	Base oil amount, additives, bleeding rate, etc.
Running in procedure	Continuous rotation to build up a tribo- layer
Temperature	Effecting e.g., oil properties

As cycle tests provide a moderate deviation of the test results and clear input parameter demands, the selection is made by the desired outcome. Therefore, a list of priorities is set up and described in the following table:

- Data of torquemeter stored for entire test
- Torque limit of drive and gear not exceeded
- Defined Velocity and acceleration
- Constant load conditions

Using the knowledge about wear development and propagation over time, the selection of a suitable reference test is performed and gives two feasible options. Besides these options another two tests are designed to create reference data. These thereby created data sets are thought to be used as basic vibration pattern evaluation and possible validation options for the SVD output. The following sub chapters will briefly define the test process and the underlaying ideas. Please find the test designs with their specific scope in Table 8. Note that's, most designs inherit a direct compare of the high and low sensitivity sensors, hence this scope is not listed. Further the load conditions of the individual tests are slightly deviating even though the axial force on the bearing sets is generally set to 90 kN with a Hertzian contact pressure of 2.5 GPa . This stems for example from temperature changes in the system, which interacts with the expansion module of the hydraulic fluid or dynamic tension losses due to frequently over rolled wear marks with a finite depth. So the influence on the transmission behavior of the vibrations wave form slightly deviates as well, leading to small changes in runtime differences at the test rig environment. Excepting Test 1, these changes cannot be accurately measured in dynamic processes of the test rig examination, leaving the static impulse test as the benchmark for runtime definition. Note that a WT has highly dynamic and directional load cases and thereby changes its vibrational transmission behavior regularly.

Table 8: Designs, DAQ IDs, properties and scope of evaluation program

#	DAQ ID	Properties	Scope
1	03010300010	Modal analysis with shock impulse measurement	Find natural frequencies, runtime differences and background noise
2	03010300015	Decoupled drive operation with low torque level	Find a pure vibration signal characteristic without bearing contact vibration interference
3	03010300013	Endurance run of wear pre-damaged RCF examination	Overrolling a severely pre-damaged bearing at continuous speed for high datapoint FFT analysis
4	03010312200	Stepped cycle test with increasing bearing damage and regreasing run	Measure the increase of vibrations at the regreasing run between the steps may quantify the minimum damage detectable

6.2 Test Profile Execution and Data Inspection

The following subsections refer to subsection 2.6.2 and show the classic CM approach for non-oscillating bearings in junction with the selected tests designs. These designs refer to Table 7 and Table 8 and the ideas of a SVD output signal evaluation and ideally validation. As mentioned in the previous SVD subsections 4.2.3 the algorithm approach in chapter 7 failed but leaving the classic CM approaches with very promising results and therefore an extensive explanation for the main part of result inspection within this thesis.

6.2.1 Test 1: Basic System Modal- Analysis

The idea of a modal analysis comes crucial when a system behavior needs to be subscribed over the full band width of frequency. As defined in subsections 2.5.2 and 2.6.2 structural analysis of these eigenfrequencies or modes indicate a vibration where maximum deformations appear while damping rates are affected by the combination of structural or multibody stiffness properties. In relation to the BEAT0.1 test rig, a multibody system includes the hydraulic cylinder, pressure plate, bearing rings, shaft, and studs. For vibrational measurement, these modes come handy to distinguish the amplification of internal or surrounding vibrations. To examine the system regarding these modes, an external impulse excitation is applied next to each sensor position. This is achieved through a shock impulse of a hardened pin, dropped about 20 mm above the surface of the vibrating structure close to the sensor's position. Besides the structure's frequency response, the runtime difference of the wave speed can be observed and the differences of the differing BAM100 and BAM500 sensor types are examined. The following *Matlab* subplot shows the impact on the bearing housing, and its propagation along the structure of the bearing housing (IEPE1 &2), base plate (IEPE4) and the sensor at the drive support (IEPE3). Figure 52 qualifies the TD signal and shows characteristic data points on data tips. The first information extracted is the duration of the impulse for the housing.

This is defined from the first excitation at $\boldsymbol{t_{start}} = 148\ ms$ and damping induced abate at $\boldsymbol{t_{end}} = 213\ ms$. The signal length of the primary impulse is 65ms. To compare the damping properties of the housing and the baseplate with connected drive support, the signal length of the ongoing vibration is defined. Here it is validated, that these two systems have lower damping properties, as they hold the vibration for the double amount compared to the bearing housing with 130ms. Note that this value is only an approximation, as the threshold for the cut off value of vibration is set to 1/30 of the peak amplitude and inherits a deviation of differing back-round noise susceptibility in both signals. The data tip on the maximum amplitude of IEPE 1 & 2 defines the signal output in relation to the sensitivity of the sensor. The difference between both sensors is considerably small and deviates with 5%. This test does not represent a high accuracy measurement as both sensors have only a suspected equally distance to the impact zone of the force inducing pin. In contradiction to this, the time of peak amplitude recognition is highly accurate and defines at 151ms for both sensors. Note here, that the impact zone is several millimeters of the sensors center pin, creating a very little runtime difference.

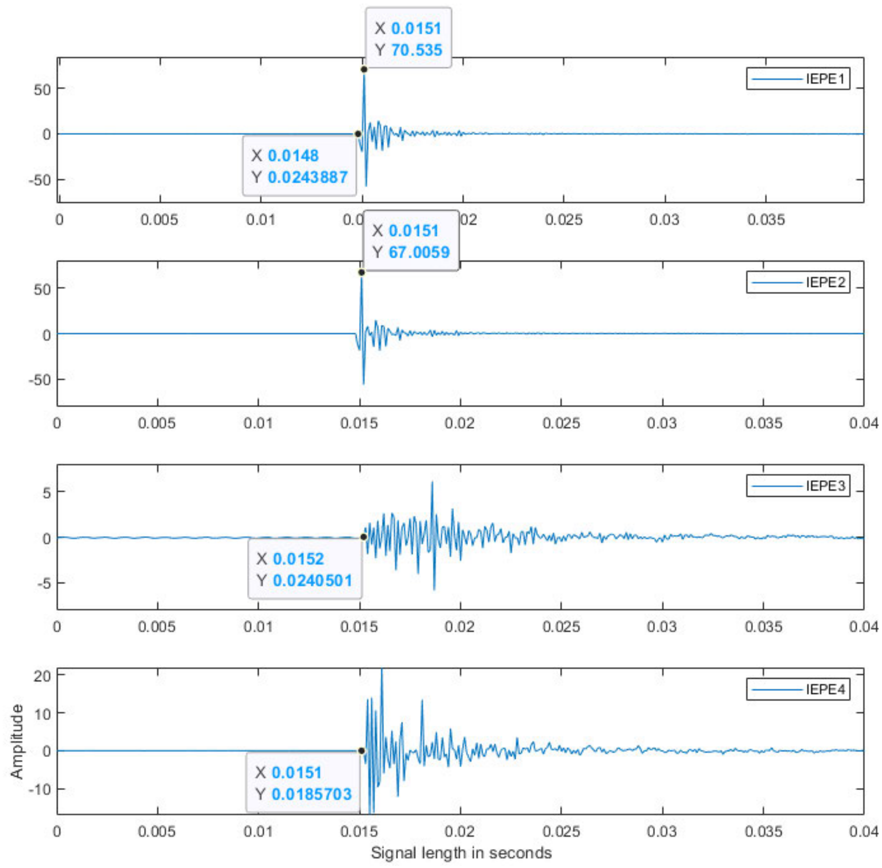

Figure 52: TD signals of shock impulse acceleration and propagation

After the amplitude inspection, it is observed that the very left data tip of IEPE1 determines the initial excitation of the impulse at the bearing housing structure and has no significant difference in terms of time state when compared to IEPE2. However, the effect of the experimental runtime difference, as described in Subsection 2.5.1, becomes evident and determines the wave propagation path based on the runtime differences of the defined sensor positions. In reference to Figure 52 , the runtime difference between the impact zone with $\boldsymbol{t}_{IEPE1} = 0.0148\ s$ and the baseplate sensor position $\boldsymbol{t}_{IEPE4} = 0.0148\ s$ is calculated to be 3 ms. Moreover, the value of the excitation at the drive sensor position $\boldsymbol{t}_{IEPE3} = 0.0152\ s$defines a runtime difference of 4ms. Therefore, the runtime delay of subsection 2.5.1 seems plausible, due to dispersion and damping behavior at bolted intersections of a structure. This is supported by the fact that IEPE 3 & 4 have an equal distance from the source of the shock. The fourth sensor at the base plate, in comparison to IEPE3, measures a vibrational amplitude of 22m/s². This demonstrates another dependency of the damping and form of the structure due to the low value of 6 m/s². Consequently, the initial acceleration of around 70 m/s² at the center of shock is reduced to about 10% consecutively along the transmission path. From now, the FD is inspected via FFT analysis shown with data tips in Figure 53. Note that, the following FFT's use the raw, non- envelope pre-processed, data sets and show the abortion effect. So the power spectrum is not representative, but its frequency response is.

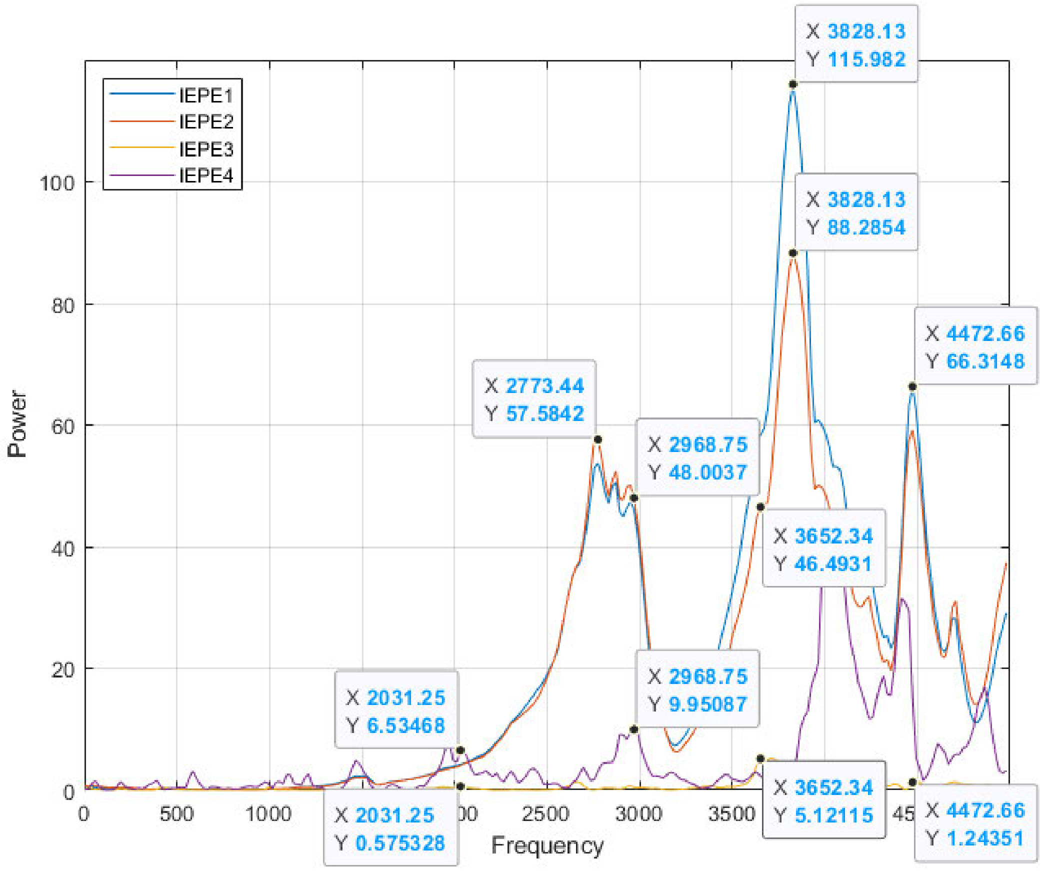

Figure 53: FFT of bearing housing shock with eigenfrequencies

Again, the first focus lays on the comparison of both housing sensors. Both sensors define the same frequency peaks and shape of the frequency response, which represent the eigenfrequencies of the housing structure. These are both accurately located at 2773,2968, 3828 and 4472 Hz within the measurable range of 5kHz, showing an exact congruency of both sensor types within the expected HF range of a very stiff structure. Surprisingly, the response of IEPE3 & 4 partly defines differing peak responses to the housing sensors. This certainly stems from the description in subsection 2.5.1, where each component of the structure is defined with an assigned frequency response. Sure, the peaks of IEPE1 and IEPE3 at 2773 and 2968Hz only differ equally with 193Hz, but do not represent a perfect frequency vise component of each other like in the steel transmission environment of the *StackOverflow* example of Figure 39. As the SVD function relies on a spectral based vector separation, this first outcome of the peak response test examines a major difficulty of the SVD application in a realistic test scenario of a test rig or wind turbine. To proof the runtime results of the first impulse on the housing to the drive system vice versa, the impulse on the drive support structure is examined and give the same result of a runtime of 4ms between the drive system and the bearing housing. Also the difference from the plate to the drive support is measured with 1ms. The FFT analysis of the drive side impulse signal does support the testimony of the Figure 53 frequency response and thereby the accurate measurement of the sensor setting. The mass of the housing is 22 times higher than the drive support. Due to this, the power of vibrations inside the bearing housing, in this direction of excitation, far lower.

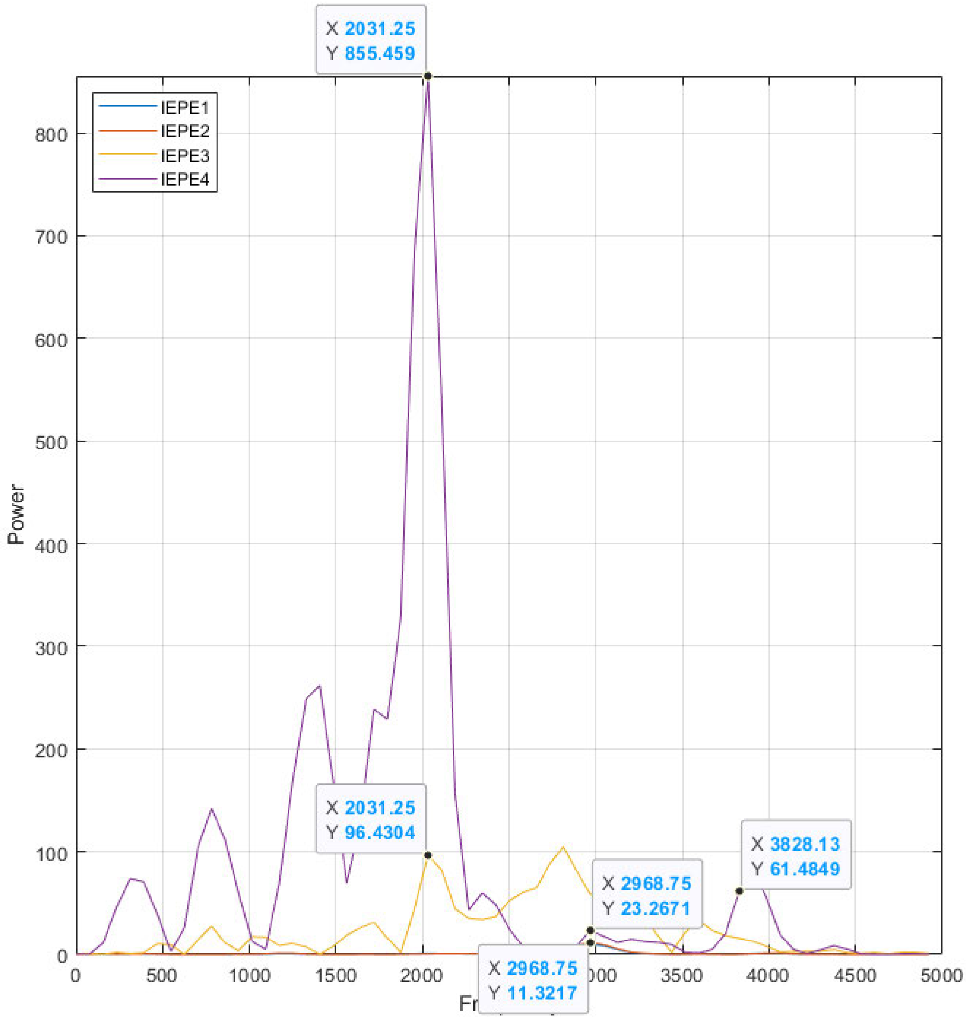

Figure 54: FFT of drive support shock with eigenfrequencies

6.2.2 Test 2: Pure Drive Operation Measurement

Having the idea to compare the output validation of the SVD output signals with the vibrational input signal demands a clear identification or characterization of one of the two inputs. Additionally the identification of significant signal parts could also help to purify mixed signals in a BEA based test scenario. So clearly, the contact vibrations are the vibration signature of interest, but the easiest and hence the first approach of a “solo recording” or decoupled drive system measurement takes place at the drive sensor’s position. As displayed in Figure 55, decoupled means a loosened drive train connection by the clutch, so torque and vibrations are not transmitted to the bearings on this way. As the base plate still connects the housing with the drive system, a limited wave transmission still takes place and enables further investigation of the vibration transmission without torsional connection in the frequency domain.

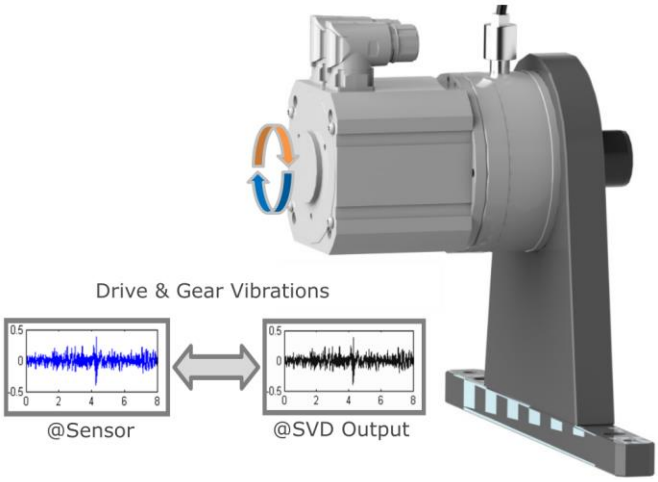

Figure 55: Decoupled drive system with signal compare approach [21]

The test design is very simple and refers to the next subsection's test number three. The drive's angular speed is set to 100°/s and refers thereby to the kinematics of subsection 3.3.1. The concept is based on a low load level which is induced by a friction creating device with about 0.5 Nm of constant torque resistance (see Torque signal in Figure 56). The friction device does not induce vibrations and thereby does not disturb the vibration signature of the pure drive signal. To find a profound data base for the FFT analysis, the TD signal is extracted from the full test data set as seen in Figure 56. This data set includes 100 revolutions of a warmup run to get the drive in a reference state of operation where grease is replenished within all gear stages and at a stable temperature. The two data tips within the position signal show the examined motion between the drive position $\rho_{Drive} = 0\ deg$ to $360\ deg$. Withing these datapoints, the friction is applied and leads to a vibration induction under steady conditions between $t = 388$ and $413\ s$ of the data set. For to this time span, the extracted data of the vibration sensors IEPE1, IEPE2 and IEPE3 are examined in the FFT signal. Note that, IEPE 1 & 2 is not shown in the following TD plot, as additional lines of data decrease the readability due to scaling.

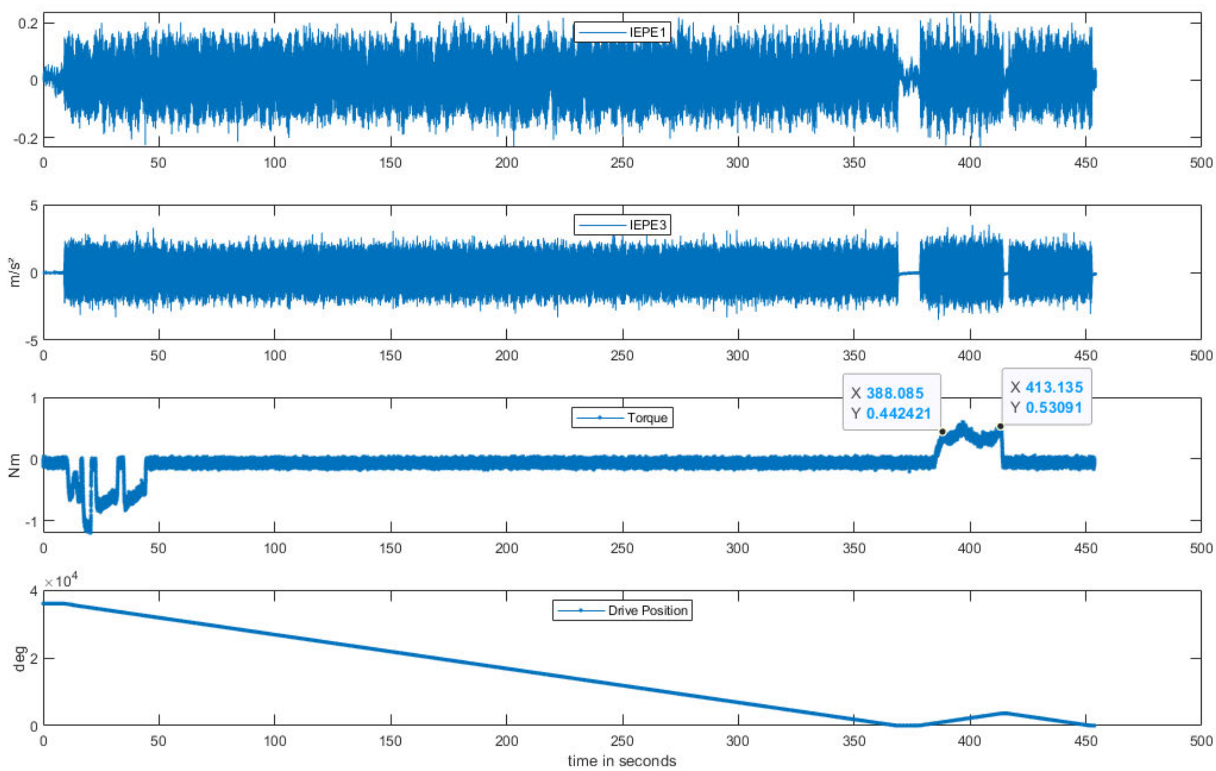

Figure 56:Full TD signal of relevant sensors

The inspection of the TD signal gives visual information about the IEPE sensor's sensitivity and the state of condition of the drive system. As seen in Figure 56 the vibration signal inhabits spikes in the signal, which could point out a component damage in inside the gear or drive system. Note that section 3.1 mentioned the high amount of test bearings under unfavorable test conditions, leaving the assumption that these, could in the past, damage the internal shaft and gear stage bearings as well. As this test provides an ideal environment to compare the sensitivity of the vibration signals of the BAM100 and BAM500 series, a quick inspection of the indirect and equally and limited accelerated (due to the lack of excitement inside the near bearing housing itself) sensors is performed. Anyway, a zoom of the IEPE signals in an overlapping *plot* show the sensitivity differences between the BAM100 and BAM500 in Figure 57. Here a slight difference between both signals is visible in the acceleration on the y- axis. Specially in the low range between 0 and 0.1 m/s² the signal of the IEPE1 sensor shows a higher output value than the IEPE2 sensor. At the peaks, the signal show congruity. In contradiction to Test 1 of subsection 6.2.1, the physical excitation of both sensors shall be equivalent, pointing out that the higher sensitivity creates a finer resolution for low energy contents. This empowers the quote of Waters in [6]. Nevertheless, slight deviations through connection properties like tightening torque of the sensor pin and boundary enhancer like contact wax or in this case, grease shall be taken into consideration, Even though they are accurately complied at the assembly process [52]. To get profound information about the vibrational characteristic and possible damage processes inside the gear stage and drive, the FFT tool is applied later.

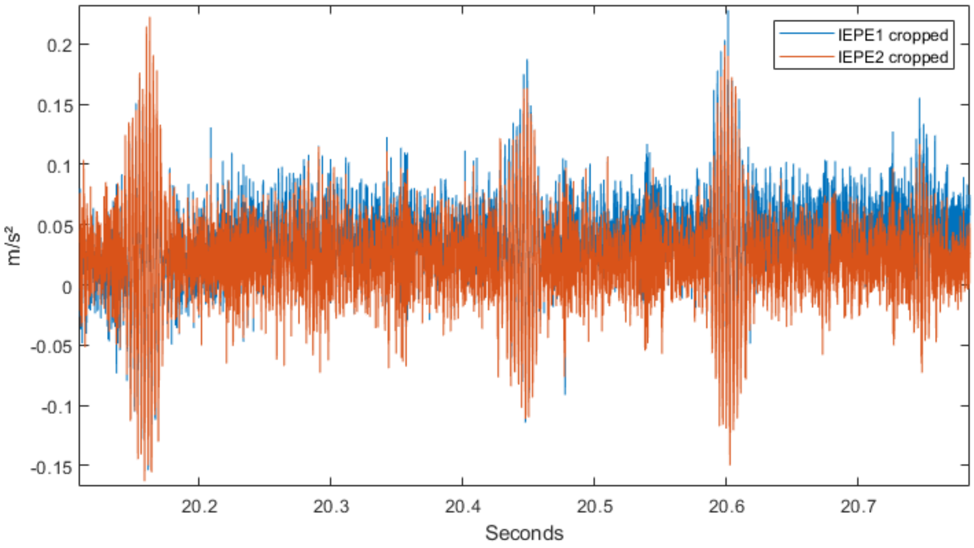

Figure 57: Cropped signal of overlapping vibrational bearing housing signal

To investigate the signals properties in the frequency domain, knowledge of subsection 2.6.2 is account with the envelope curve fitting. Reconsidering the fact, that a drive system is driven by a pulse modulating inverter with rather high modulation frequencies, and the knowledge of the FFT function that counts up signal components by the number of their appearance, regardless of they are integers or between, the expectation of high frequency share of the pure vibration data of IEPE3, is high. But, as mentioned within the BEA explanation, this would not benefit the examination of the signal and blur out the relevant high energetic peaks. This is clearly shown in Figure 59's FFT compare plot. Comparing the pure signal with the enveloped signal demands for a pre- processing of the pure TD signal shown in blue in Figure 58. The *envelope* function in *Matlab* does include a Hilbert- window function and its pre- set Kaiser filter with an ideal brick wall filter length of 8. By widening the length, the main lobe is widened and the amplitude of the sidelobes get reduced [78].

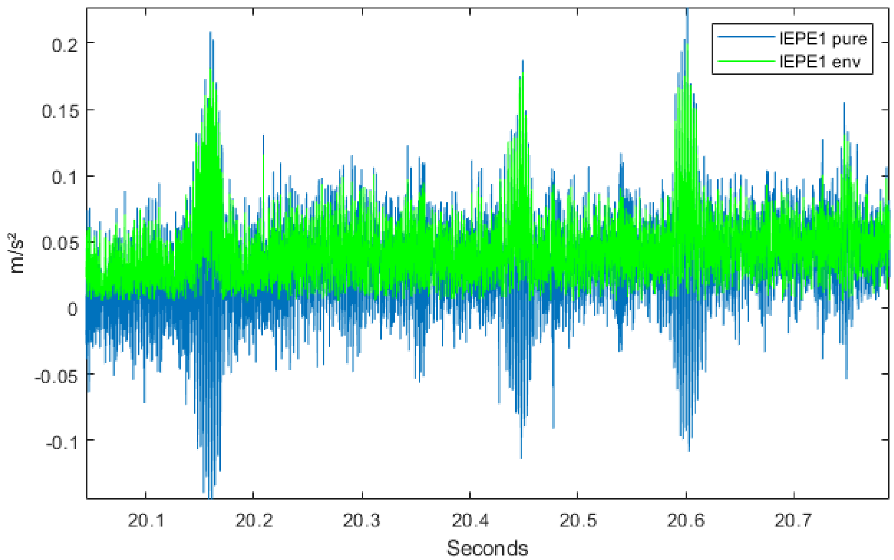

Figure 58: Cropped signal of pure and enveloped IEPE1 signal

So, the derived FFT *plot* of the IEPE3 signal can be seen in Figure 59. Like mentioned, the high frequency components of the drive are displayed in the red signal, showing little content in the LF range from 0 to 500 Hz. This range is most relevant for the LF overrolling signals and could simply be purified through the application of the *envelope* function before inserting the data to the *svd* functions input or use of a suitable low pass filter. From now, the blue enveloped signal of Figure 59 is used and inspected in the following plot.

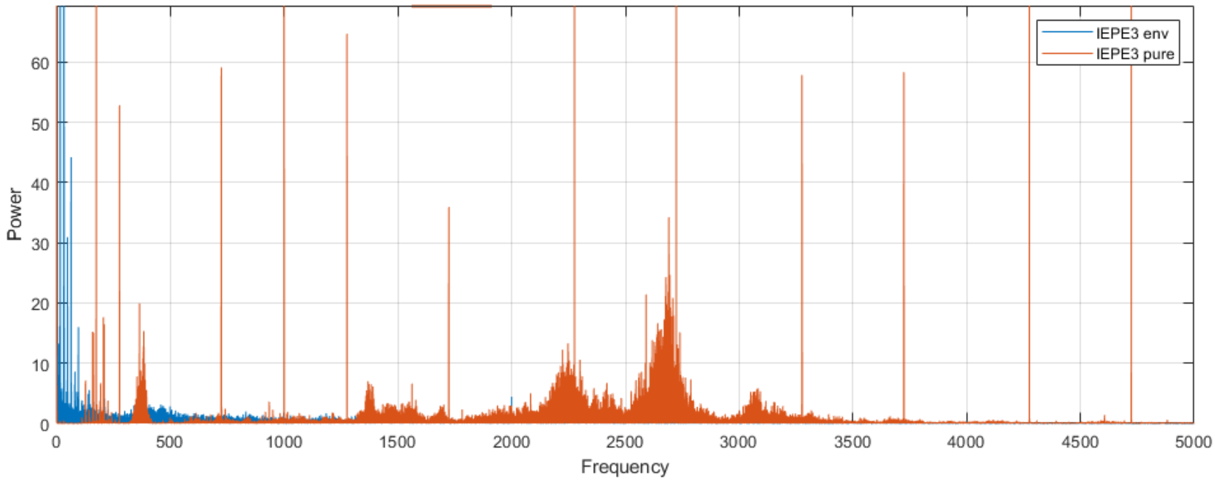

Figure 59:FFT envelope to pure signal compare

As mentioned in subsection 3.2.2 the inner geometrical relations of the *DRIVESPIN®* gear stages are not accessible to the author and leave reduction ratios, and thereby defined frequency bands for damage detection purposes, unclear. Anyway, Figure 29 shows a trochoidal gear structure, which should not produce gear meshing vibrations. This is confirmed in the enveloped IEPE3 vibration signal in Figure 60, where the major power content lays about the output frequency of the LS gear shaft and the drive's input frequency at the high-speed (HS) stage by the overall gear ratio of 57. This output frequency is trivially derived from Table 3 and gives a value of 0.277 Hz. Which corresponds through the gear ration of Table 2 with the high-speed shafts frequency of 15.846 Hz. To enhance the visibility of the most relevant frequencies, the x- axis is limited to a maximum of 70 Hz. Due to very low frequency contents above that, the loss of information is acceptable. The lowest frequencies show a high similarity to the LS shaft frequency and corresponds with the data tip of 0.267 Hz, which inhabits the highest power. Due to the data processing of the envelope curve fitting and changes of the drive speed along with the measurement, a deviations from the calculated output speed shall be confirmed. The second smallest significant frequency with 0.572 Hz is exactly double to the LS shaft frequency of Table 3 and could correspond to either a multiple deflection due to the FFT harmonics of the LS frequency, a reduction stage frequency for i = 2 or a overrolling frequency of the LS shaft bearing damage. For the latter, a possible source of damage could be derived, and at this position is most likely, as this needle bearing performs the exact same oscillations as the test bearing types. Without further knowledge a bearing defect of the gear cannot is not validated, leaving the examination of this frequency range, due to its possible influence on the measurement process, under higher load in subsection 6.2.3 in upmost importance.

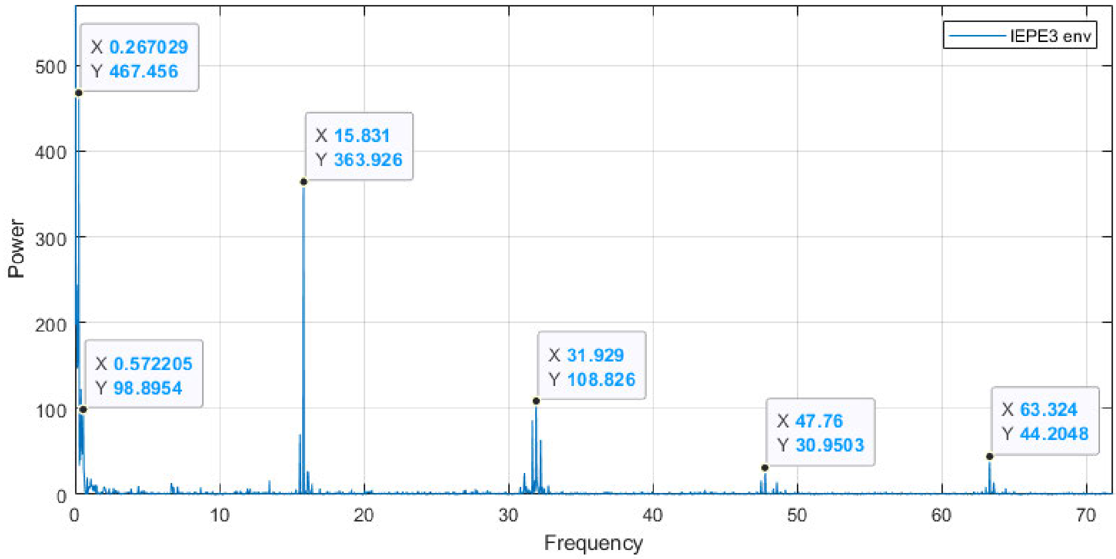

Figure 60: FFT plot of enveloped drive vibration in solo operation

Coming back to the vibrational characteristic for source separation approaches of the input signals, the higher peaks from 15.831 to 63.324 Hz play a minor role, as they are far away of the area of the BPF of a 7220-type bearing. To complete the examination, the definition of the 15.831 Hz is resembling with the HS shaft frequency, described in the last paragraph. The consecutively up counted peaks might be harmonics, as the match perfectly with the manifold of the HS shaft frequency. Due to lack of space, another *plot* with a direct comparison of the transduced frequencies (see reference of Test 1 in Figure 53) of the characteristics of e.g. IEPE1 is not shown here. This *plot* shows a very little vibrational power transition, in phase with the drive signal. So the vibrational characteristics of a realistic motion state get transduced without phase shift. So now, as this Test number two showed promising results on the pure drive characteristic, a more advanced test of the vibrational signal on the base of a BEA analysis is performed and checked for visible BPF related damages and characteristic frequencies of the drive.

6.2.3 Test 3: Endurance Run of Wear Pre-Damaged Bearing

As test number two showed promising results on the pure drive characteristic, a more advanced test of the vibrational signal on the base of a BEA analysis is performed and checked for visible BPF related damages and characteristic frequencies of the drive. Therefor a test procedure of a reference test within the HBDV project under the lead of Karsten Behnke is chosen. This test is priorly performed on a 2m real size turbine bearing and then transferred to the 7220-type for validation of the damage examination process on the BEAT0.1 test environment, loaded with $F_{axial} = 105\,kN$ [28]. Here, the first focus lays on the evoke of a wear damage by oscillating 40500 times around zero by ±2.25° and a ±4.5° regreasing run every 50th cycle to a defined quantity on the raceway, which then is continuously over rolled with a fixed drive speed of $\dot{\rho}_{7220\,=}\ 100\,deg/s$ for three full months. This test was not surveilled with high frequency data, as the DAQ system does run into performance errors as mentioned in subsection 5.2.2, so a data trending could be not performed. But the result of this test is a damage propagation similar to an incipient RCF effect around the wear marks, and thereby creates a perfect reference test to extract vibration data on a realistic example. The purple square damage zone in in Figure 61, taken of the 7220-type outer ring after the test, empowers the expectation on measurable vibrational emission. In total there are four major damage marks on the outer ring, and five on the inner ring. These marks are far more severe than the wear mark showed in Figure 14 and Figure 16.

Figure 61: Outer ring with wear and initial RCF damage after the test measurements

Hence to the consecutive test procedure and comparison to the kinematical properties inside a bearing, the overrolling speed is set to $\dot{\rho}_{7220=} 100\, deg/s$ and runs from the drives position $\rho_{Drive} = 0\ deg$ to $36000\, deg$. The vibrational data of all IEPE sensors is shown in the following Figure 62. In contradiction to the previous tests, the *plot* of all enveloped TD vibrational signals contains valuable information and is representing the main test and results of this thesis. The data tips are inspected from the beginning of the test (left to right) and are used as comparing range between the signal.

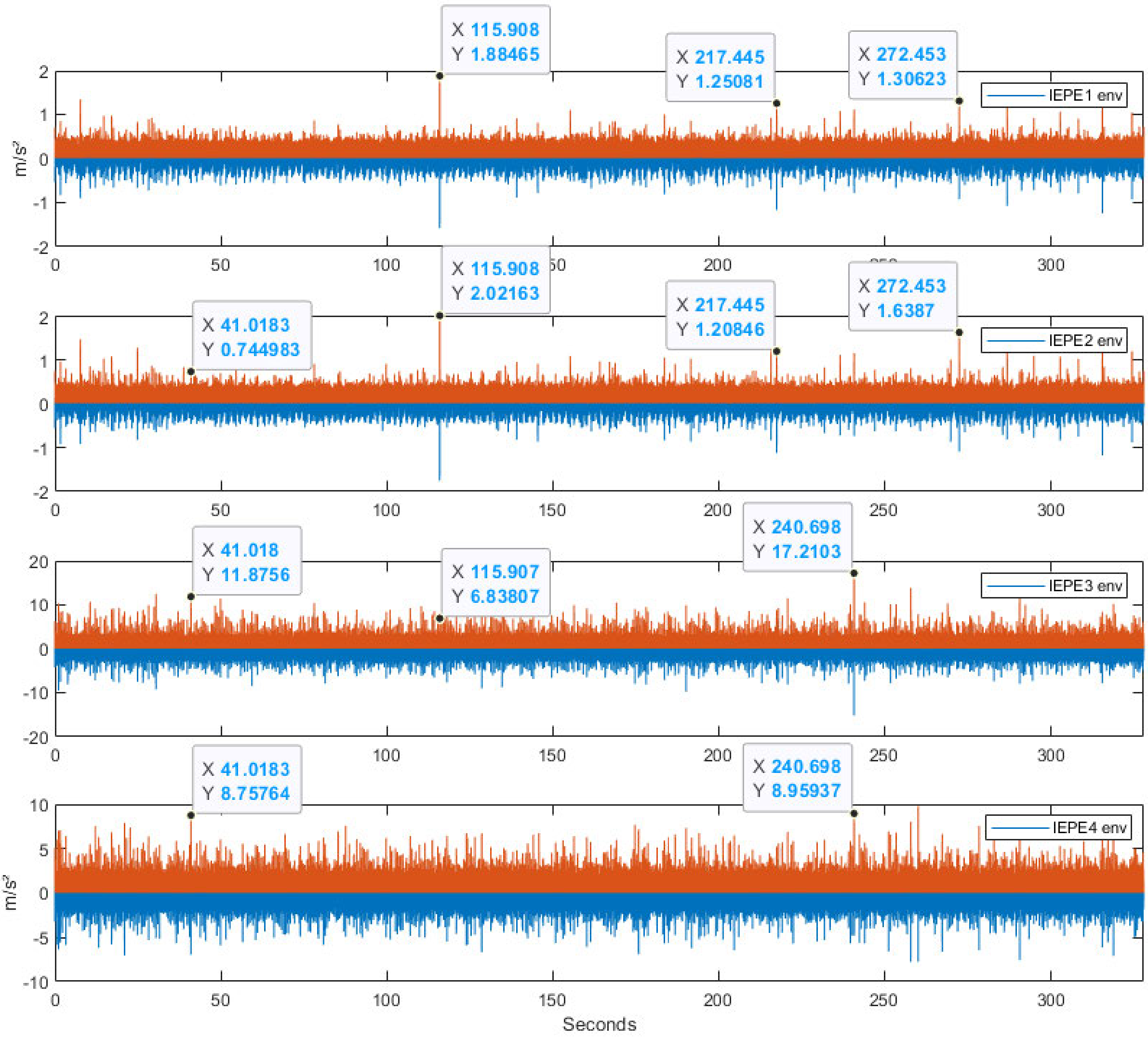

Figure 62: Enveloped time domain signals of IEPE 1- 4

The first impression of the overall compare shows a higher acceleration of the IEPE3 and IEPE4 signal, as these both components are expected to have a lower stiffness properties than the bearing housing. The first datapoint at $t_1 = 41.018\,s$ shows a strong excitation of the drive system $a_{IEPE3\_1} = 11.875\,m/s^2$. The IEPE2 sensor is excited with $a_{IEPE2\_1} = 0.745\,m/s^2$ and shows a responsive behavior. The second examined event is $t_2 = 115.908\,s$ where the housing sensor IEPE1 & 2 show the major peak of the overall signal. Here the peaks are clearly found in the IEPE3 data but have a less reactive response as the previous signal at t_1. This leads to the assumption that the main event at t_1 is sourced within the drive system and not created by damage of the 7220-type bearing raceway. This underlines the belief in subsection 6.2.2 of a defective gear component within the drive LS shaft periphery. Another useful detail at t_2, showing the difference of the acceleration of IEPE1 with $a_{IEPE2\_1} = 1.884\,m/s^2$ and IEPE2 $a_{IEPE2\_2} = 2.021\,m/s^2$ with 7.2%. The spectator is recognizing a difference in the peak designation of IEPE2 and IEPE3 at t_2 of 1 milli second. But, considering the zoomed view of Figure 63, this does not relate to the assumption of the signals wave propagation from drive to bearing housing as displayed in Figure 52. Here the figure of the pulse shows the event of overrolling and has its start at $t_{pulse\_start} = 115.899s$

and lasts for 13ms, shown in the data tip on the very left and right in Figure 63. This figure also shows the similarity of the shock response of test 1 and the overrolling of a defect at the present test configuration.

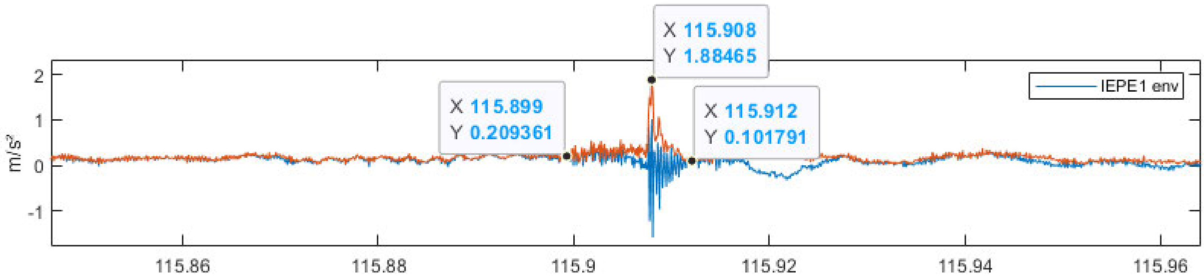

Figure 63: Overrolling pulse length of t_2 IEPE1 signal

At the third and fifth event $t_3 = 217.445\ s$ and $t_5 = 272.453\ s$ the impulse of IEPE2 is not recognizable in IEPE3 without extensive zooming operation, showing a very low wave propagation and high drive noise levels, consuming and thereby blurring the impulse energy of the defect overrolling. $t_4 = 240.698\ s$ affirms the idea with event of t_1. Taking the IEPE4 signal into scope, shows a property of a connection component, as the drive and housing signals are represented in the amplitude responses along the TD of the vibrational signal with wave related directional behavior. From now the inspection is continued in the FD via FFT analysis of the enveloped signals of Figure 62. From here, the findings and definition of the kinematic ball pass properties of subsection 3.3.2 and the CM related bearing fault recognition processes of subsection 2.6.2, find attention again. The aim is the full investigation of the overrolling process, due to its characteristic BPF and the designation of the characteristic drive vibration patterns of test 2 in subsection 6.2.2. The following Figure 64 shows the frequency response of the housing sensors IEPE 1 &2 (blue and red line) , as well as the outer ring ball pass frequency *BPFO* (- vertical line in red), inner ring ball pass frequency drive *BPFI* (* vertical line in green) and their individual third harmonics. Also, the output frequency of the low-speed shaft $f_{LS\_Drive\_0} = 0.277\ Hz$ (dotted vertical line light blue) is displayed and given with its first harmonics. The high-speed shaft is also represented by the very right data tip of the Figure 64.

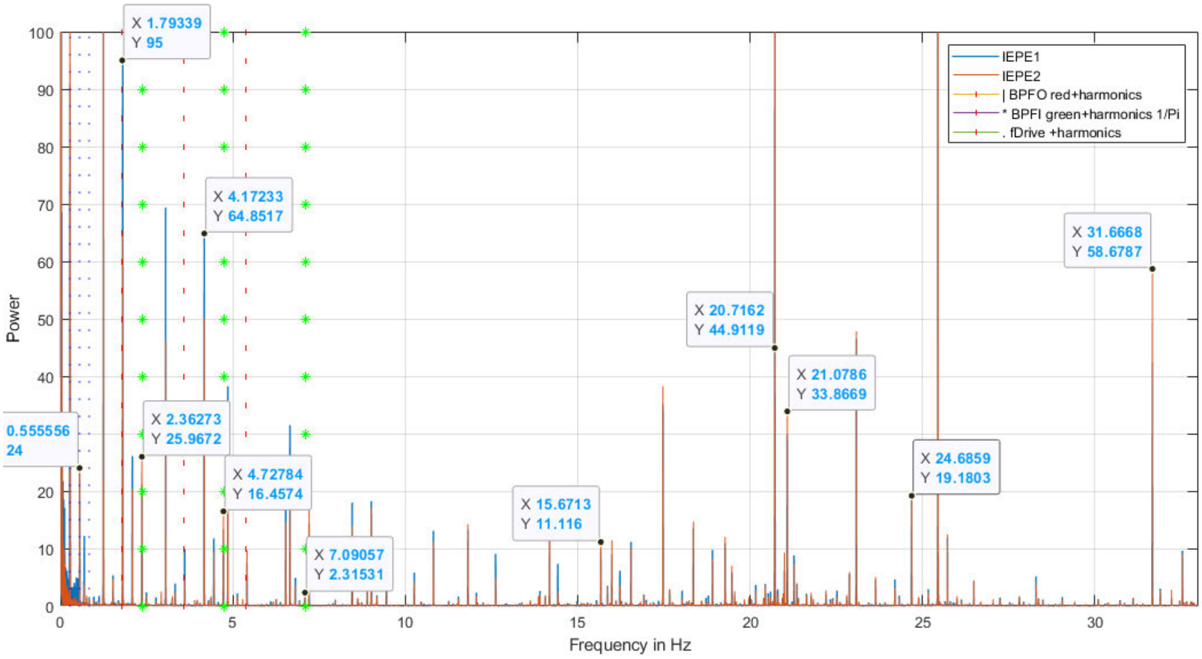

Figure 64:Frequency response with BPF and drive characteristics in BEA process

So first the drive values are scoped and described as clear representation for the calculated values of the LS shaft $f_{LS\_Drive\_0} = 0.277\ Hz$ and its first harmonic $f_{LS\_Drive\_1} = 0.555\ Hz$ due to the non-integer behavior of the FFT process. Not that more values could be defined with data tips but decrease readability of the given figures. The HS shaft input of the drive $f_{HS\_Drive\_0} = 15.864\ Hz$, takes a minor role in the frequency response of the IEPE1 & 2 *plot* but still comes close to the value of Figure 60. Note for the further that load conditions and slip can deviate the frequency values slightly between the calculated values and the results of the individual tests. Now, taking the example of BPFO (related to the damage areas of Figure 61), a clear impulse is given at the calculated close to the frequency value (- vertical line in red) of and represented by another two - lines of its first and second harmonic, which are not displayed due to lack of space in the plot. The power is the highest level of all BPF's and is assumed due to its favorable transmission path, closest to the sensor outside the bearing housing and the reduced amplitude power at the inner ring frequency, $f_{BPFI\_0} = 2.362\ Hz$ and it's first and second harmonics due to the damping property of a modulated signal with $1/\pi$. Having the envelope parameters set correctly, reduces the side bands of the modulation frequency $f_{LS\_Drive\_0}$ close to zero. Assuming the rollers surface, after inspection, as intact, the roller defect frequency BPFR is outlined. This is confirmed by the inspection of the frequency calculation with the value $f_{BPFR} = 1.499\ Hz$, and thus not listed in Table 3. Also the cage pass frequency is not given due to its plastic property and thereby low impulse effects when contacted with roller or raceway surfaces. In general, the data inspection of this test looks promising for further SVD processing or simple CM definition approaches, leaving the last task of this subsection to the sensitivity compare of the BAM sensor types in the following Figure 65. Hence the BPFO power spectra is compared with the BPFI, as the first is assumed to provide the purest base due to the limited transmission contacts from the source of bearing related vibrations to the accelerometer.

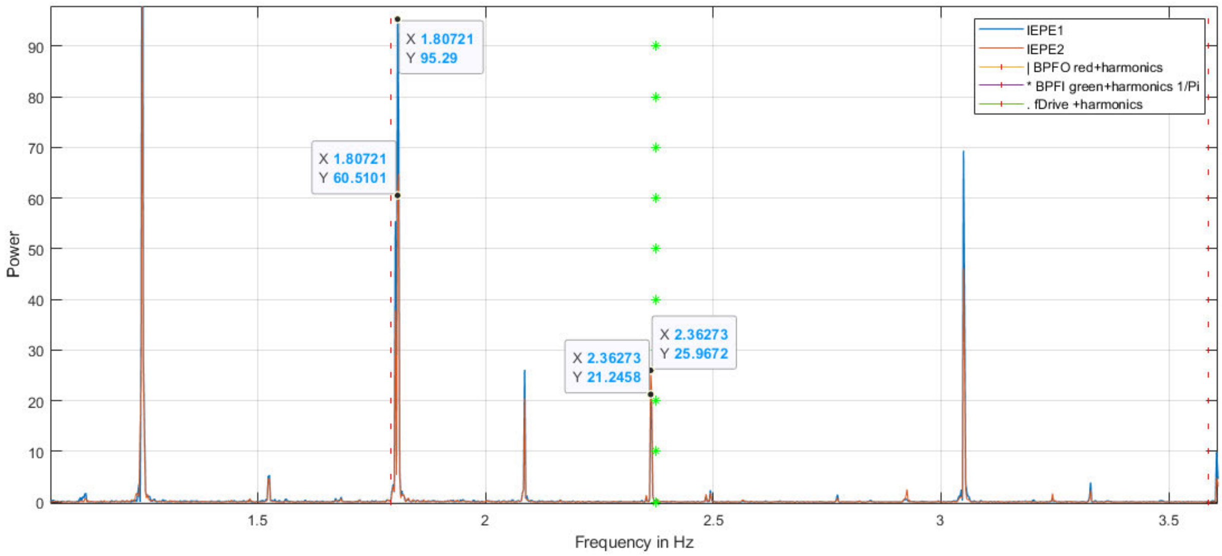

Figure 65: Comparing the sensitivity with power spectra of the BAM sensor types

So the BPFO shows a 36% larger power value of the less sensitive IEPE1 sensor with $P_{BPFO\_0} = 95.29$ compared to the IEPE2. This actually contradicts the IEPE2's (BAM500) design purpose of a more sensible sensor type and could define a linearity error of the lower sensitive IEPE1 (BAM100) or IEPE2 (BAM500) sensor type. Interesting facts emerge in the next frequency bandwidth of the BPFI, inversing the just mentioned effect with a relative difference of 18% on the right-hand side's data tips in Figure 65.

6.2.4 Test 4: Stepped cycle test with increasing bearing damage

Stepped cycle tests were originally designed to evaluate the behavior of the drives torque signal over an evolving bearing defect within the IBAC project of the LBL. Arne Bartschat and Eike Blechschmidt work on these test processes on small and medium scaled test rigs such as the BEAT0 and BEAT1.1 series [25]. To achieve a defect evolution and create comparable data, several harmful cycles were performed on a defined angular position and then over rolled to regrease the contact, before starting a higher cycle number on an offset angular position. Within this thesis, this test is selected to track the created vibration signals along with the step number. The idea is, to identify a threshold for minimum damage recognition ability of the measurement system and due to this, apply the SVD to purify the signals. But first, the classic BEA methods are applied to examine the general vibration and noise level within the characteristic vibrational component patterns. The basic set up for the test rig is derived from standard tests, with an axial load of $F_{axial} = 90\ kN$ and ten oscillation amplitudes of $\rho_{oscillation} = 0\ to\ 3.95 deg$ with one second break at the turning point as shown in the following Figure 67. These test profiles parts get repeated within the test rigs profile designer and thereby provide the desired number of full repetitions. Following Figure 66 shows the wear marks, spread equally over the race way of the 7220-type bearing after the performed test number four.

Figure 66: Test bearing with distributed wear marks over the full circumference

In this test design, seven stepped cycle tests are performed with an angular offset $\Delta\rho_{offset} = 6deg$ and 200, 500, 1000, 2000, 3000, 4000, 5000 cycles. Note that theses stepped oscillations are not tracked via HF sensors, as the duration of the cycle tests do not include valuable information for this basic approach within this thesis.

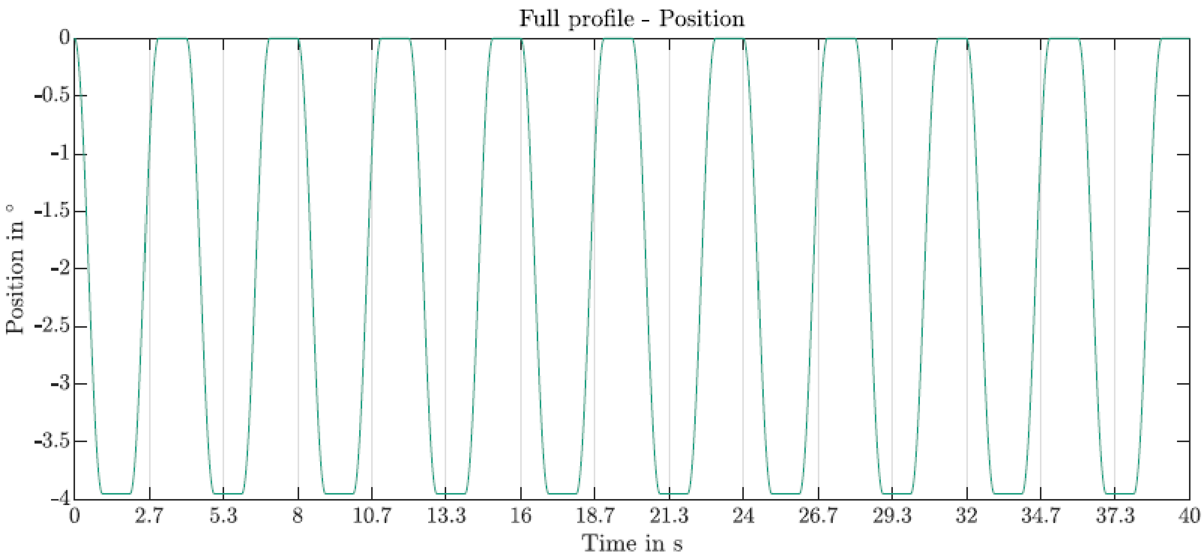

Figure 67: Motion pattern of the drive controller for the step design of Test 3 [79]

The most relevant part of the profile is the regreasing run of $\rho_{oscillation} = 0 - 180°$ between the cycles, where the high frequency sensors are activated and collect data of the vibrations. This run is performed at the very low reference test speed of subsection 3.3.1's Table 3 at a constant angular speed of $\dot{\rho}_{7220=}$ $10\ deg/s$. So the overrolling speed of this test corresponds with an exceptionally low pitch activity which could show another threshold for following WT pitch bearing investigation projects and will limit the amount of wear damage marks over rolled due to the low oscillation angle. Due to this, the power of the investigated signal is assumed to be very low, stressing the FFT examined vibration peaks and characteristics. So now the investigation, like shown in subsection 6.2.3 is performed for the vibrational data of the angularly increasing slope (of $\rho_{oscillation} = (-180°\ to\ 0°)$ of the grease run after 0, 3000 and 5000 cycles to compare an undamaged and pre-damaged bearing's vibration characteristic. So first the TD signal is inspected and shortly divided into the grease runs. So Figure 68 now shows the stitched grease runs in consecutive order. The pink square shows the oscillation before the bearing is damaged. This then gives an overview of the base noise signal in the following measurements, displayed with grey squares in Figure 68. One's eye might miss the signal of IEPE4, which is related to a malfunction of the cable connection along with this test. So IEPE1, IEPE2 and IEPE3 are the only representative signal. Next specialty is the difference between IEPE 1 & 2, which shows a totally differing TD signal in Figure 68. This proposal comes from the low $f_{LS\_Drive\_0}$ and corresponding BPF, which is in most cases below the lower edge frequency level of the low sensitivity BAM100 sensor, leading to very low signal content and noise levels within its data set. This test provides the option to examine the limits of both sensors, as well as the ability to define this low overrolling speed as suitable for test measurements based on CM and algorithm approaches within this thesis.

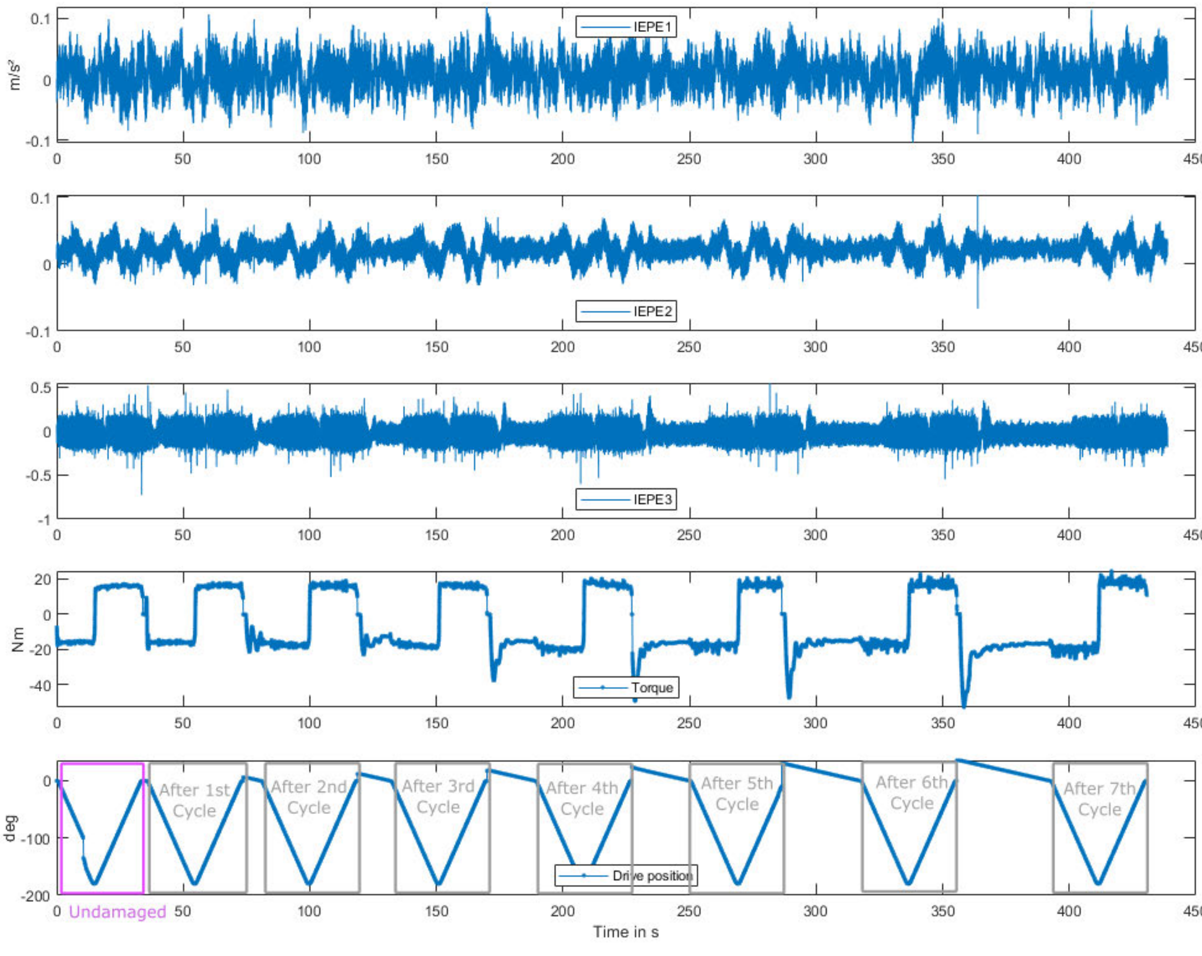

Figure 68: Stitched grease runs with HF and LF Sensor signal

The idea of an undamaged bearing measurement relates to the beforementioned desire to inspect the vibrational data trending over the course of damage propagation. Additionally, this test shall give an overview of the minimum detectable vibrational characteristics to define a sufficient amount of vibration to start with an SVD algorithm approach. Previous tests of Arne Bartschat in [25] show a measurable amount of damage related wear volume at the wear marks from 1000 cycles within the torque signal's peak of the *HBK* Torquemeter. So the following Figure 69, Figure 70 and Figure 71 show snips of the signal displayed and marked in Figure 68, pointing out significantly damaged area, over rolled with a very LS. So the first of the following figures shows the undamaged race way signals, with the drive speed $\dot{\rho}_{7220} = 100\frac{deg}{s}$ dependent BPF's. What falls into one's eye directly is the drive frequency value of $f_{LS\_Drive\_0} = 0.277\ Hz$ marked with the very left dotted line. Here a large peak rises along the y-axis but shows when, zoomed out of the Figure 69, that the line does not merge with a peak above, so this visualization is limited to a maximum of the power at 7. From this, no clear definition of the $\boldsymbol{f_D}$ can be derived, leading to the thought, that separation approaches fail already here, even though the second harmonic of the drive (second left dotted line in Figure 69, magenta in Figure 68)) seems to merge with a peak of the IEPE3 sensor (yellow line) . Note that the lower edge frequency of the BAM500 sensor is defined by 0.2 Hz in Table 4, supporting this quote of the author. Continuing the examination along the x- axis of the *plot,* the BPFO with a calculated value of 0.1793 Hz appears as red vertical dash line in Figure 69. Still under the lower edge frequency of the BAM500, and surely under the BAM100's (blue line graph) with 0.5 Hz, the latter shows a significant peak merging the red line. The high sensitivity sensor IEPE2 (red line graph) shows a lower peak at a higher frequency of 0.209 which is also displayed on the IEPE3's BAM100 data. As the following peaks of the IEPE2 signal show no direct merge with higher the higher BPFI and the drive's highspeed shaft frequency of $f_{HS\_Drive\_0} = 1.5864\ Hz$, the investigation does not converge with the results of drive characteristics of subsection 6.2.2.

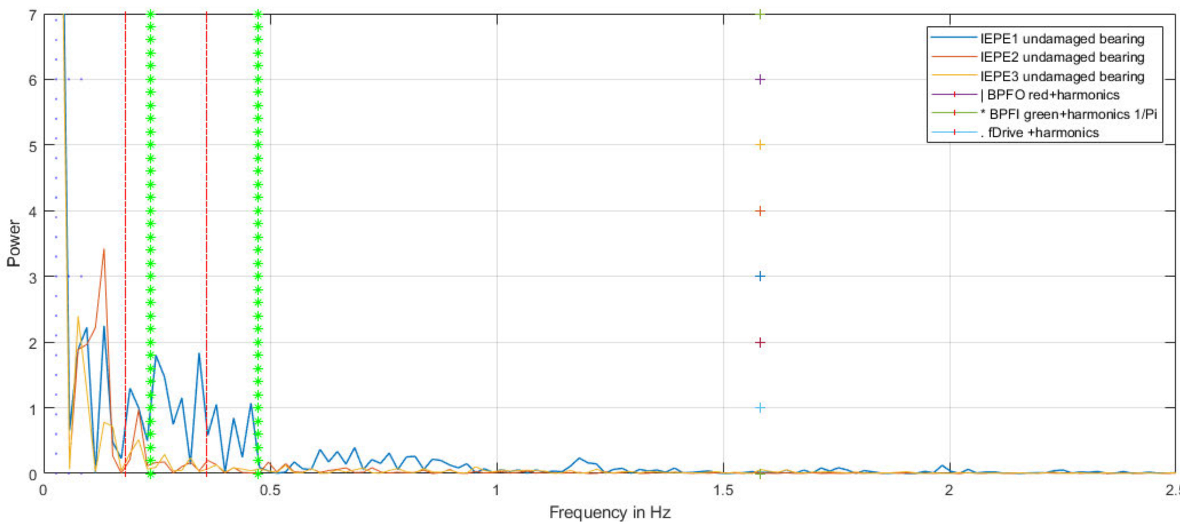

Figure 69: Close up zoom of frequency spectra of undamaged bearing

The next test cycle of the grease run takes place after 3000 damage cycles and should show a significant overrolling vibration, due to the emerged damage on the raceway. But the FFT *plot* of Figure 70 does not clarify a vibration characteristic either for the over rolled wear marks, nor for the drive system. So the investigation is continued to the results of the most damaged areas after the 7th damage cycle with five thousand oscillations in Figure 71.

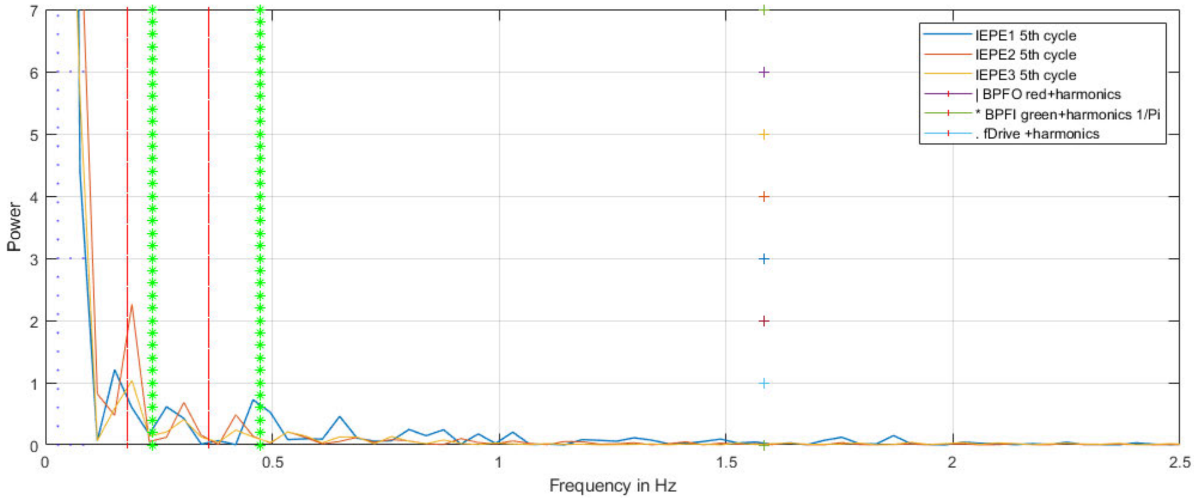

Figure 70: Close up zoom of frequency spectra after three thousand damaging cycles

Here the *plot* of the FFT signal process shows an even more confusing result, as the result defines the IEPE2 sensor, which is the only sensor with linear behavior between 0.2 and 14k Hz, as fully excited around the drive frequency $f_{LS\_Drive\_0} = 0.277\,Hz$, but close to zero at the BPFs. IEPE1 defines, same as in the previous Figure 70, a significant peak around the BPFO. Unlikely to the previous results of Test 3, the harmonics show very little to no acceleration power within the signals of the three IEPE sensors.

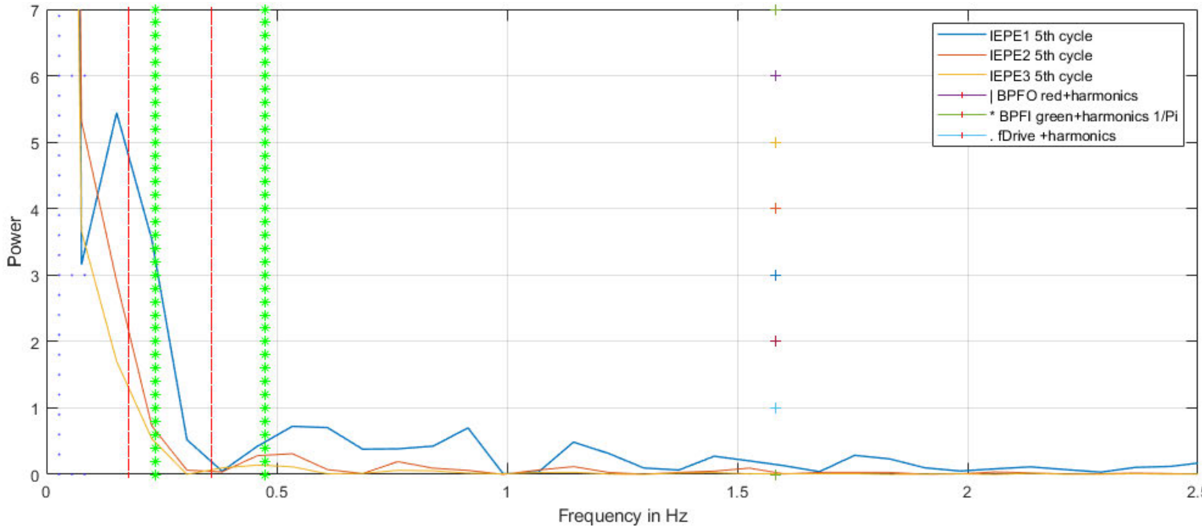

Figure 71: Close up zoom of frequency spectra after five thousand damaging cycles

To proof the results of the short time data inspection within the last three figures, a full signal analysis will help the assumption of an unfavorable vibrational state of this low-speed measurement. Here the signal peaks have very little relation to the single signal peaks of the Figure 69, Figure 70 and Figure 71 and create the impression of an impropriated cut off frequency (0.5Hz for the IEPE1 & 3) for this low speed related evaluation. Also the number of peaks does not purify with increase of the *envelope* functions Hilbert filter order. The impression is set, that longer measurement periods could clarify the peak designation more accurately and is displayed in Figure 72 with the same color designation of the line graphs as the figures before.

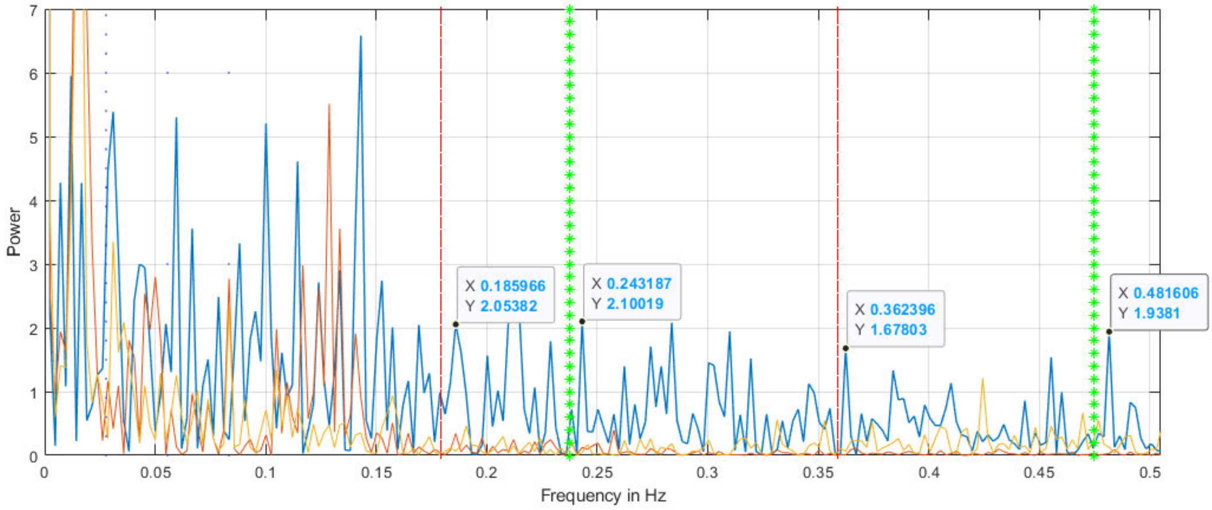

Figure 72: Close up zoom of frequency spectra all regreasing cycles

Generally the results of this test show a strong deviation or blurring of the frequency response behavior, compared to subsection 6.2.3's results. Reasons for these deviations were mentioned within the test properties like roller speed and test duration (numbers of samples). Also possible, is the test bearings cage design, which leaves a one-millimeter gap of the diameter between the roller and the cage's wall. Hence, the distribution of the fifteen wear marks for each damage cycle might be inequal, blurring the impulse cumulative for each over rolling event. This effect might be even worse, due to the disordering effect of the rollers inside the cage after several oscillation cycles. One mind would assume the same effect in WT bearings but might forget about the high load zones of a pitch bearing (as displayed with the bending moment in Figure 9), which would rather limit the emerging and distribution of damaged areas to a high loaded raceway area of the bearing comparable to the wear mark emerging within test 3 (see Figure 61). Consequently to the low performance and uncertainties of these pre-examination evaluations, this test is not a subject to the SVD based separation approach of the following chapter 7. Considering the yet not sufficient signal duration for this basic FFT analysis, the decision is also supported through the very short signal durations of the SVD input which reduce the information content of Figure 70 to Figure 72 even more.

7 SVD Process Application on Test Structure

This chapter is referring the definition and description of the *Coursera* [59] SVD processing example. The idea of this approach is the investigation of the code's ability to separate the incoming mixed signals of the vibrational sensors IEPE 1/ IEPE2 and IEPE3. As verified in the previous subsections 6.2.1- 6.2.3 the input signals consist of frequency components of the counter signal. Meaning, that the IEPE sensors on the bearing housing contain a mix of their own source of vibration, as well as the transmitted vibrations characteristic of the drive system. Considering the ability of the SVD function to perform a spectral differentiation, the signal component of each countersignal shall be reduced. Considering that the code structure is based on a homogeneous transmission medium (air), the author assumes that the transmission behavior of the isotropic test bed environment will be adapted to this transmission behavior. This is achieved by normalizing the input signals and reduces the influence of the stiffness-dependent vibration behavior of the individual measuring points. To double check this thesis of transmission behavior, the author performed tests with normalized and original signal input, showing no significant difference to the separation results. The geometrical relations of the sensor and source diameters are defined by subsection 4.2.3 and displayed in Figure 38. From here the code performance in terms of separation efficiency and calculation power needed is inspected and related to the process of the subsection 4.2.3. The input signals are yet characterized in the FD by section 0 and used to testify the results. Therefore an analogy like shown in Figure 35, shall help the reader to see the verification of the SVD output with the drive's characteristics.

7.1 Performance Evaluation of Test 1

This test structure is used to inspect and compare the system's basic behavior or frequency response for external impulse excitation. Now the enveloped and normed signals of the housing sensor, as well as the signals of the drive system are fed into the *svd* processor and compared in the TD and FD.

7.1.1 Time Domain Signal Input and SVD Output Examination

The input inspection is giving a brief overview of the two selected data sets, prepared to be processed with the *svd* function in *Matlab*. Generally these signals do relate to the evaluation of section 0, but need extensive cropping, as the processing time for a long data period is exceeding the existing calculation capacity of the used computer. For this specific impulse test of the bearing housing excitation (see Figure 52), the signal length is short, as the impulse provides only 65ms of damped oscillation. The inputs then get normalized via vector normalization [80] and stored in the array *a.* This normalization of the input is providing a comparable input power for the component related vibration characteristics. Figure 68 provides these signals in a raw format and shows the higher energy input of the softer baseplate and drive support structure. The stiffer housing signal of IEPE1 & 2 shows comparable low energy content, To track down the *svd* code's calculation power, the *tictoc* function is used and defines a calculation time of 9ms For this noticeably short data sample. Note that background tasks can slightly deviate this result, so only relevant programs run parallel to the code execution. Feeding the input value and the first and second column of the output array *v* in the *subplot* with adjusted amplitude labels for the y-axis creates the following Figure 73. Here the two signals were merged with a little offset to each other to show their similarity. Except the reduction of the output's amplitude signal to half the input amplitude, the signals show convergency. As this code now relies on the runtime difference to map the state vector like described in 4.2.2, given by the examination of the impulse transmission in subsection 6.2.1 with 4ms.

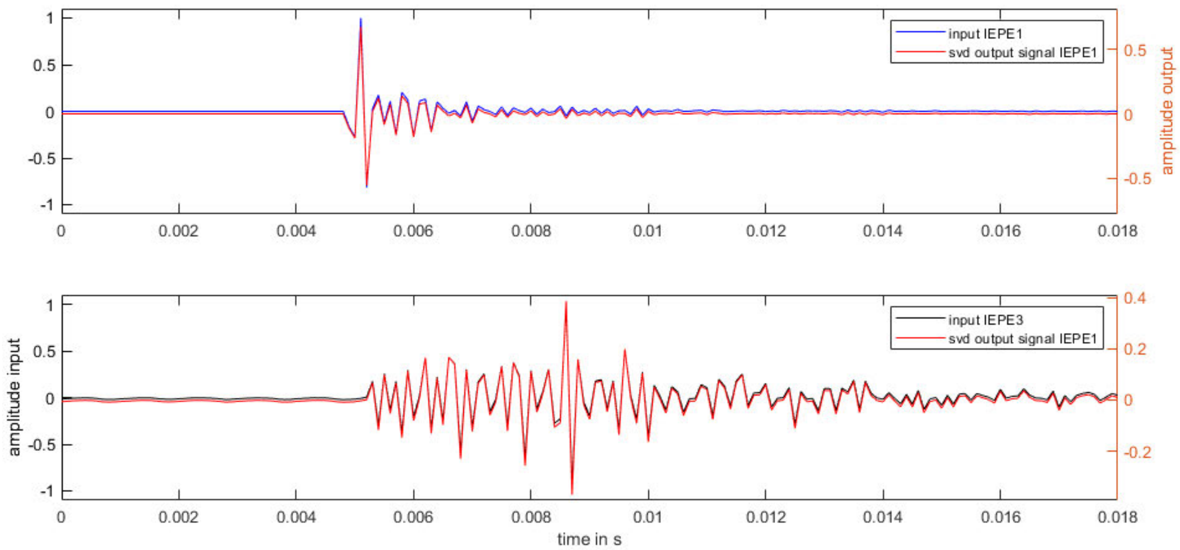

Figure 73: Test 1 TD signal compare of SVD in- and output

7.1.2 FFT Input and SVD Output Examination

The TD signal does not show an impact on the data plot in Figure 73, except the amplitude reduction. So the FFT analysis is performed to extract possible changes. Therefore the SVD outputs get normalized to create a comparable power spectra to the yet normalized input signal of the IEPE sensor. Within this normalized input signals the FFT function provides the following *subplot* of with a totally converging frequency response for the drives IEPE 3 signals in Figure 74. The housing signal of the SVD output shows an increase in signal power via svd processing. The author might assume to see an amplification or purification of the desired housing vibration signal but has doubt about the untouched IEPE3 signal power. Due to the findings withing the FFT plot of the air transmission environment in Figure 37, an increase in signal power shall create a reduction on the other signal source, specifically the IEPE3. So the interpretation of this result is not successfully interpretable.

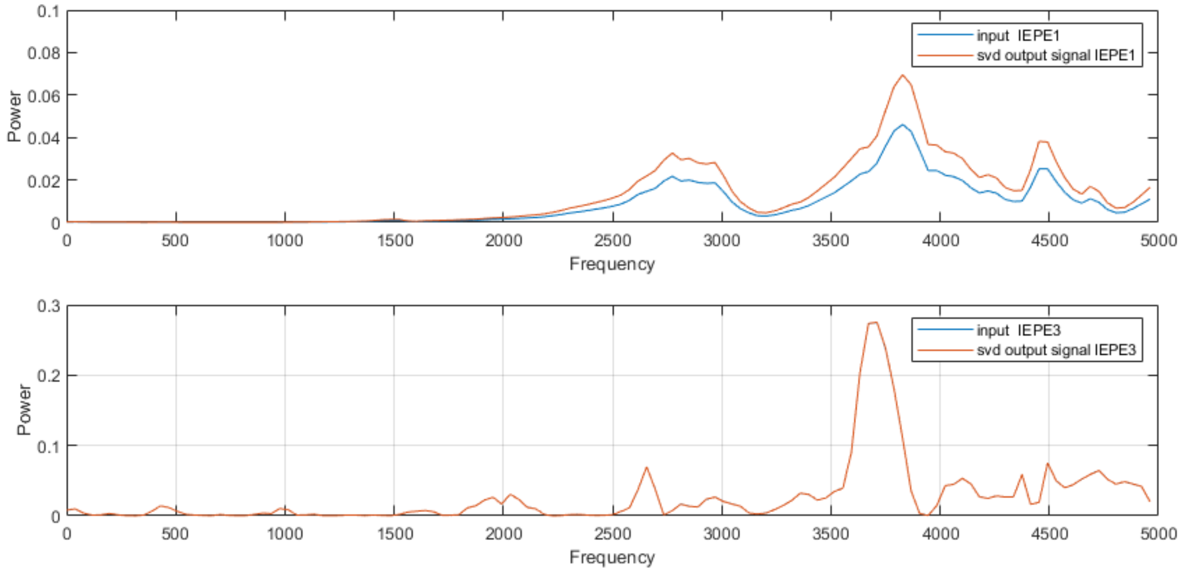

Figure 74:Close up zoom of Test 1 FFT signal compare of SVD in- and output

7.2 Performance Evaluation of Test 2

The now inspected pure drive operation is thought to reproduce the previous examination in subsection 6.2.2 with additional information about the code performance and compare of SVD related FFT results. To execute the SVD function a drastic data cropping needs to be performed. This is related to the limited computing power. So the data amount is limited from a 25 second time domain signal of subsection 6.2.2 to a one second signal snip for a calculation effort reference test, than a two second signal Input for FFT examination (see Figure 75) of the full time signal *subplot* shown in Figure 57. This short signal provides several peaks and should therefore produce an number of characteristic vibrations for the higher frequency areas above the level of the drive's frequency. Also interesting for the further data processing approaches within test rigs and turbines, is the run time of the code to process a limited snip of the five kHz signal. At the first reference calculation it requires 225 seconds for the separation attempt of one second of signal length. Considering the demand of long signal duration and higher sample frequencies, which could increase the resolution of the output data, this processing demand is also increased with the number of processed signals. In a larger test rig or wind turbine, this number is expected to be much higher, due to the additional inducing noise sources. Considering this fact, the potential for a real time supervision and separation of the vibrational signal of a pitch bearing is rather limited.

7.2.1 Time Domain Signal Input and SVD Output Examination

The normalized two second input signals for the time span of 339.3 seconds to 341.3 seconds are provided in Figure 75. Now the analysis for the SVD function begins and contests a large calculation duration of 1666s for the given TD signal of Figure 75. Considering the calculation time of the other reference profile with one second the calculation effort seems (with the limited knowledge about internal processing steps inside the SVD function and the *Matlab* processor) to follow a square rule for signal length in seconds. Note that the PC does not achieve longer data samples, even though virtual RAM of 60 Gb are assigned for the calculation within the SSD storage, which limits further examinations to this length. The effort for SVD processing comes crucial with the ratio of calculation performance to the accuracy of the results, as the FFT function demands large datasets to clearly define peaks within the characteristic signals. Considering the example of the calculated drive frequency of the low-speed shaft $f_{LS\_Drive\_0} = 0.277\ Hz$, a minimum of 3.59 signal length in seconds shall be calculated to provide a full rotation signal information, which is the minimum requirement to track a frequency component in a signal. Note that better the double of this signal time shall be measured to prevent the aliasing effect for harmonic oscillations due to Nyquist- Shannon [76]. In the following Figure 75 the TD test signal are now displayed in blue.

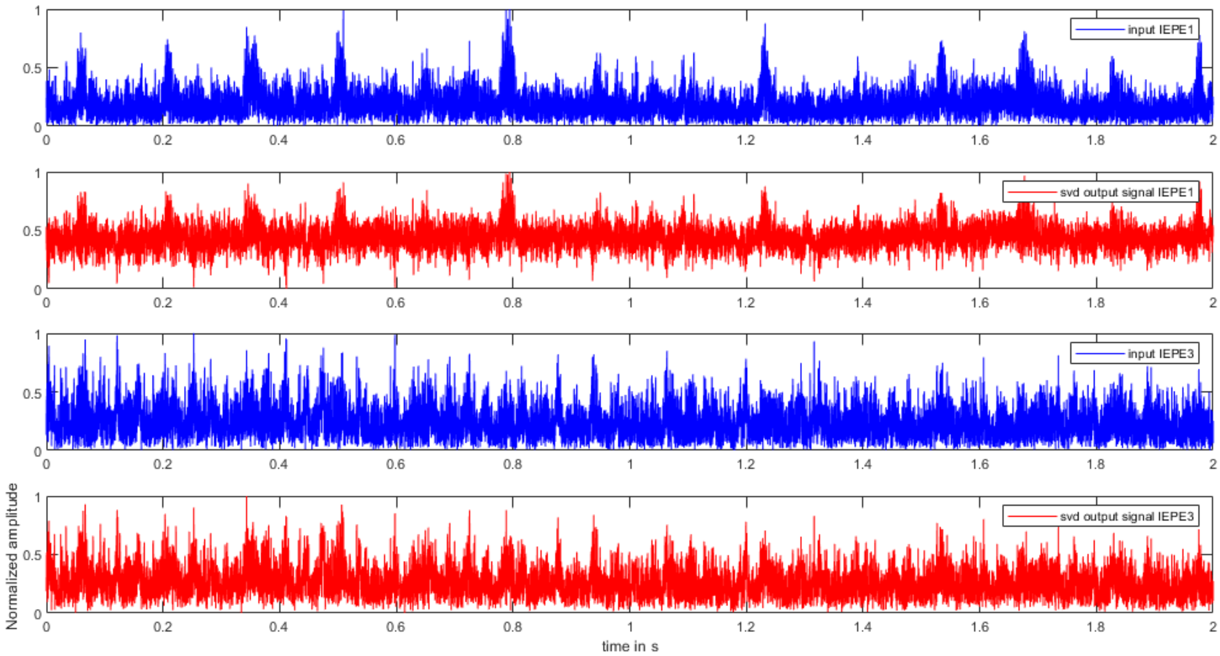

Figure 75: Test 2 TD signal compare of SVD in- and output

Below each signal, the again normalized output of the SVD function is displayed in red. This figure differs slightly from Figure 62, as the overlapping two row *subplot* would here fade the qualitative information of the signal compare. This information results from the inspection of the peaks within the input-/ output. Here a slight deviation is given, contesting a basic functionality of separation algorithm. Here the peak around $t = 1.2\ s$ seconds in Figure 75 shows a shift of the signal component from the IEPE 1 to the IEPE3 signal characteristic. But the TD still does not provide clear information of the frequency characteristic, which is the main object in signal designation. The next subsection shows the FFT analysis of the given and calculated signals.

7.2.2 FFT Input and SVD Output Examination

So now the data compare of the input and output signals of the two main sensors IEPE1 and IEPE3 is displayed in Figure 76. The primary object of interest is not the frequency region for the drive's LS shaft and the high-speed input shaft. Here the results of the signal snip with 25 seconds, displayed in subsection 6.2.2's Figure 60 is referenced. These frequencies show a clear characteristic at around 0.267 and 15.831 Hz and produce two or more harmonics. As these frequencies are characteristic for the drive operation, a determination of the drive noise within the SVD signals of the IEPE1 & IEPE3 signals could be simplified. Ideally, this leads to a separation of the signal, via drive characteristics. Note the beforementioned frequency limits due to the limited signal duration in relation to the existing signal length and anti- aliasing apply for the low signal frequency are below 1.5Hz.

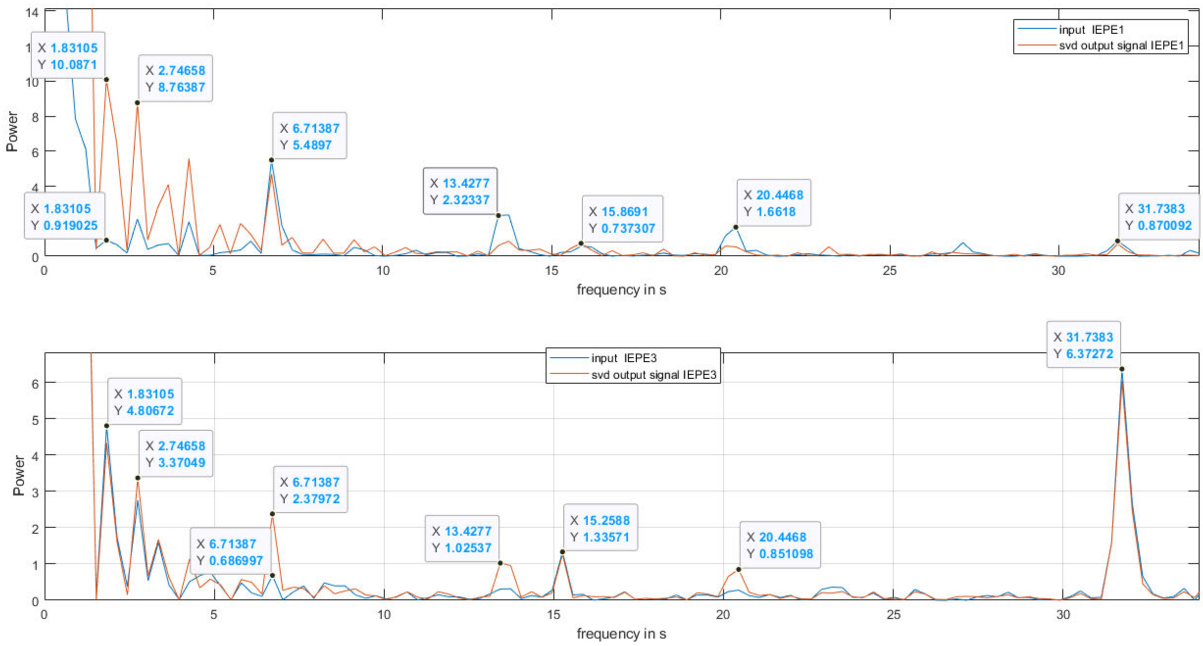

Figure 76: Close up Zoom of Test 2 FFT signal compare of SVD in- and output

Inspecting the results in Figure 76, one's eye would directly point at the 15.258 Hz peaks in both signals. Assuming the HS motor frequency would take a major lead in the signal's power amplitude. In fact this is not the case. Also the separation performance at this specific frequency does not show a relevant change. But the value of 31.738 Hz shows a reduction of 20% and within the IEPE1 domain and a high value within the IEPE3 sensor domain. Considering the short duration of the signal snip, the result of the lower frequencies from HS drive frequency to the last peak of 1.8 Hz shall be considered but cannot be qualitatively described by its source. Having the impression of the first basic results, the SVD process showed very low or even nil deviation within Figure 74. With the frequency response of test two, this impression is not confirmed. Taking the exemplary frequencies of 20.446, 13.427, 6.713 Hz as an, the behavior of the power separation/shift (as seen in subsection 4.2.3's Figure 37) from one to the other sensor, is affirmed. It is clearly seen that the values of 20.446 and 13.427 Hz (with 283% and 227% reduction in IEPE1) shift their power from the IEPE1 Input's signal to the IEPE3 SVD output (Increase with 301% and 320%). Which is the expected behavior for a successful separation. Another peak around 6.713 Hz shows the same behavior but with limited reduction with 15% from the power of 5.48 to 4.68. Besides these results, the power shifts are less logical, as all peaks on the left side of 6.713Hz increase in their synthetic output, regardless to the number or better said, position of the IEPE sensor.

These contradictions, as well as the limited ability to clarify the source of frequencies within the gear construction limits the value of the overall result of the solo drive operation evaluation number 2.

7.3 Performance Evaluation of Test 3

The preceding investigations within chapter 6 showed a valuable outcome of the vibrational signals, created by overrolling the pre- damaged bearing of the test design number three. Here a clear definition of bearing damage could be derived of the characteristic frequencies within the BEA related frequency analysis within Figure 64. Now the SVD function shall perform a separation attempt to proof the ability of a vibration characteristic. For this purpose again, a two second signal snip is extracted, enveloped and fed into the function. This test marks the main reference for the thesis related investigation approach, as it relies on realistic motion profiles and load conditions within a turbine. Unfortunately the examination of the proceeded test number two, showed limitations in the LF examination due to the short signal duration observable. Without options to change these circumstances the following analysis, again, refers to higher frequencies than 1.8 Hz. But here the significant BPF are calculated in Table 3 and should be visible due to their elevated values of $\boldsymbol{f_O} = 1.793\,Hz$ and $\boldsymbol{f_I} = 2.373\ Hz.$

7.3.1 Time Domain Signal Input and SVD Output Examination

To find a possibility to track two primary events, the full signal gets inspected and searched for a double event enclosed in two seconds of time. For this purpose several areas are identified and consequently tested to find the most significant part. The options will be preset as time steps within the code as variables *start and stop* representing the points with two second distance. The part, shown in Figure 78, is representing the time boundary between $t_{start} = 165.92\,s$ and $t_{stop} = 167.92\ s$ within the full TD signal of Figure 62. Referring to the findings in the before gone test number two, a slight data shifting is performed by the SVD function. This is visible e.g. around $t_{shift} = 0.82s$ of the IEPE 3 signal domain. In general, the IEPE 1 signal shows a stronger peak appearance, which could point out the higher LF content of the signal.

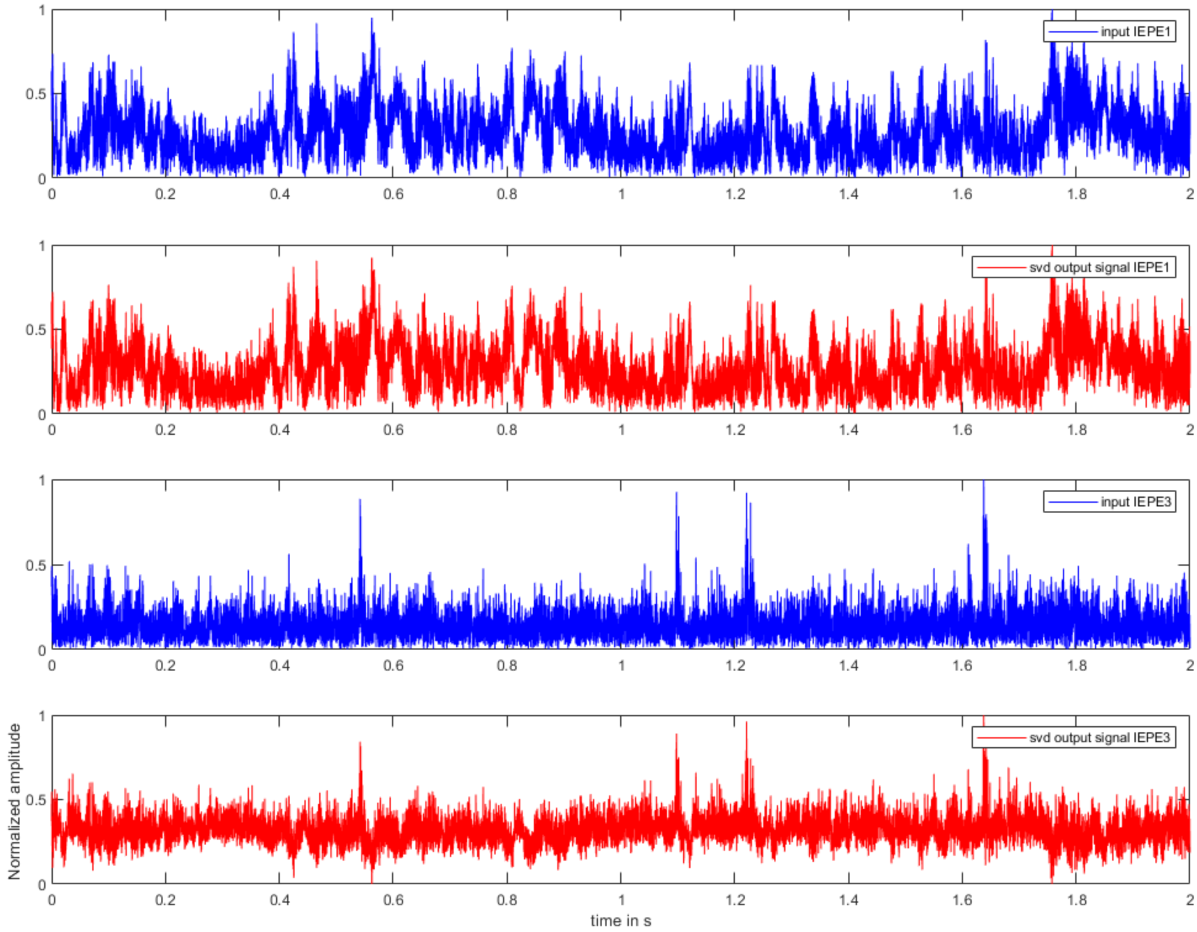

Figure 77: Test 3 TD signal compare of SVD in- and output

7.3.2 FFT Input and SVD Output Examination

Similar to the foregone evaluations, the close-up view of the FFT spectra is displayed in Figure 79. But this time the full spectra of the FFT is shown and shall present the higher frequency components of both signals as well. Here a strong HF power spectral group is detected between 2500 and 3200 Hz and a weaker field between 1 and 1.5 kHz such as 3.7 kHz and 4.2 kHz are calculated for the IEPE1 sensor. This finding merges with the results of the eigenfrequency evaluation in Figure 53 and Figure 54 of the single pulse excitation test subsection 6.2.1. The frequency response of the IEPE1 at around 400 Hz does not fully conclude with the results of Figure 53, but matches with the peak responses of the baseplate eigenvalues of IEPE4 in Figure 54. The drive support sensor on the IEPE3 signal also defines a lower power field around 3 kHz and is excited at this range of Figure 54. But still it is not totally acknowledged how strong the influence of a high mass component, like the bearing housing, with a low mass drive component is. Clearly the housing defines higher stiffness and thereby creates higher eigenfrequencies as the soft and slender drive support (compare Figure 53 and Figure 54).

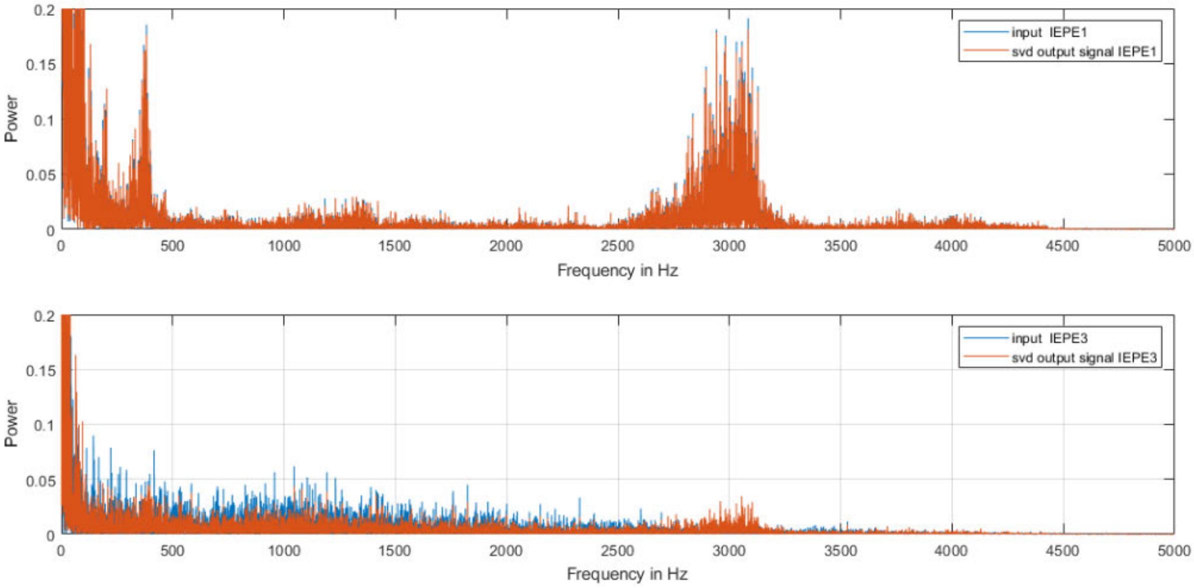

Figure 78: Full spectra of Test 3 FFT signal compare of SVD in- and output

Again, the lowest frequency components of the LS shaft output and harmonics, are not visible due to the short signal duration and end up in a high power zero crossing of the x-axis at the power of 450 at both sensor domains. Note that the y-axis scaling differs in Figure 79.

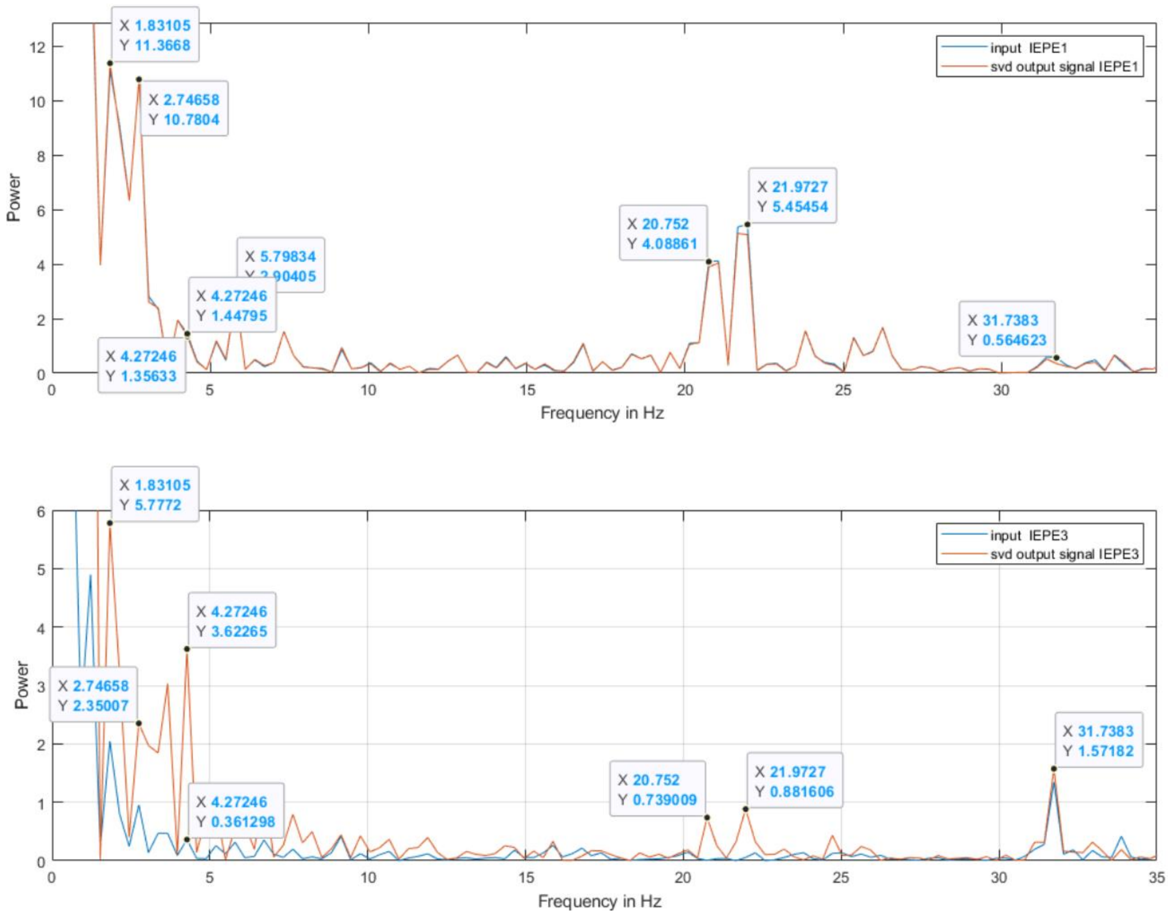

Figure 79: Close up Zoom of Test 3 FFT signal compare of SVD in- and output

The values of the data tip, corresponding to the calculated BPF of the inner and outer ring are located at $f_1 = 1.831\ Hz$ and $f_2 = 2.745\ Hz$, consecutivly numbered from left to right. Here the input impulse power of the IEPE1 is about five times and ten times higher than the input signal power of the IEPE3 sensor. This makes much sense, as the source of vibration is in the bearing housing. Taking the SVD output values into account, zero deviation within the housing signals and curiously a double up of the IEPE3 signal is visible. The latter does not follow the logic of a power shift via separation at these data points. The data point of $f_3 = 4.272\ Hz$ shows the strongest increase within the IEPE3 domain, produced through the SVD. This datapoint does refer to a datapoint in the IEPE1 signal, which is not displayed due to visibility of the line structure. This points have the assumed source of the vibration within the drive system and reduces its power with 10% in IEPE1 while the SVD's IEPE3 output is amplified with 1005%. The data tip of $f_4 = 20.752\,Hz$ and $f_5 = 21.9727\,Hz$ align with the forgone statement and decrease little with 6% in the IEPE1 output and increase with 660% for the IEPE3 output. The frequency of at $f_6 = 31.783\ Hz$ reduces with 35% for the IEPE1 signal and rises with 17% for the IEPE3 in-/output ratio. Note that alle inspected two second data sets within the full TD signal pointed towards the similar qualitative increase within the IEPE3 signal, above $f_3 = 4.272\,Hz$, and a slight signal reduction for the bearing housing. For the frequency bandwidth of $< f_3$ the reduction in the bearing housing is neglectable, while the IEPE3 shows strong amplifications within this area and can be defined as sourced within the drive system. So in total the performance of the higher frequencies is low, but partly supporting the thesis scope of a signal separation process. For the low frequencies of the expected vibrations, sourced in the bearing kinematics a reduction of the IEPE1 signal is not performed, fulfilling this scope criteria as well. But the IEPE3 sensor output takes the illusion of a fully successful approach, due to its amplification. Considering the findings of subsection 2.5.1, the solid born sound speed of the mainly measured bending waves [5] within these frequency ranges deviate strongly. This adds a dynamic runtime influence on the separation process for a multi body steel vibrational transmission environment. Also aliasing effects and low linearity accuracy could emerge close to the drive and cut-off frequency of 0.5 Hz of the drive itself and its sensor system and reduce the processivity by low resolution input data.

8 Results and Critical Discussion

The conceptional idea of machine learning based source separation for vibrational signals showed the demand of an extensive investigation of the fundamental wave propagation and thereby the main intricacies within the selected test rig system. By cooperating with Bachmann electronic, an appropriated measurement chain with multiple sensor sensitivities was selected and integrated into the DAQ system successfully. The test rig and its characteristics showed a solid base for the system behavior in terms of frequency response measurement, sensor application options and damage method reproduction ability to clearly identify the expected sources of vibrations. These results are evidenced via CM- based test methods and supports the thesis of a wear mark related vibrational investigation abilities with comparable WT roller speeds and general kinematic references through a specifically developed test sequence. First of these designs defined the impulse response of the main components and gave a solid base to debate the later FFT results. To raise a reference characteristic of a single source vibrational signal, the second evaluation pointed at the frequency characteristic of the drive system, showing the sensitivity differences within the utilized sensor types. The sensor compare by sensitivity was achieved successfully and contests a suitability for the LF sensor type BAM500 of *Bachmann electronics*. The main test design number three got evaluated with a BEA reference method and detected the ball pass frequencies of an initial RCF damage of inner and outer ring efficiently while enabling the validation with the analytical calculations. These results empower further investigations within the outlook if this thesis. The last performed test design investigated the lower threshold of wear detection methods by stepped cycle approaches and drive parameter adaption, showing a blurred BEA result for critically low overrolling speeds. The selection of a suitable machine learning algorithm was performed via case determination of the given sensor set. Implementing the SVD function on the vibrational data created inconclusive results in terms of the separation behavior. These deviation from the expected results are presumably due to the very short distances of the source sensor configuration which create a minimal runtime difference of 4 ms to transmit the waves from source to source, as well as the frequency dependent wave propagation speed within this isotropic multi-component structure and the very limited signal processing capability of two seconds. Also the matrices square proportion of the input value creates a critically high calculation effort for longer time span observations, which are mandatory for very low vibrational characteristic detection. Additional to this, the output designation of the SVD function conducted dynamic behavior within the signal allocation and an arbitrary algebraic signing. Reflecting these patterns of conduction, a general eligibility for un-/ and supervised machine learning processes cannot be verified. Considering the low performance of the SVD function several impediments within the pre-selection process are revealed. First, the general ability of the air environment-based separation algorithm test got postponed for the wave speed property of a multi-body isotropic environment. Second, the low data content of the two second data input led to a lack of delimitation for the generated peaks withing the BPF related frequency response graphs. Third, the computation power of the embedded signal converter was overestimated, limiting the upper high frequency limit to 5 kHz, cutting off inspection options for the SVD behavior in higher frequency ranges.

9 Outlook

Now looking back on the thesis related evaluation ideas and derived processes, the findings of the first and latter critic points could have testified the general approach for the algorithm within a constant bending wave speed range earlier. Therefore a stronger embedded PC could be integrated to the BEAT0.1 test rig. Additional to this option, the full transfer of the measurement chain from the test rig's 0.1 to the 0.2- series could be a solution, as it's controller unit provides a higher RAM and processor power. Same is for the second point for the LF area of the SVD output generator. Here a stronger computer center could be fed with at least seven seconds of data to clearly define and process the drive characteristics of the LS shaft and perform a separation approach. Due to the very low drive speed of test number four, the lower edge frequency of the LF sensor fell short significantly, and could not show characteristics of the drive, further the impulse energy was very low. So the referenced overrolling speed of a repeated test number four should, assumingly, be at least 20°/s or even higher to match realistic roller speeds and create reliable results. Rethinking the speed parameter in test three, several overrolling cycles with stepped speed reduction from 100 to 20°/s could help defining a threshold for a significant damage detection process. In general the result of this test showed a very promising outcome, which empowers the idea of a general BEA processing success without the need of a source separation. This test, with inherited roller speed and load properties, could be repeated in a more complex test rig like BEAT1.1 or 6.1 series. Basically the overrolling process with constant speeds is part of a WT control strategy (at e.g. idle to cut-in pitch adjustment) and enables the calculation of constant force condition within the loaded contact zone of the bearing. So cyclic BEA results could be fed into an AI- algorithm to track down harmful pitch periods through trend-based data clustering. Also the longer travel of the vibrational waves within these test rigs, or even wind turbine structures could benefit the approach of source separation via SVD or other algorithms. Therefore a reinvestigation of the used algorithm could be beneficial. Still the calculation power to process the data of the low overrolling frequencies shall be considered and might be enhanced by static pre-filtering or code adaption.

References

[1] F. Zhao, "Wind Energy Report 2022," GWEC, Brussels, 2022.

[2] M. Ogge, "https://www.welthungerhilfe.de," Diagram of Münchner RE, 06 2018. [Online]. Available: https://www.welthungerhilfe.de/informieren/themen/klimawandel/naturkatastrophen/. [Accessed 22 11 2022].

[3] E. Hau, Windkraftanlagen, 5. Auflage, Krailingen: Springer Vieweg, 2014.

[4] S. Faulstich, "Wind turbine downtime and its importance for offshore deployment," Fraunhofer IEE, Kassel, 2011.

[5] R. Wirth, "Maschinendiagnose an Industriegetrieben Teil I & II," *Antriebstechnik,* pp. S. 77-81, 1998, Ausgabe Nr. 10.

[6] N. Waters, "A word about sensor selectioon for condition monitoring systems," *Windpower "Engineering&Developement",* p. 1, 21 11 2016.

[7] WHO, "Chernobyl: The True Scale of the Accident," WHO, 2018.

[8] "Jumbos and the Square Cube Law," *Wind Power Monthly,* p. 1995, 01 04 1995.

[9] P. Dalhoff, *Berechnung und Konstruktion von Wind- und Wellenenergieanlagen, Vorlesung 5: Lastannahmen,* Hamburg: HAW Hamburg, 2020.

[10] vattenfall-and-ge-join-forces-to-deploy-haliade-x-12mw-wind-turbine, "www.energyglobalnews.com," energy global news, 20 05 2019. [Online]. Available: http://www.energyglobalnews.com/vattenfall-and-ge-join-forces-to-deploy-haliade-x-12mw-wind-turbine/. [Accessed 18 05 2022].

[11] M. Stammler, Endurance Test Strategies for Pitch Bearings, Hannover: Fraunhofer Verlag, 2020.

[12] Solargenossenschaft Liechtenstein, "www.solargenossenschaft.li," 20 11 2020. [Online]. Available: https://www.solargenossenschaft.li/rueckschlag-fuer-vertikales-windkraftwerk-vertical-sky/. [Accessed 23 05 2022].

[13] R. Gasch, Windkraftanlagen, Berlin: Teubner, 2005.

[14] C. Bayles, "Extending wind turbine life with pitch bearing upgrades," 03 02 2020. [Online]. Available: https://www.windpowerengineering.com/extending-wind-turbine-life-with-pitch-bearing-upgrades/. [Accessed 30 ß5 2022].

[15] Union of Concerned Scientists, "How Wind Energy Works," 21 October 2013. [Online]. Available: https://www.ucsusa.org/resources/how-wind-energy-works. [Accessed 24 05 2022].

[16] Silmley, Fürst, Haizmann, "Optimizing Lidars for Wind Turbine Control- Results from the IEA Wind Task 32 Workshop," Remote Sensing, MDPI, Stuttgart, 2018.

[17] Scholbrock, Flemin, Schlipf, "Lidar-enhanced wind turbine control: Past, present, and future," IEEE, Boston, 2016.

[18] NSK Europe Ltd., "https://www.nskeurope.de," 2022. [Online]. Available: https://www.nskeurope.de/de/bearings/industries/wind-energy.html. [Accessed 08 06 2022].

[19] P. Jamieson, Wind Turbine Design, West Sussex: Wiley, 2011.

[20] E. A. Bossanyi, "Further Load Reductions with Individual Pitch Control," *Wind Energy, vol. 8,* pp. 481-485, 2005.

[21] F. Kovacevic, "Own Rendered Figure Siemens NX12," Fraunhofer IWES, Hamburg, 2022.

[22] " IMO GmbH & Co. KG, Produktkatalog Drehverbindungen," IMO, Gremsdorf, 2013.

[23] M. Stammler, "Internal Document of Finalized IWES Project," IWES, Hamburg, 2022.

[24] " Rothe Erde, Großwaelzlager: Gesamtlieferprogramm," Rothe Erde, 2016.

[25] A. Bartschat, "Internal IWES Report of IBAC Test Results," Fraunhofer Internal, Hamburg, 2022.

[26] O. Günes, *Assessment of Pitch Movements Based on Wear Damage Evaluation,* Hamburg: Fraunhofer Verlag, 2021.

[27] Schwack, Stammler, Halmos, "Wear in wind turbine pitch bearings—A comparative design study," Research Gate, Hamburg, 2022.

[28] K. Behnke, "Internal HBDV Project Report," Fraunhofer IWES, Hamburg, 2022.

[29] F. Schleich, "Internal Project Sketch for Ring Fatique," Fraunhofer IWES, Hamburg, 2022.

[30] C. Mittleider, "https://www.malloywind.com," malloywind, 21 9 2021. [Online]. Available: https://www.malloywind.com/articles/blade-bearing-ring-cracks-pt1. [Accessed 25 11 2022].

[31] S. Hambric, "https://www.researchgate.net," 02 01 2006. [Online]. Available: https://www.researchgate.net/publication/243716526. [Accessed 01 02 2023].

[32] "https://www.onlinemathlearning.com," 03 02 2020. [Online]. Available: https://www.onlinemathlearning.com/transverse-longitudinal-wave.html. [Accessed 01 03 2023].

[33] Dresig et al., Schwingungen, Brelin: Springer Vieweg, 2020.

[34] Brommundt et al., Schwingungslehre, Berlin: Springer Vieweg, 2018.

[35] Nashif et al., Vibration Damping, J. Wiley and Sons, 1986.

[36] M. Beranek, Noise and Vibration Control, McGraw Hill, 1988.

[37] H. Fritsch, "Condition Monitoring als Technologie zur Optimierung der Lebenszykluskosten“," VTT- Vorarlberger Technik Tag 2013, Dornbirn, 2013.

[38] M. Schedat, "Entwicklung eines Structural health Monitoring- Konzepts zur Beurteilung von Windenergieanlagen," HS Flensburg, Flensburg, 2017.

[39] VDI, "https://www.vdi.de," VDI, 04 2013. [Online]. Available: https://www.vdi.de/richtlinien/details/vdi-3832-koerperschallmessungen-zur-zustandsbeurteilung-von-waelzlagern-in-maschinen-und-anlagen. [Accessed 2023 03 08].

[40] T. Esswanger, Elements of statistical analysis, Wien: Springer, 1986.

[41] F. Harris, "http://web.mit," 01 01 1978. [Online]. Available: http://web.mit.edu/xiphmont/Public/windows.pdf. [Accessed 12 04 2023].

[42] PCB Piezotronics , "Schwingungsmessung an rotierenden Maschinen," 01 02 2018. [Online]. Available: https://www.synotech.de/produkte_skript/downloads/marketing/SYN_Schwingungsmessung_an_rotierenden_Maschinen_Applikationsbroschuere_DEU.pdf. [Accessed 21 03 2023].

[43] IDOM©, *(Internal document) Final Design Concept BEAT6.1,* Bilbao, 2018.

[44] M. Stammler, "https://www.iwes.fraunhofer.de," Fraunhofer IWES, 01 02 2020. [Online]. Available: https://www.iwes.fraunhofer.de/de/testzentren-und-messungen/antriebsstrang-komponenten.html#1286397915. [Accessed 30 11 2022].

[45] M. Stammler, "Internal Document: Zyklenmusterversuch von oszillierenden Wälzlagern," Fraunhofer IWES, Hamburg, 2017.

[46] SPINEA, s.r.o, *Product Catalogue of SPINEA Drivespin series,* Presov, Slovakia, 2019.

[47] M. Stammler, "A Brief Definition of Rolling Contact Kinematics," Internal Document, Hamburg, 2022.

[48] Dimitrov, Kelly, Berg, "From wind to loads: wind turbine site-specific load estimation using data bases with high fidelity load simulations," *eawe,* 03 2018.

[49] "Entwicklung eines Structural Health Monitoring- Kozepts zur Beurteilung von Windenergieanlagen im Hinblick auf Schadensfrüherkennung und den Weiterbetrieb nach Ablauf der geplanten Nutzungsdauer," Wind Energy Technology Institute, Flensburg, 2017.

[50] N. Cosack, P.h.D: Fatigue Load Monitoring with Standard Wind Turbine Signals, Stuttgart: University of Stuttgart, 2010.

[51] NREL, "Use of SCADA Data for Failure Detection in Wind Turbines," NREL, Washington, 2011.

[52] Bachmann electronic GmbH, "https://www.bachmann.info/," 08 2021. [Online]. Available: https://www.bachmann.info/media/2106/download/CM_Sensor_BAM500_en.pdf?v=2&inline=1. [Accessed 10 01 2023].

[53] H. Slatky, *Dissertation: Algorithmen zur richtungsselektiven Verarbeitung von Schallsignalen: die Realisierung eines binauralen Cocktail-Party-Prozessor-Systems,* Bochum: Ruhr Universität Bochum, 1992.

[54] T. Duong, "Audio Source Separation exploiting NMF-based Generic Source Spectral Model," ResearchGate, Hanoi, 2019.

[55] L. Makino, Blind Speech Separation, Berlin: Springer, 2007.

[56] N. Wand, Blind Source Separation: Advances in Theory, Algorithms and Applications, Berlin: Springer, 2014.

[57] N. Sunohara, "DNN-based Environmental Sound Recognition with Real-recorded and," Semantic Scholar, Taipeh, 2016.

[58] K. Lawrence, Fundamentals of acoustic, New York: Library Genesis, 2000.

[59] Andrew Ng lecture at learning platform, "Introduction Lecture of Machine Learning," Coursera, Stanforf, 2014.

[60] MathWorks , "Cocktail Party Source Separation Using Deep Learning Networks,"

MathWorks, 2020.

[61] Stoller, Ewert, Dixon, "WAVE-U-NET: A MULTI-SCALE NEURAL NETWORK FOR," 08 06 2018. [Online]. Available: https://arxiv.org/pdf/1806.03185v1.pdf. [Accessed 27 03 2023].

[62] M. Takahashi, "https://arxiv.org," 29 06 2017. [Online]. Available: https://arxiv.org/pdf/1706.09588v1.pdf. [Accessed 27 03 2023].

[63] L. Hu, "A subspace approach for enhancing speech corrupted by colored noise," IEEE International Conference on Acoustics, Orlando, 2003.

[64] "Effect of singular value decomposition based on processing on speech perception," *International Journal on Natural Language Computing,* p. 9, 02 2013.

[65] S. Greg, "https://stackoverflow.com/," 06 12 2013. [Online]. Available: https://stackoverflow.com/questions/20414667/cocktail-party-algorithm-svd-implementation-in-one-line-of-code. [Accessed 29 03 2023].

[66] De lathauwer, De Moor, "A Multilinear Singular Value Decomposition," *SIAM Journal on Matrix Analysis and Applications.,* p. 21, 01 01 2000.

[67] F. Kovacevic, "Protocol of Bachmann Electronics Expert Talk," Hamburg, 2022.

[68] F. P. Leon, Messtechnik, Berlin: Springer Vieweg, 2015.

[69] T. Kuttner, Praxiswissen Schwingungsmesstechnik, Berlin: Springer Vieweg, 2015.

[70] Jonscher et al., "Very low frequency IEPE accelerometer calibration and application to a wind energy structure," *eawe,* p. 7, 02 05 2022.

[71] Gantner Instruments, " www.gantner-instruments.com," 02 2021. [Online]. Available: https://gi-productbase.gantner-instruments.com/en/products/30/datasheet/web/latest/a4/. [Accessed 03 2023].

[72] Beckhoff Automation, "https://www.beckhoff.com," [Online]. Available: https://www.beckhoff.com/de-de/produkte/i-o/ethercat-klemmen/elmxxxx-messtechnik/elm3604-0000.html. [Accessed 23 03 2023].

[73] Gantner Instruments, "https://www.gantner-instruments.com/," Gantner Instruments, [Online]. Available: Gantner Instruments, „https://www.gantner-instruments.com/,“ [Online]. Available: https://www.gantner-instruments.com/zh-hans/blog/voltage-iepe-sensor-measurement-data-acquisition-daq-with-q-bloxx-a111/. [Accessed 23 03 2023].

[74] Unknown, "https://www.directindustry.fr/," Beckhoff Automation, [Online]. Available: https://www.directindustry.fr/prod/beckhoff-automation/product-7183-442003.html.

[Accessed 23 03 2023].

[75] Unknown, "https://logos-download.com/5684-mysql-logo-download.html," [Online]. Available: https://logos-download.com/5684-mysql-logo-download.html. [Accessed 23 03 2023].

[76] Shannon, Claude, Elwood, "Communication in the Presence of Noise," *IEEE Vol.86,* pp. 447-457, 2 1998.

[77] O. Menck, "Commissioning of the vibrational sensor system (Internal IWES Document)," Hamburg, 2022.

[78] MathWorks, "Kaiser Window Documentation," 2023.

[79] M. Stammler, "Internal Document (Pitch Profile Developement Tool)," Fraunhofer IWES, Hamburg, 2023.

[80] Baeldung, "https://www.baeldung.com," Baeldung, [Online]. Available: https://www.baeldung.com/cs/normalizing-inputs-artificial-neural-network. [Accessed 23 04 2023].

[81] G. Scheffels, "keNEXT," 19 07 2016. [Online]. Available: https://www.ke-next.de/antriebstechnik/mechanische-antriebstechnik/verbesserte-waelzlager-fuer-windenergieanlagen-109.html. [Accessed 08 06 2022].

[82] Gantner Instruments, "www. Gantner-instruments.com," 02 2021. [Online]. [Accessed 23 03 2023].

[83] Vestas Wind Systems, "Vestas.com," 01 03 2021. [Online]. Available: https://nozebra.ipapercms.dk/Vestas/Communication/Productbrochure/OffshoreProductBrochure/v236-150-mw-brochure/?page=8. [Accessed 01 04 22].

Ich versichere, dass ich die vorliegende Arbeit ohne fremde Hilfe selbständig verfasst und nur die angegebenen Quellen und Hilfsmittel benutzt habe. Wörtlich oder dem Sinn nach aus anderen Werken entnommene Stellen sind unter Angabe der Quelle kenntlich gemacht.
In manchen Fällen ist ein spezieller Wortlaut durch Richtlinien der Hochschule oder des Unternehmens vorgegeben.

Ich erkläre mich damit

o einverstanden,

o nicht einverstanden

dass ein Exemplar meiner Master- Thesis in die Bibliothek des Fachbereichs aufgenommen wird; Rechte Dritter werden dadurch nicht verletzt.

Hamburg, den ..... [redacted] ....